Optical Micromanipulation Using Ultrashort Pulsed Laser Sources

by

Helen Little

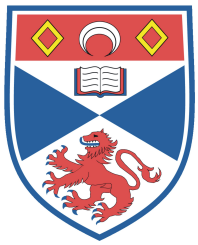

Thesis for the degree of
Doctor of Philosophy
May 2007

The J.F. Allen Physics Research Laboratories
School of Physics & Astronomy
University of St Andrews
St Andrews, Fife
Scotland

"Roads?...Where we're going, we don't need roads..."

Contents

List of Figures

Declarations

I, Helen Little, hereby certify that this thesis, which is approximately 40,000 words in length, has been written by me, that is the record of work carried out by me, and that it has not been submitted in any previous application for a higher degree.

date signature of candidate

I was admitted as a research student in September 2002 and as a candidate for the degree of Ph.D. in September 2003; the higher study for which this is a record was carried out in the University of St.Andrews between 2002 and 2006.

date signature of candidate

I hereby certify that the candidate has fulfilled the conditions of the Resolution and Regulations appropriate for the degree of Ph.D. in the University of St. Andrews and that the candidate is qualified to submit this thesis in application for that degree.

date signature of supervisor

In submitting this thesis to the University of St. Andrews I understand that I am giving permission for it to be made available for use in accordance with the regulations of the University Library for the time being in force, subject to any copyright vested in the work not being affected thereby. I also understand that the title and abstract will be published, and that a copy of the work may be made and supplied to any *bona fide* library or research worker.

date signature of candidate

Acknowledgements

Through the course of my research many people have helped me in many different ways and all are deserving of sincere thanks. First and foremost, I would like to thanks my supervisors Professors Kishan Dholakia and Wilson Sibbett. They have guided, encouraged and inspired me every step of the way.

For their time and assistance, I must also thank Tom Brown, Pascal Fischer, Chris Leburn, Iain Cormack, Vene Garcés-Chávez, Barry Stormont, Ben Agate, Tanya Lake, Hannah Melville, Steven Neale and Toni Carruthers.

I must also acknowledge my Gannochy partners in crime: Debs, Charlie, Alex & Sara. Three down, one to go...

Most of all, I must thank my family who have supported me through this venture. Thanks and love to Mum, Dad, Bert, Elayne, Katie, Jamie, Molly & Eleanor.

Abstract

In this thesis two previously separate fields of study are brought together: optical micromanipulation and ultrashort laser research. Here, the benefits of combining the high peak powers of ultrashort pulsed lasers and conventional optical micromanipulation techniques are explored. As optical trapping has been studied extensively, the focus of this research is on optical guiding. Moreover, the emphasis is on the use of Bessel beams as these have been shown to offer greater guiding distances than comparable Gaussian beams. The studies within this thesis show that optical guiding in Bessel and Gaussian beams is governed by the average power of the laser. However, the benefits of guiding with ultrashort pulsed lasers to exploit multi-photon processes become evident as the demonstration of simultaneous optical guiding and second harmonic generation in microscopic nonlinear crystal fragments is detailed. This work is developed by using ultrashort pulses to induce two-photon excitation-induced fluorescence in the guiding medium. This allows direct visualisation of the beam-particle interaction and measurement of the reconstruction of the Bessel beam around an object. Some studies using two-photon excitation to investigate Bessel beam penetration through turbid media are discussed. Finally, the work is concluded by exploring the use of pulsed white-light lasers in optical guiding. The wavelength-dependent propagation and reconstruction properties of the white-light Bessel beam are studied before some preliminary optical guiding experiments are discussed. From this, the broad bandwidth of the supercontinuum source is found to offer extended guiding distances in Gaussian beams thereby negating the need for Bessel beams.

Synopsis

The aim of this thesis is to explore optical guiding and multi-photon excitation using ultrashort-pulse and broadband white-light sources. In this study, I move away from the usual Gaussian light fields and explore the use of non-diffracting light beams. The research forms part of a wider vision to find applications in the fields of biophysics and medicine. For this reason, the work has been constrained to the manipulation of microscopic objects on the same scale as many biological structures of which are of interest in these fields.

To set the scene, Chapter 1 introduces the fields of optical micromanipulation and ultrashort pulses. There are several optical micromanipulation techniques such as tweezing, sorting and guiding. These techniques rely on the radiation pressure of light to constrain or manipulate an optically transparent object. For the purpose of this thesis, however, the focus will be on the optical guiding using some novel beam types as there has been little research in this area. For multi-photon excitation and the generation of broadband white light the high peak power of ultrashort pulses are required. For this reason, the physics of ultrashort pulses will also be introduced here. In the following chapters these topics will be discussed in more detail.

We begin this in Chapter 2 by discussing the generation of ultrashort pulses. This relies on the use of modelocking techniques. While there are many techniques available, the focus in this thesis will be on those employed in the lasers used for the experiments I carried out. In a brief overview, a flavour of the some of the existing applications which use ultrashort pulses is given in this chapter.

Particular attention is given to those applications in the fields of biology and medicine. These include microscopies which rely on the multi-photon excitation techniques of which this thesis is concerned. Consequently, the chapter concludes with a discussion on two-photon excitation-induced fluorescence and second-harmonic generation. From here the attention moves to the physics of optical micromanipulation. In Chapter 3 we consider first the forces acting on a particle within a light beam. This forms the basis of the subsequent discussions on optical micromanipulation under two distinct sets of conditions known as the Mie and Rayleigh regimes. Two important factors in optical guiding studies include those of convection and diffusion and these will be discussed briefly here. From this chapter the natural progression is to one which discusses the types of beams that can be used in this technique.

Since the first demonstration of optical guiding, there has been much interest in using non-Gaussian beams. In Chapter 4 we introduce a special beam called the Bessel beam which is known for its non-diffracting properties. To aid appreciation of the unique properties of the Bessel beam the Gaussian beam is discussed briefly first. The spotlight then falls on some techniques which are used for generating Bessel beams. As well as being non-diffracting one of the key properties of the Bessel beam is its self-healing property. This is discussed in detail as it forms a significant part of the experimental work in this thesis.

Before moving on to discuss this experimental work there is an opportunity to review some of the previous work carried out by others in this field. Optical micromanipulation is a vast subject of study. To review it fully is not possible here and so Chapter 5 is limited to a brief overview of three pivotal experiments which are pertinent to my research. This includes the early ground-breaking

experiments by those at the forefront of optical manipulation research.

Having given the reader an introduction to the fields of optical guiding, ultrashort pulse research and novel beams we can begin to detail the experimental work carried out. Bringing together these three topics, Chapter 6 relates first details experiments which were designed to compare and guiding with continuous wave and ultrashort-pulsed lasers in Bessel and Gaussian beams. Next we begin our exploration into multi-photon excitation experiments with a detailed description of simultaneous second-harmonic generation and optical guiding of particles.

This exploration is taken further with the experiments detailed in Chapter 7. Here, some very interesting and exciting work is carried out into using two-photon excitation-induced fluorescence as method of actually visualising the self-healing properties of a Bessel beam. From this we can compare experiment with theory. A second experiment is detailed which again uses the two-photon excitation-induced fluorescence as measurement tool. The aim was to determine whether the self-healing properties of Bessel beams can give increased penetration through turbid media as a precursor for developing better tissue probes.

As this research period came to an end, I was given the opportunity to carry out some experiments using a broadband white-light source. This was a natural extension to the previous work as the white-light source known as a supercontinuum, has properties similar to ultrashort pulsed lasers used previously. The supercontinuum also has a pulsed output but has a much broader spectral

output. Therefore in Chapter 8 the attention turns to the generation and characterisation of a white-light Bessel beam. The focus here is on the exploring its propagation and self-healing properties.

Finally, exploratory experiments into optical guiding with white-light Bessel beams are detailed. Due to time constraints, I was unable to complete this work however this formed the basis for further work which was carried out by colleagues after my departure.

Publications

1. P Fischer, H Little, R L Smith, C Lopez-Mariscal, C T A Brown, W Sibbett and K Dholakia, "Wavelength dependent propagation and reconstruction of white light Bessel beams", J. Opt. A.: Pure Appl. Opt. **8** (2006) 1 - 6.

2. K Dholakia, H Little, C T A Brown, B Agate, D McGloin, L Paterson and W Sibbett, "Imaging in optical micromanipulation using two-photon excitation", New J. Phys. **6** 136 (2004)

3. H. Little, C.T.A. Brown, V. Garcés-Chávez, W. Sibbett and K. Dholakia, "Optical guiding of microscopic particles in femtosecond and continuous wave Bessel light beams", Opt. Express **12**, 2560 (2004)

4. H. Little, C. T. A. Brown, V. Garcés-Chávez, W. Sibbett, K. Dholakia, "Optical guiding with continuous wave and femtosecond lasers", Proceedings of SPIE **5514** (SPIE, Bellingham, WA, 2004) 524-529 (2004).

"The desire to explore our surrounding world has always been one of the strongest characteristics of human nature. Columbus and the great explorers travelled outwards and discovered new continents in the 16^{th} century and Bohr, Einstein, Rutherford, Curie and many others travelled inward to explore the secrets of the atomic world in the 20^{th} century."

"Explorers used ships, planes or spacecraft to travel outward and they use increasingly sophisticated tools to travel inward into the world of atoms and molecules. Here, at the beginning of the 3^{rd} millennium we have microscopes allowing us to see single atoms and telescopes allowing us to see the edges of the universe. At the end of the 10^{th} century a fascinating new tool, the femtosecond laser was developed. The femtosecond laser provides us with ultra short light pulses, allowing the motion of atoms and molecules to be captured as if they were filmed. To have, not only the structure of the atoms and molecules, but also their motion, is of unique importance in our quests to understand and control chemical and biological processes".[1]

"The precise degree of control made possible by optical trapping and manipulation of small neutral particles has caught the imagination of experimentalists in diverse areas of science, especially atomic physics and biology. Many ingenious and previously impossible experiments have been devised, some having revolutionary impact. The field is still young, and the scope of applications is still growing. Advances in laser technology should further stim-

ulate adoption of these novel manipulation methods. The future looks bright" - Arthur Ashkin, March 11, 1997

CHAPTER 1

Introduction

From the first demonstration of light amplification by stimulated emission radiation, laser research and development has become widely used in daily life but more importantly it has become an indispensable tool in physics-based research. More recently it has become of interest to those working in the fields of biophysics and medicine. With its quasi-monochromatic, high-power and highly-directional output as well as temporal and spectral coherence the laser has achieved supremacy as a spectral source. These properties have allowed the laser to be developed into a tool for tissue ablation, corneal and retinal surgery and in the treatment of some cancers.

Concurrently there has been considerable focus on laser development in telecommunications where ultrashort pulses have been shown to improve data transfer rates and capacity. This has led to the development of a range of laser sources in terms of wavelength, power, repetition rates, cost and size. From Maiman's first ruby laser built in 1960, there are now many more lasers sources available [2]. These have now been finding applications in the fields of biophysics and medicine. In recent years there has been some interest in using ultrashort-pulsed

lasers in multi-photon microscopies and optical micromanipulation techniques.

As a contribution to this research, the aim of this thesis is to explore the optical guiding and multi-photon excitation using ultrashort-pulsed lasers as well as a relatively new broadband white-light source known as the supercontinuum. Most of the preceding work in optical micromanipulation has been focussed on optical tweezing techniques and using Gaussian beams [3, 4]. For this reason, we move towards optical guiding using non-diffracting Bessel beams. These have been shown to offer longer guiding distances over conventional beams. As both fields play a fundamental part of this research here we give an introduction to ultrashort-pulsed lasers and optical manipulation techniques [5, 6].

From the biggest, most powerful and expensive research tools to the tiny, cheap devices found in compact disc players, the basic and essential elements of a laser include a gain medium, pump source and a system of mirrors forming a resonator cavity as illustrated in figure 1.1. Every laser requires an input of

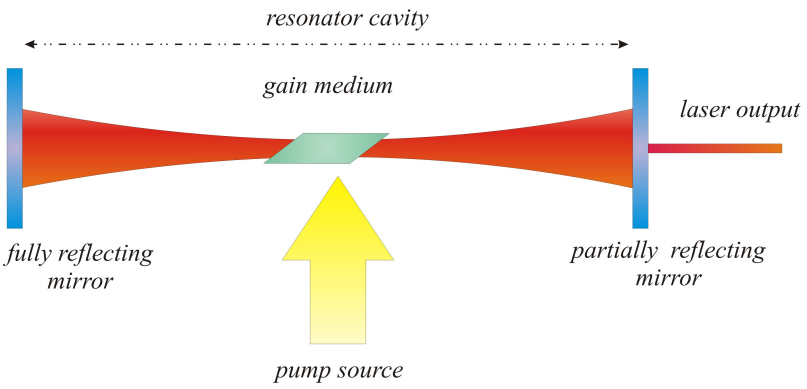

Figure 1.1: The three basic and fundamental elements of a laser: pump source, resonator cavity and gain medium. The output is coupled via the partially reflecting mirror

energy to launch the lasing process and this is provided by the pump source.

This can be in the form of an electrical discharge, a flash or arc lamp, a chemical reaction or more usually another laser. For example a helium-neon (He-Ne) laser uses an electrical discharge in a gas mixture. The Nd:YAG laser is pumped by focused light from a xenon flash lamp and the Ti:sapphire laser can be pumped by a high power argon-ion or a number of diode lasers.

The pump source exists to continually excite atoms from a ground state into a higher state. These excited atoms can relax by one of several radiative and non-radiative processes. The non-radiative processes include loss of energy to heat and the creation of phonons. More important are the radiative processes of spontaneous and stimulated emission of photons. In spontaneous emission the atom relaxes and emits a photon which has a random phase, polarisation and direction. By contrast, stimulated emission can occur when an incident photon stimulates the atom to relax. The emitted photon possesses the same phase, polarisation and direction of the incident photon. Akin to a chain reaction, the emitted photons can cause further stimulated emission processes. It is this stimulated emission that is desired for the lasing process. However, the probability of an atom undergoing stimulated emission is dwarfed by that of spontaneous emission. By introducing a resonator cavity, the stimulated emission can be enhanced by repeatedly reflecting the photons through the medium. The random direction of the photons which result from spontaneous emission means most are lost from the system while most of the photons from stimulated emission are confined within the cavity. The pump source maintains this process of excitation and stimulated emission.

Once the pumping process produces a gain of stimulated emission which exceeds the cavity losses, then a tiny proportion of the light can escape via a

partially-reflecting mirror at one end of the cavity producing the laser beam. This point at which the gain equals the cavity losses is called the *lasing threshold*.

The optical resonator cavity in its simplest form is two highly reflecting interfaces placed around the gain medium which provide feedback of the light. In more complex lasers, configurations with four or more mirrors forming the cavity are used. The design and alignment of the mirrors with respect to the medium is crucial to determining the exact operating wavelength and other attributes of the laser system. The mirrors are given optical coatings which determine their reflective properties.

For efficient excitation and therefore a more efficient lasing process, in optical pumping at least, the wavelength of the pump source must be matched to the absorption profile of the gain medium. The gain material can be a gas, liquid, solid or a semiconductor material. The physical properties of the material dominates the spectral properties of the emitted laser light. Lasers can not only be categorised in terms of their physical properties but also in terms of their spectral output properties: narrow bandwidth versus broad bandwidth and continuous wave output versus pulsed output.

Quasi-monochromatic lasers such as the Helium-Neon laser have a very defined narrow gain bandwidth centered at $632.8nm$ whereas the Ti:sapphire laser has a broad gain bandwidth, depending on the pump source, intracavity components and configuration, of between $770nm$ to $820nm$. In the He-Ne laser, the Helium gas atoms which constitute nearly 90 per cent of the gas mixture, accumulate

in the 2^1S and 2^3S states. The Helium atoms collide inelastically to transfer some of their energy to the $5s$ and $4s$ states. Allowed transitions between these and the other energy states give laser transitions in the infrared ($1152.3nm$ and $3391.2nm$) and the visible red ($632.8nm$) and green ($543.5nm$). In the case of the Ti:sapphire and other vibronic gain materials, the energy levels are smeared. Excited atoms can by emission of phonons relax to lower energy sub-levels within that level. The laser transitions can therefore occur over a range of wavelengths with varying intensities.

Earlier we alluded to the importance of the laser cavity in determining the operating wavelength of the laser. Its importance lies in whether it can support the existence of these laser transitions within the laser. The resonator cavity imposes restrictions on the wavelengths of light that can propagate within it. In the case of a two mirror cavity, the electric field of the radiation takes on a standing wave pattern which means that there must be a node at each mirror. Therefore the cavity will resonate if and only if there is an integer number, m, of half wavelengths in the cavity of length L. That is,

$$m = \frac{L}{\lambda/2} \tag{1.1}$$

with $v = \nu\lambda$ where v is the velocity, ν is the frequency and λ is the wavelength of the radiation this gives

$$\nu_m = \frac{mv}{2L} \tag{1.2}$$

Thus there are an infinite number of possible standing waves or longitudinal cavity modes which are separated by

$$\Delta\nu = \frac{v}{2L} \tag{1.3}$$

From this relationship, it follows that as the cavity gets smaller, the spacing in frequency between supported longitudinal cavity modes gets larger. For lasing, only modes with frequencies that lie within the bandwidth of the gain medium will be supported and consequently it is possible to design cavities for single mode operation.

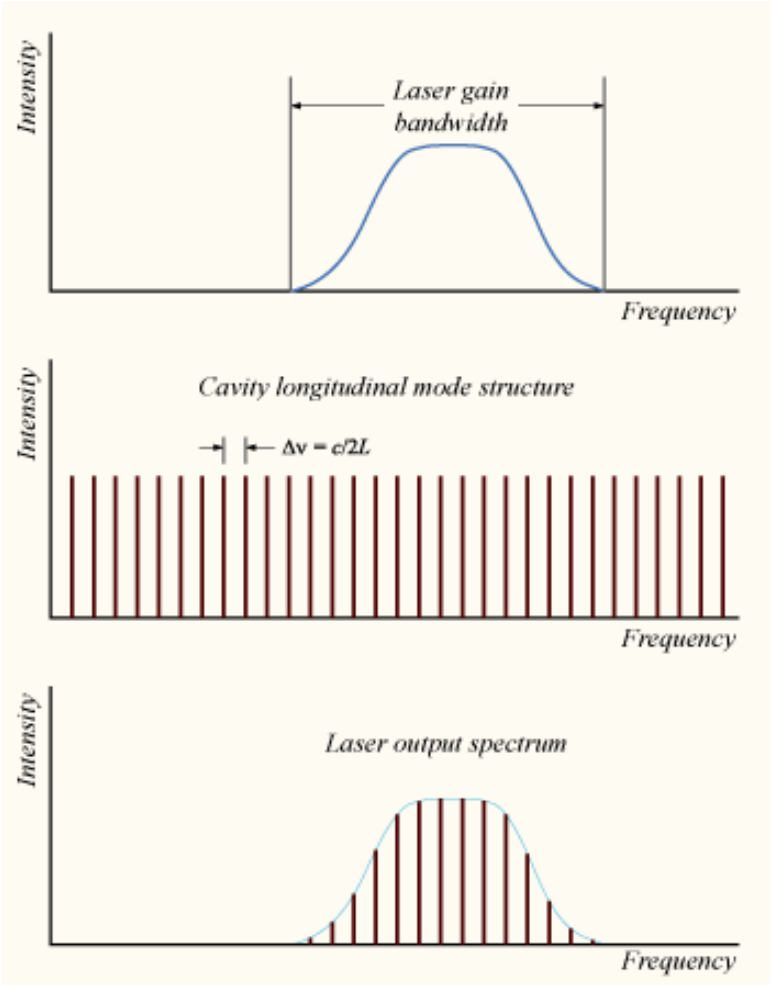

Figure 1.2: The gain bandwidth of a laser medium spans a certain wavelength range (top). The cavity supports longitudinal modes separated by frequency $\delta\nu = c/2L$ (middle). Combined the laser medium and cavity will support lasing of a restricted subset of modes (bottom)

For this reason, even gain materials with broad emission bandwidths have narrow largely monochromatic outputs. At least it is fair to say that *continuous*

wave (cw) laser outputs are monochromatic. With lasers which have a broad bandwidth gain material it is possible, by careful design of the cavity, to produce pulsed outputs of a short durations from milliseconds down to femtoseconds. To understand just how short these pulses are, consider how far light can travel during that time-frame. The shortest optical pulses demonstrated to date have a pulse duration of $4,2 \times 10^{-15}$ seconds during which time light can travel just $1.26\mu m$. With these shorter pulse durations, the power from a laser is squeezed into each pulse giving huge peak powers which can prove very useful in a plethora of applications. The first pulses produced were in the range of microseconds but with the advent of Q-switching techniques, nanosecond pulses became achievable. Shorter pulses came by employing mode-locking techniques where random noise fluctuations were forced either passively or actively to produce trains of short bursts of laser light. Active modelocking techniques are those which require an intracavity element such as a semiconductor saturable absorber to force the phase of the cavity modes to lock together [7, 8, 9]. A saturable absorber is any material which has decreasing light absorption when exposed to increasing light intensity. Semiconductors prove to be a good choice of material for this as they absorb over a broad range of wavelengths and their recovery time and saturation fluence can be controlled in the design and manufacture stage. Through the 1970s and 1980s, passive mode-locking techniques and saturable dye absorbers led to the production of picosecond and ultrashort pulses. However, it was the discovery of spontaneous mode-locking by Sibbett et al. in 1991 which produced pulses as short as 60 femtoseconds from a Kerr-lens modelocked Ti:sapphire laser [10]. This technique is particularly interesting as it requires no external intervention but instead relies only on the properties of the beam itself and its nonlinear interaction with the gain material. Kerr-lens modelocking occurs specifically in solid state lasers such as

the ubiquitous Ti:sapphire laser. It arises from the Kerr effect which, as will be discussed more fully in Chapter 2, modifies the refractive index n of a medium to

$$n = n_0 + n_2 I \tag{1.4}$$

where n_0 is the linear refractive index, n_2 is the nonlinear refractive index and I is the instantaneous intensity of the beam. At cw powers, the nonlinear refractive index is negligible. However when subjected to very high intensities the refractive index of the medium can be altered significantly. A spike of high intensity radiation can be introduced to the laser cavity by tapping the end mirror. As illustrated in figure 1.3, this spike or noisy pulse will have a high intensity which alters the refractive index of the crystal as it propagates through the crystal causing it to act as a lens. As the crystal focusses the beam the increasing intensity exacerbates the effect. The end result is a laser cavity with a soft aperture which encourages the laser cavity to support pulsed operation over continuous wave operation. The separation of the pulses, also known as repetition rate, is determined by the round trip time of the cavity and therefore by reducing the size of the cavity increases the repetition rate of the pulses. The properties of the laser light from a pulsed laser differ from that from

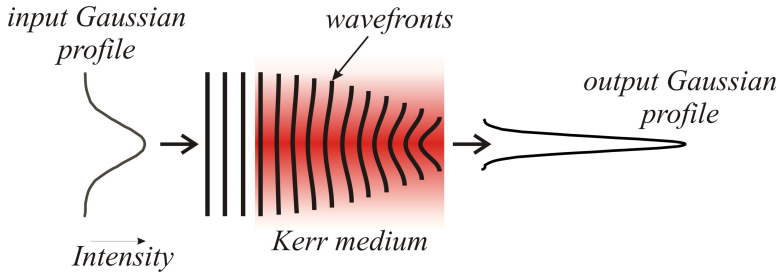

Figure 1.3: Self-focussing of a laser beam through a solid-state gain medium which exhibits the Kerr effect(Kerr medium). The high intensity profile of an noise spike acts to increase the refractive index by means of the Kerr effect. This, in turn, focusses the beam further. The cavity sees less loss with high intensity spikes and hence is encouraged into producing a pulsed output

a cw laser. Consider two cw and pulsed lasers with comparable average output powers at a defined wavelength. With the cw laser, the output is constant and effectively monochromatic. The first notable difference can be understood by considering the bandwidth theorem $\Delta\nu\Delta\tau \geq 2\pi$ where $\Delta\tau$ is the pulse duration. For a cw laser, $\Delta\tau$ tends to infinity and hence the bandwidth, $\Delta\nu$, tends to a line function or more realistically, a monochromatic beam. In contrast, the pulsed laser has a defined pulse duration and consequently has an defined bandwidth and hence the approximation to a line function is no longer valid. The second notable difference is the relatively massive peak power of the pulses compared to the average output. These two main properties of pulsed lasers have been exploited either together or alone in many applications. The high peak powers of pulses can induce nonlinear effects in materials such as multi-photon absorption, second- and third-harmonic generation and indeed the aforementioned Kerr effect. The increased bandwidth of the pulses have been used in data transfer techniques where the pulse broadening is encouraged as the greater bandwidth $\Delta\nu$ can give even shorter pulse durations. However, that aside, perhaps the exciting attribute is the amazingly short pulse duration as it has opened up a new field of 'femtoscience'. In 'femtoscience', femtosecond time resolution is required to study the atomic and molecular dynamics of reactions and processes (Fig 1.4). Now it is possible for biologists to study complex biochemical reactions such as photosynthesis which take place within a time frame of only a few femtoseconds. Similarly, chemists can now observe the dynamics of chemical bond making and breaking while physicists have recently used ultrashort X-ray pulses to probe atomic phenomena such as coherent lattice vibrations. Figure 1.4 shows the timescales of some biological, chemical and physical processes that can be probed using short and ultrashort laser pulses.

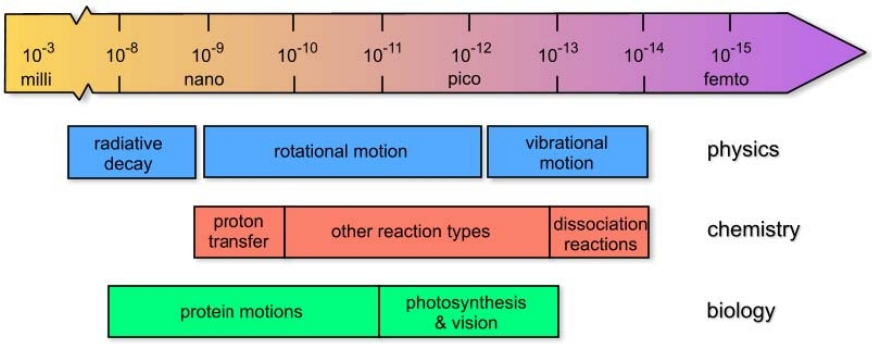

Figure 1.4: Many biological, chemical and physical processes occur on a femtosecond timescale and can be studied using femtosecond laser-based techniques.

Using ultrashort pulses of laser light as a dynamic probe has become a useful technique. However, the power of the ultrashort pulse is not limited to ultrafast speed photography of biological, chemical and physical processes. Its potential for use in new applications across the sciences is huge. When an established technique or tool is taken into other sciences or research, exciting experiments and results are possible. Just as femtoscience has been generated from the cross-fertilisation of the traditional branches of sciences, other exciting areas of research today are also emerging.

For many years now, the laser has been an essential tool in medicine. A laser can be used as a scalpel that selectively cuts tissue leaving blood vessels intact, as a tool for targeted annihilation of cancer cells in photo-dynamic therapy and more routinely now, in birthmark and permanent hair removal. The last few years have seen an explosion of cross-discipline research. By bringing physicists, chemists and biologists out of their scientific silos, a transfer of knowledge and understanding between disciplines is allowing scientists to improve upon existing scientific techniques and devices. Here lies the driver for perhaps one of the most exciting branches of scientific research today: biophysics.

Established techniques in biology and physics are being combined to give us innovative solutions and applications. The possibilities seem endless. Within this new discipline, optical micromanipulation has particularly become one of interest to the wider scientific community.

Scientists working in optical manipulation techniques are well acquainted with the name Arthur Ashkin, for it is his pioneering work that was the foundation of this field of research [11] [12]. His first demonstration of optical trapping of a particle in a laser beam showed that it was possible to exploit the forces of light to optically manoeuver particles. This elegant experiment has developed into a major subject of scientific study. By being able to optically trap, guide and bind particles we have a range of established techniques, dubbed the 'optical toolkit', with applications in a range of disciplines including but by no means exclusive to biology, genetics, microfluidics, pharmacology, biotechnology and forensics.

As Ashkin is quoted as saying, some of the *'previously impossible experiments'* have had a *'revolutionary impact'*. The basis of this claim is that light is able to selectively manipulate and interrogate living cells and organisms non-invasively. Furthermore, it is now possible to examine, in vivo, the chemical reactions, physical forces and biological processes without irrevocably damaging the subject of study.

In optical micromanipulation, a laser beam becomes an optical scalpel that can perform cellular microsurgery allowing scientists to learn more about the microscopic intracellular structures and their functions; it becomes an optical

drill which momentarily tears a cellular membrane, permitting fast and targeted molecule and DNA delivery prior to seemingly miraculous self-healing of the membrane [13]. A laser beam can distinguish then sort white blood cells from red blood cells, or identify then select fluorescing samples. In miniature laboratories, a laser beam can become the driver of tiny pumps, valves or cogs on the micrometre scale. How is this possible?

The answer lies in an idea put forward by Einstein. In his research into the quantum nature of light he proposed that light has no mass but can still exert a force. Photons possess and can transfer momentum just as billiard balls on a table can exchange momentum. On a macroscopic scale, the momentum of light is not yet sufficient to significantly influence the motion of objects. However, at and below the microscopic scale, the force of light is capable of influencing quite strongly the motion of certain objects. Conservation of momentum dictates that an optically transparent particle within a light beam can itself influence the light direction and thus change its momentum. The rate of change in momentum p, can be described by

$$F = \frac{dp}{dt} = \frac{md\nu}{dt} \tag{1.5}$$

where dt is the rate of change, m is the particle mass and ν is the particle velocity. This interaction between light and an object is the basis of optical micromanipulation techniques.

Consider two light paths as illustrated in figure 1.5. The on-axis ray, ray 1, has higher photon flux than the off-axis ray, ray 2. The light rays are refracted by their interaction with the optically transparent microsphere. This change of path direction introduces a change in momentum of the photons which by the

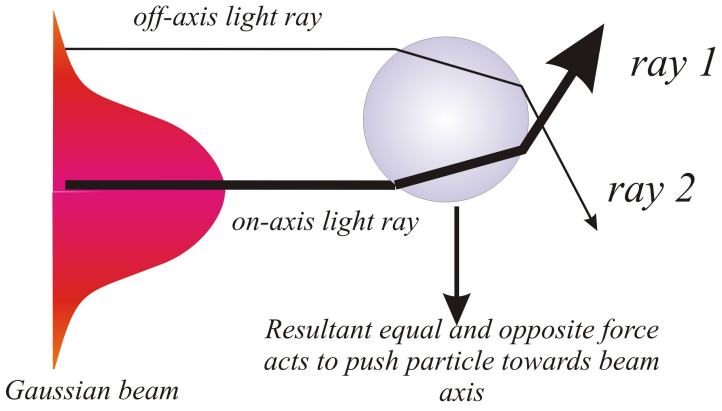

Figure 1.5: The momentum transfer of momentum between light and optically transparent objects can influence the motion of the object. The photons travelling along path rays 1 and 2 exchange momentum with the optically transparent spherical particle. This momentum exchange acts to push the particle in the opposite direction to each refracted ray. Since the flux of photons in the on-axis beam (ray 1) is greater than the off-axis beam (ray 2) net result is to push the beam towards the beam axis where it will stay in a transverse equilibrium

conservation of momentum principle is transferred to the microscopic particle. Due to the imbalance of photon flux there is a resultant force which acts to force the particle toward the region of high intensity which is along the beam axis where, in the absence of other forces, it remains in equilibrium. This effect is the basis of the optical micromanipulation techniques such as tweezing and guiding. In optical tweezing, the particle is confined within a local trap but in optical guiding, the particles are transported along a beam axis. Optical tweezing has been studied extensively and the optical forces are now well understood and characterised [14, 15]. In contrast, optical guiding techniques have been used but not explored fully. Furthermore, most optical micromanipulation techniques have been carried out using cw lasers. In this context, the thrust of my research has been to explore optical guiding techniques using ultrashort-pulsed lasers. The aim is first to better understand the physics of optical guiding and then identify any additional benefits or potential applications of using pulsed laser sources over continuous wave sources and Bessel over Gaussian

beams. Included in this is an ambition to explore multi-photon excitation in optical guiding using ultrashort lasers.

In this thesis I set out to give the reader an introduction and understanding of the science pertinent to my research. This includes the physics of ultrashort pulse generation, multi-photon excitation optical micromanipulation and Bessel beams. These topics will be discussed in the next three chapters. Following from this, a brief review of previous, pivotal experiments in this field is given. From this background and theory the attention moves to the experimental work carried out. This will be detailed in the three subsequent chapters. Finally, to conclude, the work will be discussed with suggestions for further work. To begin, in Chapter 2, we first discuss the generation and applications of ultrashort pulses and multi-photon excitation.

CHAPTER 2

Ultrashort-pulsed lasers: generation & applications

As ultrashort pulses are used throughout my research, it is important to expand on the brief overview given to this subject in the introduction. As my research is primarily concerned with the application rather than the characterisation of ultrashort pulses, the focus here will be on those topics directly relevant to the work. For a more detailed description of ultrashort lasers, the reader is referred to the following references [5, 16, 17]. Here we include a general discussion on pulsed lasers before moving to ultrashort pulse generation by modelocking methods. We shall then move on to the applications of ultrashort pulses and briefly touch on the suitability of femtosecond lasers in biomedical applications. Also, as multi-photon excitation plays an important role in the experimental work carried out an overview of this subject follows. Again this is constrained to those topics of particular relevance.

2.1 Generation of ultrashort pulses

The most common laser is one with a continuous wave (cw) output. These range from tiny semiconductor diode lasers with milliwatt outputs to fibre lasers which can produce powers as high as $100W$ [18]. This means that the power from the laser is released from the cavity constantly with time. As discussed in Chapter 2, multi-photon processes require a high photon flux. To achieve this with cw lasers would require prohibitively costly lasers in terms of pump energies and running costs. Alternatively, if it was possible to somehow contain the energy from a cw laser within the cavity before suddenly releasing it in a single short burst of light, the instantaneous power of the laser would be increased for the duration of the light burst. For the same average output power as a cw laser, it would be possible to achieve high peak powers from periodic bursts of light from the laser. There are many ways to produce bursts or pulses of laser light. The resulting pulses with higher peak powers are sufficient for inducing these multi-photon processes.

As discussed in the introduction, a laser will only produce an output if and when the gain exceeds the cavity losses. In a method called *Q-switching*, a cavity is set up initially with high losses. This allows the pumping process to build up a large population inversion as it tries to reach the lasing threshold. By suddenly switching to a low loss cavity, the energy within the cavity is released as giant pulse of light. The name of the mechanism is related to the quality factor of a cavity, Q, which is a measure of how efficiently the cavity releases the energy within it. A cavity with low losses has a high Q-factor and hence in Q-switching, the laser cavity goes from a low to high Q-factor. This can

be achieved by using active Q-switching techniques such as rotating mirrors, electro- and acouto-optic modulators. Here the quality factor of the cavity is controlled by an external component. In passive methods, the inherent optical properties of an intracavity component are exploited to control the losses within the cavity. One such common method is by saturable absorbers which become increasingly transmitting at higher intracavity powers. As the intracavity power increases, the absorber becomes saturated and increasingly transparent which consequently reduces the losses within the cavity. The production of a pulse results. The pulse repetition for Q-switched lasers is typically 1-100 kHz or higher with pulse durations in the region of nanoseconds. For microchip lasers which are Q-switched with a semiconductor saturable absorber mirror, pico-second pulse durations are obtainable and at megahertz repetition rates. For shorter pulses in the region of pico- and femtoseconds a different approach, called modelocking, is required.

2.1.1 Modelocking

Modelocking is now the most common and efficient method of producing ultra-short laser pulses. Normally a laser operates in a continuous wave fashion. This is because the the axial modes within the cavity oscillate with random phase between one and other to produce a continuous noise-like output. If one can somehow encourage the electric fields to start oscillating in phase, then this leads to the evolution of spikes. To illustrate, in figure 2.1 there are three modes with wavelengths λ_1, λ_2 and λ_3. If the phases are locked together as illustrated then the superposition of the wave trains leads to the development of pulse trains. These are separated in time by the cavity round trip time $2nL/c$

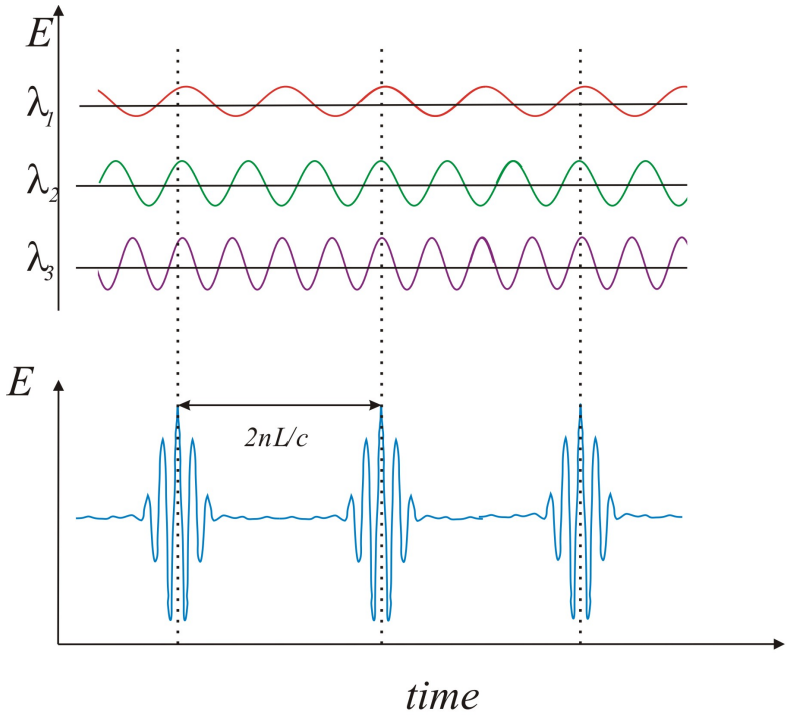

Figure 2.1: Illustration of mode-locking of axial cavity modes to form pulses. Three modes of λ_1, λ_2 and λ_3 are in phase leading to evolution of pulses with a separation in time of $2nL/c$.

where n is the refractive index of the medium, c is the velocity of light and L is the cavity length.

Recalling the bandwidth theorem introduced in Chapter 1, from this illustration it can be deduced that the greater the number of modes that oscillate within a cavity, the shorter the pulse duration can become. However, as stated, a laser normally operates in continuous wave fashion and therefore must be forced to produce pulses in some way. This can be done by applying some kind of

amplitude or phase modulation within the cavity. This modulation can be applied either by some external source in active modelocking or by some other means in passive modelocking.

In active modelocking, intracavity components such as electro-optic or acousto-optic modulators have a modulation frequency set to match a multiple of the round trip frequency of the laser. This means that the pulse is able to complete a round trip of the cavity before returning to the modulating component where the gain or transmission will be at a maximum once again. This ensures that only multiples of this mode are able to propagate within the cavity and hence force modelock operation. These techniques are limited to the frequency of the modulation and are able to produce picosecond pulses. For the shorter pulses that we require, passive techniques are required.

In passive modelocking, there are no external components needed. To take the example of a saturable absorber in the form of an organic dye, these broad bandwidth dyes become increasingly transparent with intensity. A random noise spike in the cavity will experience less loss than smaller oscillations. It will therefore will grow at the expense of the other oscillations within the cavity. An erosion of the leading and trailing edge of the pulses reduces the pulse duration until its bandwidth equals the gain bandwidth of the gain medium. The same process is used in semiconductor-saturable absorber mirrors. Even shorter pulse durations became possible with solid-state materials with broader bandwidth however the pivotal breakthrough came with the demonstration of self-modelocking in 1991 [10].

Self-modelocking is often referred to as Kerr-lens modelocking and exploits self-focussing and self-phase modulation which arise from the Kerr effect as mentioned in Chapter 1. In self-focussing we can consider a pulse with a Gaussian-like spatial profile as it passes through a medium which has a refractive index described by equation 1.4 where the term $n_2 I$ is significant and positive. If the incident wavefront is planar with a Gaussian profile, then the outer portions of the wavefront will increase in speed with respect to those nearer the central more intense part of the pulse. This acts to create a virtual lens within the material which causes the beam to be focused. While this is pivotal in ultrashort pulse generation, the same phenomenon can cause beam break-up and optically induced damage of materials.

Self-phase modulation also results from the nonlinear refractive index change caused by the Kerr effect. The change in refractive index is instantaneous and causes different parts of the pulse, in the temporal domain, to experience different refractive indices. Over many round trips within the cavity a pulse will suffer from increasing spectral broadening. In combination these two effects can be deleterious to pulse generation. In high power lasers they can lead to distortion of the pulse shape to the extent that it can not be amplified by the finite bandwidth of the laser medium. These effects can be managed by maintaining the power of the laser below a distortion-inducing threshold.

However, it was discovered that when a large noise spike is introduced into a laser cavity during normal cw operation, there is sufficient intensity to cause self-focussing within the gain medium. As with the saturable absorber, the noise spike sees less loss in the cavity. An intracavity aperture encourages the laser into pulsed operation. Concurrently self-phase modulation helps to broaden

the pulse and therefore, from the bandwidth theorem, supports the production of pulses with even shorter durations. The limiting factor in producing pulses in this way is the dispersive effects of the optics within the cavity. Dispersion compensation is essential and can be provided either by specially engineered chirped mirrors, or quite commonly by a prism-pair arrangement as shown in figure 2.2.

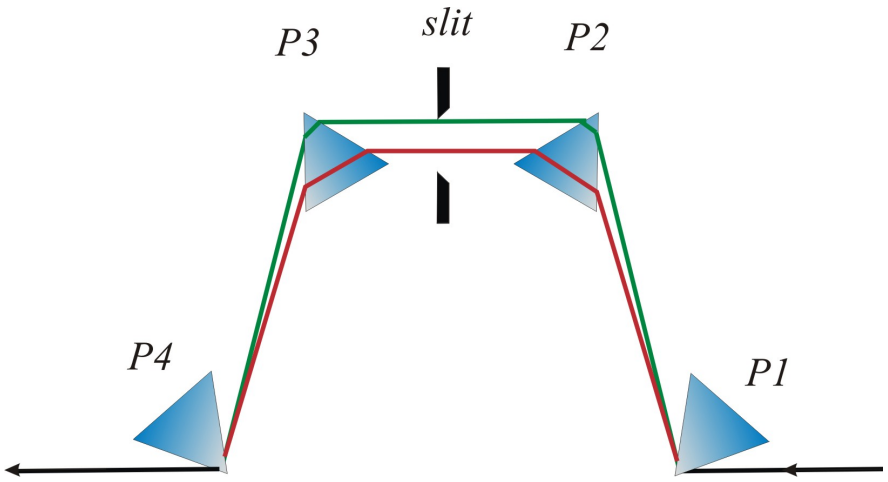

Figure 2.2: A double prism-pair arrangement is used to provide negative dispersion which compensates for the positive dispersion generated by material dispersion and self-phase modulation. The beam incident on prism P1 is refracted into its spectral components and travels through the series of identical prisms P2, P3 and P4. The beam is recombined by P4. Longer wavelength components travel through more optical glass and therefore are subject to greater dispersive effects than the shorter wavelengths.

Pulses as short as $4fs$ have been generated in this way. Efforts continue to produce lasers with pulses of attosecond duration. To reach this many barriers have to be overcome. One of the major impediments is finding a mechanism by which to measure these pulse durations as they become shorter than the time it takes a light wave to complete one cycle.

2.2 Applications of lasers in biomedicine

As mentioned in Chapter 1, many atomic, molecular and chemical processes occur within the picosecond and femtosecond timescale. To enable scientists to investigate these processes in detail some faster event is required and ultrashort laser pulses provide a means of achieving this. In the field of semiconductor spectroscopy, pump-probe experiments have been key in developing theoretical models of semiconductor devices and therefore instrumental in improving their speeds. In ultrafast chemistry, ultrashort laser pulses are used to investigate many chemical processes which occur on a femtosecond timescale such as bond formation and breakage, ionisation, molecular collisions, rotations and vibrations. With the wide variety of laser powers, wavelengths and pulse durations available, there are a huge range of laser parameters to choose from.

In biomedical applications, one aim is to be able to probe and investigate structures within biological tissues. To gain information from these complex structures, the light needs to be able to penetrate the tissues. The depth to which light can penetrate is dependent on the scattering and absorption properties of the tissue.

Consider first the scattering of light in tissue. This occurs as a direct result of the interaction of light with microscopic and macroscopic constituents such as cellular membranes, mitochondria, ribosomes, fat globules and the refractive index mismatching between intra- and extra-cellular fluids [19].

For particles much smaller than the wavelength of the light, Rayleigh scattering dominates and is inversely proportional to the fourth power of wavelength [20, 21]. Mie scattering of particles greater than the wavelength of the light is not wavelength dependent. If there is a high concentration of Mie particles present in a substance, the high levels of scattering is evident in the white opaque appearance of the substance. The combination of Mie and Rayleigh particles in a tissue means that scattering in tissue is reduced at longer wavelengths as illustrated in figure 2.3.

There are four main types of tissue within the body: epithelium, connective, muscle, and nervous tissue. All of these tissues contain water, haemoglobin, proteins and fats to varying degrees. As illustrated in figure 2.3, the combination of the absorption spectra of these tissue components and wavelength-dependent scattering combine to make the near-infrared region of the electromagnetic spectrum particularly amenable to the interrogation of tissue. This region of the electromagnetic spectrum is termed the *therapeutic window*. There are a range of sources which are suitable for working in this part of the spectrum including the Cr:LiSAF and Ti:sapphire lasers used in the experiments detailed in this thesis. One of the benefits of using red and infrared lasers is deeper tissue penetration. However, many of the structures within tissue need to be excited at shorter wavelengths. Cellular structures can also can be tagged with fluorophores which also have absorption and emission spectra in the visible spectrum. Fluorophores will be discussed in more detail in Chapter 7 but here it is important to understand that to excite and image the emission from these these structures, one needs light with wavelengths which map to the absorption spectra. These structures can be imaged using a range of microscopies.

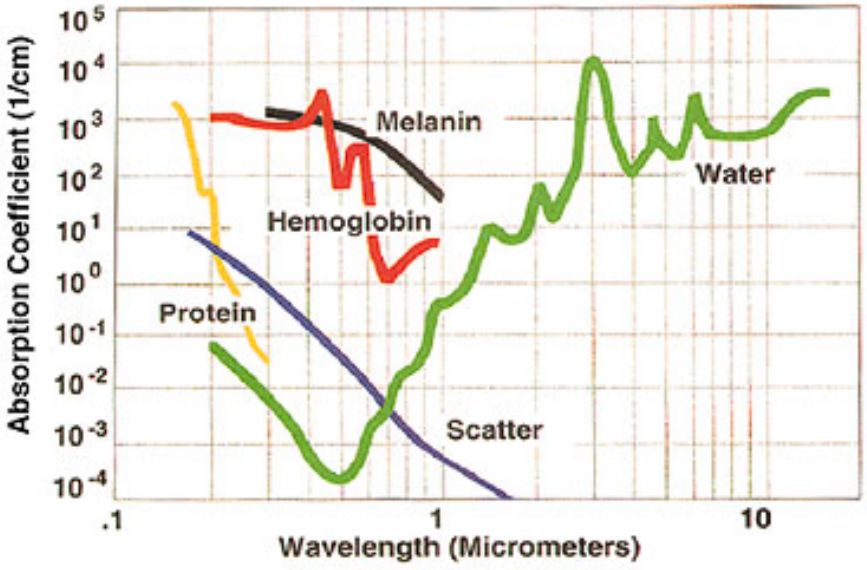

Figure 2.3: Absorption spectra of water, proteins, melanin, haemoglobin show that the region of lowest absorption is between $600nm$ and $1000nm$. Also shown is the wavelength-dependent scattering of particles in tissue.

There are several microscopy-based imaging techniques which can be used to obtain information and an understanding of the structures and processes within biological samples. Conventional techniques include conventional scanning and confocal microscopies. In a conventional scanning microscope, a simple microscope arrangement is modified to allow a light probe to scan over an object. The image is formed by the electric signal measured by a photodetector which captures the reflected or transmitted light. This electronic signal allows quantitative measurements, image processing, analysis and enhancement. This method is usually reserved for imaging 2-dimensional samples. For 3-dimensional imaging of thick biological tissues, a confocal microscope is required. In theory, by placing a small aperture close to the biological sample, resolution is increased at the expense of field of view by rejecting the out of focus contributions. In practice, this higher resolution is achieved by using a point source such as a laser which is focussed onto the sample. The image spot is

then focussed back through the lens and through an aperture which is situated at the conjugate focal plane. Light from object planes away from the focussed image do not converge at the pinhole and therefore is mostly blocked by it. The result is an optical section of the object which can be constructed into a 3-dimensional image by scanning the point source and aperture simultaneously over the sample. Confocal microscopy has been used extensively as an imaging technique since it provides a high-resolution optical sectioning capability however it has some limitations. The aperture which increases the resolution also acts to reduce the signal and hence higher powers are needed for imaging the fluorophores. The downside from this is that the fluorophores will tend to suffer from photo-bleaching. Also, as previously mentioned the excitation of fluorophores by this method requires UV, blue and green lasers which are more quickly attenuated by scattering in the tissue. These shortcomings can be overcome by use of two-photon techniques which use the high-peak power of pulses to result in a smaller volume of excitation, deeper penetration into tissue with a reduction in photo-bleaching and photo-damage. The two-photon excitation phenomena are discussed further in the next section. Suffice it to say, in microscopy-based imaging techniques, ultrashort pulses are fundamental in providing higher resolution images at deeper penetration.

Another imaging technique called fluorescence life-time imaging (FLIM) allows real-time imaging and spatial mapping of a fluorophore within a cell or tissue [22, 23]. This uses the fluorescence lifetime of a fluorophore as an imaging mechanism. The lifetime of a fluorophore is related not to the concentration or intensity of the fluorescence but to its environment. By using ultrashort pulses to excite the fluorophores measurements of the lifetime can be used to differentiate between healthy and cancerous tissue. One of the key applications in

biomedicine has been the development of photo-dynamic therapy (PDT). In this cancer treatment, a photo-sensitive chemical which is designed to preferentially congregate in tumours is injected into tissue. This chemical is activated using light from a laser which causes the generation of singlet oxygen. Singlet oxygen promotes cellular death and therefore kills the cancerous cells. The process was first carried out using single photon absorption but recently, two-photon excitation photo-dynamic therapy has been investigated as an alternative method [24]. The production of singlet oxygen which is beneficial in this application is an unwanted effect in others [25, 26]. Using infrared femtosecond lasers has been shown to induce cell death and inhibit cell division. The benefits of multi-photon microscopies of increased resolution, decreased photo-damage and photo-bleaching are balanced by this deleterious effect. This must be considered in choosing a suitable laser for use in biomedical applications.

There are many nonlinear effects that are of interest to scientists, however, the research detailed within this thesis is primarily concerned with that of two-photon excitation-induced fluorescence and second-harmonic generation. Both phenomena involve the interaction of atoms with two photons but the processes and the resulting emission are subtly different. These will now be discussed in the following sections.

2.2.1 Two-photon excitation-induced fluorescence

When a single photon is absorbed by a molecule, an electron is excited to a state which is higher by an energy equal to the photon energy. In 1931 Goppart-Mayar

hypothesised that two-photon absorption could take place [27]. Simultaneous absorption of two photons would require the presence of two photons of the same state at the same point in space and time. In fact as Denk et al. reported in their 1997 paper on the subject, a fluorophore exposed to bright daylight may be excited by a one-photon absorption once a second. In contrast it will be spontaneously excited by a two-photon absorption once every 10 million years [28]. Hence, the first practical demonstration of two-photon excitation by Werner Kaiser, which had to wait until the advent of the laser, came in 1961 [29].

Given a high enough flux of photons, two are absorbed almost simultaneously by the electron which is then excited to a higher energy state. This excited state is higher by the sum of the two photon energies. The molecule relaxes via non-radiative processes to slightly lower energies within the higher state. The fluorescence which results from the radiative relaxation has an energy lower than the sum of the energy of the absorbed photons. The non-radiative transitions within the molecular energy levels also act to broaden the emission spectrum. A slight increase in the incident photon energies results in an emission wavelength which is Stokes-shifted to a longer wavelength. The fluorescence is emitted isotropically as illustrated in figure 2.4. The reduction of photo-bleaching and photo-damage arises from the fact that the excitation can only occur in regions of high intensity such as the beam focus. As mentioned previously, when this technique is combined with microscopy techniques, the resulting images have a higher resolution [30]. For imaging purposes, fluorescing molecules typically emit in the visible spectrum ($400 - 700nm$). To repeat, the benefits of using pulsed laser sources in the infrared ($700 - 1000nm$) means exploiting multi-photon excitation and deeper penetration of tissues due to

decreased scattering at these longer wavelengths [6].

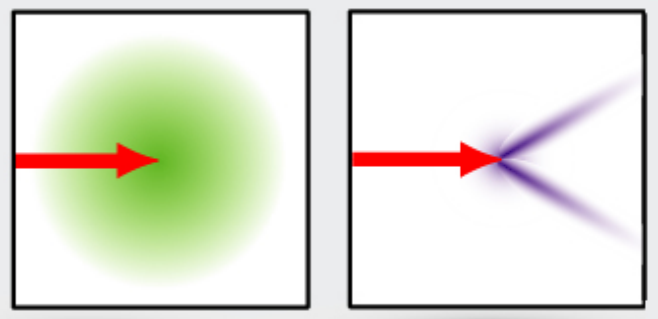

Figure 2.4: The incident radiation (red arrow) generates two-photon excitation-induced fluorescence (green) which is isotropic(l) compared to the directional nature of second-harmonic generated radiation (blue)(r).

2.2.2 Second-harmonic generation

In contrast with two-photon excitation-induced fluorescence, multi-harmonic generation arises from the optical properties of a material. Different materials have different properties and therefore exhibit varying levels of multi-harmonic generation. These properties are described by a nonlinear susceptibility tensor. For second-harmonic generation, the tensor has 27 components which results in an electric polarisation of the electric field which is dependent on the various components of the electric field. Second-harmonic generation only arises in materials with a non-centrosymmetric crystal structure such as Potassium Titanyl Phosphate, KTP, or Lithium Niobate, $LiNBO_3$. Third-harmonic generation can take place in structures which are either centrosymmetric or non-centrosymmetric. However, this requires the simultaneous absorption of three or more photons and the probability of this event occurring is even less than that of two-photon absorption. In multi-harmonic microscopies third

and second harmonics of the fundamental laser wavelength can be generated in structures such as collagen, elastin and muscle. It has also been used in the imaging of surfaces, microtubules, tumours and in *in-vivo* developmental biology.

In this form of excitation, multiple photons interact simultaneously with a molecule with no absorption events. N-photon harmonic generation is primarily a scattering process which produces an emitted wavelength of exactly 1/N times the incident photons. Here we are concerned primarily with second-harmonic generation which was first demonstrated by Franken et al. in 1961 [31]. By focussing a ruby laser with a wavelength of $694nm$ into a quartz crystal and analysing the output light through a spectrometer, they were able to record the spectrum on photographic paper, which confirmed the production of light at $347nm$. Second-harmonic generation is a special case of frequency mixing which arises from the nonlinear response of the polarisation:

$$P(t) = \chi^{(1)}E(t) + \chi^{(2)}E^2(t) + \chi^{(3)}E^3(t) + \cdots \tag{2.1}$$

For frequency-mixing processes it is the second-order term which is key. By writing the time-varying electric field as

$$E(t) = E_1 e^{i\omega_1 t} + E_2 e^{i\omega_2 t} + \text{c.c.} \tag{2.2}$$

where c.c. denotes the complex conjugate of two incident beams E_1 and E_2 the second-order polarisation becomes

$$P^{(2)}(t) = \sum \chi^{(2)} n_0 E_1^{n_1} E_2^{n_2} e^{i(m_1\omega_1 + m_2\omega_2)t} + \text{c.c.} \tag{2.3}$$

where the summation is over

$$n_0 \in 1, 2$$

$$n_1, n_2, m_1 \in 0, 1, 2$$

$$m_2 \in 0, -1, 1, 2$$

From this, there are six non-degenerate combinations of the paramters n_0, n_1, n_2, m_1, m_2 which relate to six different possibilities of frequency mixing: second harmonics of E_1 or E_2, optically rectified signals of E_1 and E_2, the difference frequency $\omega_3 = \omega_1 - \omega_2$ and the sum frequency $\omega_3 = \omega_1 + \omega_2$. In the case of $\omega_1 = \omega_2$, the emitted radiation is the second harmonic of the incident radiation. All these frequency-mixing processes are sensitive to the relative phases of the incident and generated beams. For efficient frequency mixing to take place effective and efficient *phase-matching* is required. Phase-matching plays a key role in the success of some of my experimental work which is detailed in Chapter 7 and will be explained here.

Phase-matching can be understood by considering a travelling wave described by

$$E_j(\mathbf{x}, t) = e^{i(\omega_j t - \mathbf{k}_j \cdot \mathbf{x})} \tag{2.4}$$

with $\mathbf{k_j} = n(\omega_j)\omega_j/c$ where c is the velocity of light and $n(\omega_j)$ is the refractive index of the medium at the angular frequency ω_j. Thus equation 2.3 becomes

$$P^{(2)}(\mathbf{x}, t) \propto E_1^{n_1} E_2^{n_2} e^{i\omega_3 t - (m_1 \mathbf{k_1} + m_2 \mathbf{k_2})x} \tag{2.5}$$

From this it can be deduced that the second-order polarisation gives rise to a radiated field at angular frequency ω_3 and its corresponding wave vector is $\mathbf{k_3} = m_1\mathbf{k_1} + m_2\mathbf{k_2}$. The phase-mismatch between the three wave vectors $\Delta\mathbf{k}$

can be expressed as

$$\Delta\mathbf{k} = \mathbf{k_3} - m_1\mathbf{k_1} + m_2\mathbf{k_2} \tag{2.6}$$

In the case of second harmonic generation, $m_1 = 2$ and $m_2 = 0$, and from the condition $\omega_1 = \omega_2$ then $\mathbf{k_1} = \mathbf{k_2}$ to give the relationship

$$\Delta\mathbf{k} = \mathbf{k}_{2\omega} - 2\mathbf{k}_{\omega} \tag{2.7}$$

The aspiration is for the $\Delta\mathbf{k} = 0$ as this will give the most efficient frequency con-

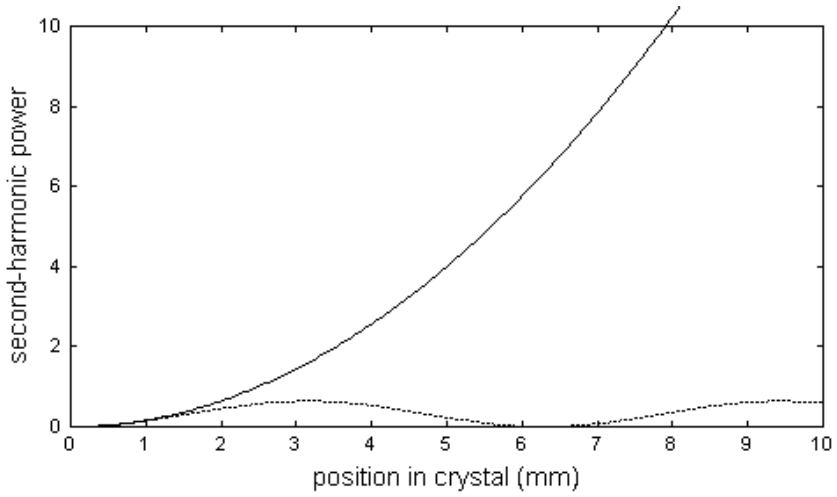

Figure 2.5: The second-harmonic generated signal is dependent on the phase-matching conditions. The dotted line shows how the SHG signal oscillates between a low value and zero. The solid line shows how the SHG signal grows along the direction of propagation when phase-matching conditions are met[32].

version. As shown in figure 2.5, without phasematching, the second-harmonic signal will oscillate between zero and a small value [33]. This can be understood by considering how the second-harmonic signal propagates along the z axis of medium of refractive index, n.

$$P(2\omega)e^{1k_{2\omega}t} \propto E_{\omega}E_{\omega}e^{i2k\omega t} \tag{2.8}$$

Under steady state conditions, $d/dt = 0$ the second-harmonic electric field will vary along a the crystal length according to the expression

$$\frac{dE_{2\omega}}{dz} \propto E_{\omega}E_{\omega}e^{i\Delta kz} \tag{2.9}$$

Integrating over the length of the crystal yields the expression

$$E_{2\omega}|_{z=l} \propto E_{\omega}^{2} l sinc(\frac{\Delta kl}{2}) \tag{2.10}$$

The intensity of the radiation can then be described by the relationship

$$I_{2\omega} \propto I_{\omega}^{2} l^{2} sinc^{2}(\frac{\Delta kl}{2}) \tag{2.11}$$

Under these conditions, the intensity will be vary between zero and unity. Forconditions where $\Delta kl/2$ is large this can be rewritten as

$$I_{2\omega} \propto I_{\omega}^{2}(\frac{2}{\Delta kl})^{2} l^{2} \sin^{2}(\frac{\Delta kl}{2}) \tag{2.12}$$

For conditions where $\Delta kl/2$ is small, then the $sinc^{2}(\Delta kl/2)$ approaches unity and hence the second-harmonic generated field is optimised. By employing phasematching techniques the second harmonic signal will grow quadratically along a crystal axis.

The direct relationship between incident photon energy and generated radiation means that when the excitation frequency, ω, is changed, the emission wavelength maintains the harmonic relationship, 2ω. Again in contrast to two-photon excitation-induced fluorescence, the emitted light is coherent and therefore must satisfy phase matching constraints. In multi-photon microscopy

the second-harmonic signal retains the phase information and emits with a directionality dependent on the nature of the scatterers as illustrated in figure 2.4. In both cases, however, the emitted radiation has an intensity, $I_{2\omega}$ which is proportional to the square of the incident power P_{ω}

$$I_{2\omega} \propto P_{\omega}^2 \tag{2.13}$$

Second-harmonic generation and two-photon excitation-induced fluorescence as optical imaging techniques can, in combination, provide important information about a tissue sample. It is possible to perform two-colour multiphoton microscopy by tailoring the excitation wavelength in such a way as the second-harmonic generated radiation is sufficiently far from the fluorescence wavelength [34, 35, 36].

2.3 Discussion

Femtosecond lasers have, until now, not been used to any great extent in the field of optical micromanipulation. Since the vision here is to explore their use in combining multiphoton excitation techniques with optical guiding we need to understand some of the properties and existing applications of these ultrashort pulses. Therefore, in this chapter we have discussed the generation of ultrashort pulses by modelocking techniques. Since this work was carried out as part of a wider brief to potentially develop biomedical applications, an overview of applications for these pulses was geared towards those in the biophysics. For this reason, a discussion of the suitability of lasers sources was included. From

discussing what comprises an important part of the experimental work, to another: optical micromanipulation techniques. We will now visit this in the next chapter.

CHAPTER 3

Optical micromanipulation

In this chapter we will discuss in more detail the radiation pressure of light and the forces that act on an optically transparent particle either to trap or to guide it within a light beam. Optical trapping has been well characterised and hence it will not be discussed in detail here. The reader is referred to elsewhere for a more thorough treatment of this topic [4, 14, 15, 37, 38]. We will instead concentrate on optical guiding techniques as this has not been subject to the same level of study. Understanding the physics of this technique more fully underpins much of the research detailed in this thesis.

3.1 Forces acting on a particle within a light beam

Here we look at the forces which act on an optically transparent particle within a beam. Figure 3.1 shows the main forces which govern the motion of a particle within a light beam. The optical gradient force will act to confine the particle within the beam but has to compete with a number of other forces. Of these, the

simplest to understand and quantify is the force due to gravity as it is a function of the mass of the particle. Second, if the particle is not held within a vacuum, it will also be subject to the forces of convection, diffusion and buoyancy. These forces relate to the volume, surface area and relative mass of the particle in its carrier medium. If a the scattering force is sufficient to propel a particle along a beam, then it will experience an opposing force known as Stokes drag. This is related to the viscosity of the medium,η, the particle radius, r, and its velocity, v.

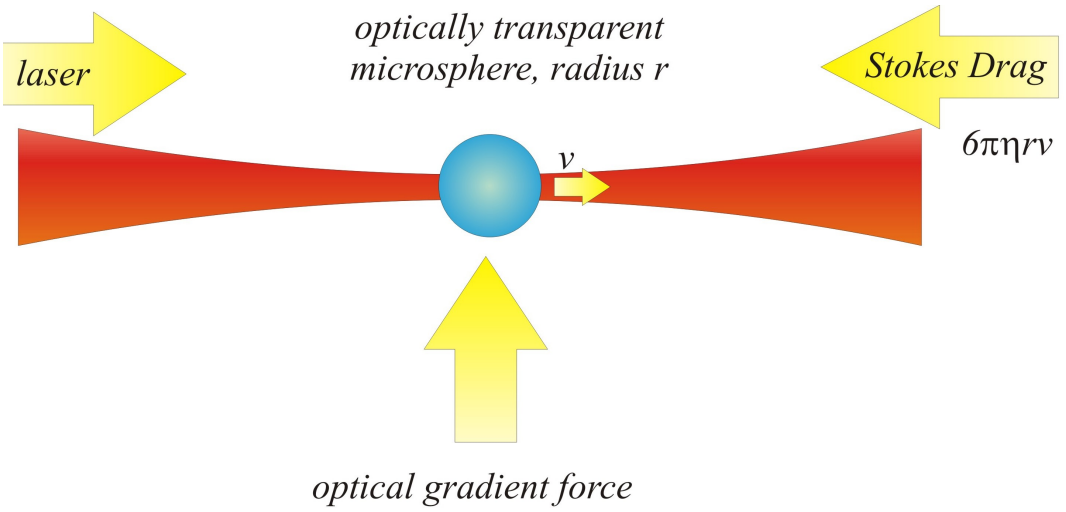

Figure 3.1: The main forces acting on a particle radius r travelling at velocity,v, within a beam are gravity, heating, scattering and gradient forces. The Stokes drag, $6\pi\eta, rv$ also acts to retard the forward motion of the particle.

More difficult to quantify are the scattering and gradient forces. In optical trapping experiments it is the gradient force which dominates to confine a particle within a trap. Conversely, it is the scattering force which dominates the motion of a particle in a beam. Modelling and subsequent quantification of the scattering and gradient forces relies not on the absolute size of the particle

but on its size in relation to the radiation wavelength. As mentioned in the introduction, it is possible to trap and guide a wide range of particle sizes. In understanding the physics of optical micromanipulation it is the relative size of the particle r compared to the wavelength, λ of trapping or guiding beam that is important. There are two main regimes which have been modelled that are of interest in optical micromanipulation. The first is the Mie regime where the particles have a radius r which is approximately of the order of 10λ or more. In contrast, in the Rayleigh regime, the particle radius r, is of the order of $\lambda/10$. In the following sections, after discussing generally the forces acting on an optically transparent particle, we will discuss in more detail the Mie and Rayleigh regimes before turning some attention to the intermediate regime where the optical forces are not so easily analysed or described.

3.2 The Mie regime

When Ashkin first demonstrated optical trapping of biological particles he used an infrared (IR) beam to trap a cell of approximately 5 microns [39]. He later developed a model to support his observations by considering a ray-optics approach. This model was found to be valid for particles in the Mie regime, where particles have a radius r, larger than the wavelength of the laser, λ [40].

In the Mie regime, the physics of optical trapping can be explained by considering photons of frequency ν to have linear momentum $p = h\nu$. When a photon interacts with an object it can refracted or scattered. If the photons undergo a change of direction then the momentum undergoes a parallel change. Total

momentum must be conserved therefore any change in momentum of the photon must be transferred to the object. A change in momentum, p produces a force

$$F = \frac{dp}{dt} \tag{3.1}$$

where F is the force, dp is the change in momentum and dt is the change in time. If the object is small enough, like a microscopic particle, then even picoNewton forces will impel the object to move. To illustrate this, consider a spherical particle placed off-axis in a laser beam that has an intensity gradient, as shown in figure3.2, it will be forced towards a point of equilibrium. In this case the point of highest intensity is at the beam axis.

This can be explained by considering two ray paths passing through the sphere, $abcd$ and $ABCD$. Path $abcd$ is of lesser intensity and hence contains fewer photons per unit time than path $ABCD$. The paths are refracted as they cross the air-particle-air boundaries. The change in direction effects a change the photons' momenta. Since momentum must be conserved, from equation 3.1 a force is generated. This is illustrated in figure 3.2 by the resultant vectors$\vec{pq}$ and $\vec{PQ}$. Since $\vec{PQ}$ is greater than $\vec{pq}$, the resultant force acts to push the particle to the beam axis where it reaches a transverse point of equilibrium.

By introducing an axial gradient in intensity, a similar argument can be used to understand how particles are trapped near the focus of the beam. Again consider the path $ABCD$ shown in figure 3.3 (i). The momentum change of the photons following this path gives rise to a force $\vec{PQ}$ figure 3.3 (ii). Due to symmetry, another force $\vec{RS}$ is also produced which, combined with $\vec{PQ}$ gives a resultant force that pushes the particle up towards the focus of the beam

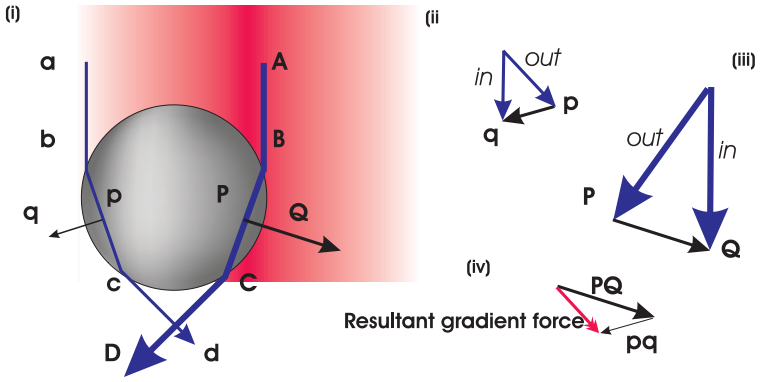

Figure 3.2: (i) A particle is off-axis in a laser beam which has a gradient in intensity. Two rays are shown *abcd* and *ABCD*. (ii) The change in momentum of *abcd* gives force $\vec{pq}$ and (iii) the change in momentum *ABCD* gives force $\vec{PQ}$. (iv) The resultant force from gradient in intensity is shown to push the particle toward the region of higher intensity.

figure 3.3 (iii). Here, a spherical particle with a refractive index, n greater than that of the surrounding medium, n_m, has been considered. However, the same argument can be used to show that hollow spheres or bubbles of material with a refractive index lower than n_m are repelled to a local minimum in the beam intensity profile. In the case of a Gaussian beam, this means that hollow particles will be pushed out of the beam. This sensitivity of optical trapping to the relative refractive indices has been put to good effect, for example, in optical sorting of polymer microspheres and of red and white blood cells [41, 42].

3.3 The Rayleigh regime

In this section we discuss the forces which act to trap a particle which is much smaller than the wavelength of the trapping beam. Understanding the interaction of these small particles with light has traditionally been of interest to

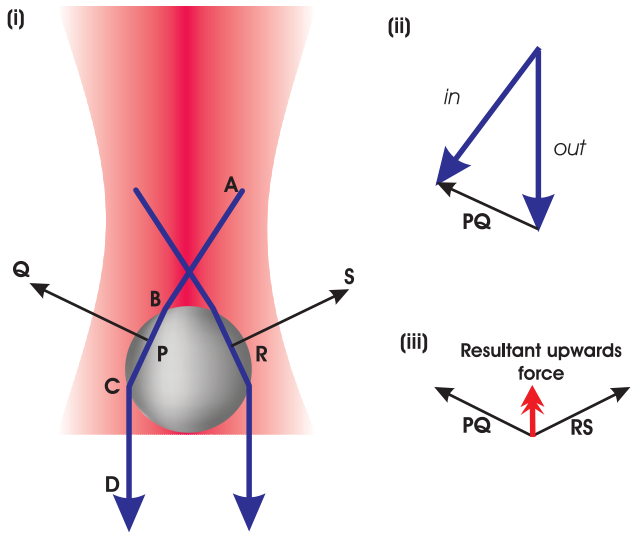

Figure 3.3: A particle below the focus experiences two symmetrical forces $\vec{PQ}$ and $\vec{RS}$(ii), the resultant of which acts to push the particle towards the region of greatest intensity which is along axis of the beam focus.

atmospheric physicists. For optical physicists, the same Rayleigh scattering plays a dominant role in optical guiding and a lesser role in optical trapping.

In the Rayleigh regime, the particle is very small relative to the incident radiation and a distinction between reflection, refraction and diffraction can no longer be made thus a ray optics approach is no longer valid. However, the relative size of the particle means it can be viewed as a tiny perturbation to the incident radiation wavefronts. The particle can be viewed as an induced dipole that obeys the laws of electromagnetism.

From electromagnetism theory, introducing a polarisable particle to an electric field will cause a decrease in the electric field over the particle volume. Since the beam has a variation in its electric field profile, the change in electric field caused by the presence of the particle will also depend on the position of the

particle within the beam. Noting that particle may be neutrally charged, the electric field will induce a dipole force. This dipole force acting on the particle is given by equation 3.2

$$F = -\nabla U \tag{3.2}$$

where U is the potential energy. For a particle with a higher refractive index than its surrounding medium, the particle has a positive relative polarisability, α. Therefore, applying an external electric field, E to the particle will induce a dipole moment, ρ quantified by equation 3.3

$$\rho = \alpha E \tag{3.3}$$

The resulting dipole moment is defined as the product of the induced dipole charges, q and the distance d, separating them

$$\rho = qd \tag{3.4}$$

Hence, it follows that the net force on a dipole depends not on the strength of the electric field but on the gradient in E as given by

$$F = (\rho.\nabla)E = \alpha E.\nabla E = \alpha \nabla E^2 \tag{3.5}$$

That the induced dipole will cause a particle, with a positive relative polarisability, to be directed towards the region of maximum intensity can be deduced from equation 3.5. From equation 3.3 we can intuit that the electric field will act to confine the particle in a potential energy trap. As with the Mie regime, it is the gradient intensity of the electric field that causes the particle to be confined at a region of local maximum intensity. When referring to the Rayleigh regime, this gradient force is often known as the dipole force. For Rayleigh particles,

this dipole force is weak and the scattering force is dominant in the interaction. Hence, while the dipole force draws the particle to the central maximum, the scattering force will simultaneously push the particle in the direction of the beam propagation.

To model the scattering and dipole forces in the Rayleigh regime, it is useful to consider a particle in weakly focused Gaussian beam. If the light rays are assumed to be planar wavefronts and approximately parallel to the propagation beam axis and $\lambda \ll w_0$, expressions for the scattering and dipole forces (equations 3.6, 3.7) can be derived [43].

$$F_{dipole}(r) = 2\pi n_h^2 \epsilon_0 a^6 \left(\frac{m^2-1}{m^2+2}\right) \nabla |E^2(r)| \tag{3.6}$$

Here, m is the ratio of the refractive indices of the particle n_p and the host medium n_m, such that $m = n_p/n_h$. The permitivitty of free space is denoted by ϵ_0, the electric field component by $\vec{E}(\vec{r})$ and a is the particle radius. Again, the scattering force originates from the change in momentum of the light due to scattering from the particle and can be described by

$$F_{scatt}(r) = \frac{n_h}{c} \frac{128\pi^5 a^6}{3\lambda^4} \left(\frac{m^2-1}{m^2+2}\right) \nabla |I(\vec{r})| \tag{3.7}$$

where the light intensity $I(r)$ is determined by the number of incident photons per unit time and area and is related to the electric field vector by

$$I(\vec{r}) = \frac{n_h \epsilon_0 c}{2} \vec{E}(\vec{r})^2 \tag{3.8}$$

From equations 3.7 and 3.8 we can see that the magnitude of these forces in relation to the particle size are $F_{scatt} \propto a^6$ and $F_{dipole} \propto a^3$. Therefore the significance of the scattering force is dependent on the size of the particle. For stable optical trapping to occur, F_{dipole}/F_{scatt} must be greater than unity. Now, having considered the two extremes of particle modelling, the regime where particles are of the same order of magnitude as the laser wavelength must be considered. This will be discussed in the following section.

3.4 Generalised Lorentz-Mie theory & other models

In sections 3.2 and 3.3, we looked at the Mie and Rayleigh regimes which are able to model the conditions where $r \gg \lambda$ and $r \ll \lambda$. Given an experiment where a laser wavelength of $800nm$ is used to micromanipulate $1\mu m$ particles, these models no longer hold true. However, the intermediate region where $r \approx \lambda$ is far more complex to model. Despite this, an attempt to model this has been undertaken by Malagnino et al. with the Generalised Lorentz-Mie Theory (GLMT) [44]. The GLMT model is an extension of the Mie approach where the force can be described by $F(r)$,

$$F(r) = \frac{n_h}{c} I_0 \left[\vec{x} C_{pr,x}(r) + \vec{y} C_{pr,y}(r) + \vec{z} C_{pr,z}(r)\right] \tag{3.9}$$

where $C_{pr,i}$ represent the incident light on the cross-sectional area of a spherical particle The intensity I_0 is given by

$$I_0 = \frac{2P}{\pi \omega^2} \tag{3.10}$$

where ω_0 is the beam waist and P is the incident power. The factor 2 arises from the assumption that the light is reflected along the same path as the incident light.

To summarise, it is the relative size of the particle to the laser wavelength that is important in modelling the optical forces. Regardless of the model used, however, the importance in quantifying the strength of optical forces lies in the potential applications. For example, a simple optical trap can be calibrated to become a useful tool in biological applications such as in the measurement of intramolecular forces.

3.5 Convection & diffusion

In the previous sections we looked at the gradient (or dipole) and scattering forces which act on a particle located within a laser beam. Now, let us consider two other effects which can affect the motion of a particle in a beam: convection and diffusion. These effects influence any optical guiding experiment and are discussed briefly here. Convection arises from the absorption of laser light in a medium. Diffusion arises from the Brownian motion of particles in a vapour or liquid. If a pulsed beam is used to trap or guided a beam then an important consideration is the repetition rate of the laser. If the repetition rate is too low then there may be enough time between pulses for a particle to diffuse out of the beam. Diffusion times of a particle must be considered when choosing a

laser for optical trapping and guiding as it may become difficult to maintain trapping or guiding at low repetition rates.

In optical trapping, the gradient force is usually large enough to dominate the heating effects, but in optical guiding the weaker scattering forces can conflict with the convective forces. The heating effects cause particles to rise in the medium before falling under gravity to interact with the guiding beam. For this reason, in optical guiding, some convection is useful as it maintains a continuous flow of particles within the guiding beam. Conversely, overly-strong convection forces can overcome the scattering forces needed to guide the particles along the propagation axis. Convection forces are governed by the absorption of both the particles and the medium. In turn, absorption of most materials is wavelength-dependent. As we will see in Chapter 6, when using water as a guiding medium, lasers with wavelengths in the infrared region of the spectrum can induce significant heating effects. For this reason, the laser wavelength of the guiding beam must be chosen carefully.

3.6 Discussion

In this chapter we have discussed the topic of optical micromanipulation. In brief we looked at the forces that act on a particle to locate it or guide it within a light beam. The key point from this is to consider the Mie and Rayleigh regimes when considering optical trapping and guiding. In each case a particle will undergo a propulsion towards a region of maximum intensity. Optical trapping in a fundamental Gaussian beam has been extensively modelled while optical

guiding has been barely been investigated in comparison. The little that has been investigated has been primarily in Gaussian beams. The guiding distances of these Gaussian beams are limited because of their diffractive nature. Hence there has been increasing interest in other beam shapes such as Laguerre-Gaussian and bottle beams[45, 46, 47]. However, there is one beam that has been shown to offer extended guiding distances over many others and is is the subject of much exploration in the research detailed in this thesis. The 'non-diffracting' Bessel beam is the next topic to come under the microscope in Chapter 4.

CHAPTER 4

Bessel beams: generation & properties

Optical trapping has been well studied over the past three decades [48, 49, 50, 51]. In this time there has been some interest in using non-Gaussian beams for this application. One such beam, the Bessel beam, has been the subject of considerable study over the past decade as its properties have led the development of some interesting applications [52, 53]. These properties include having a non-diffracting propagation and the ability to self-heal around an object. In this chapter we shall discuss the Bessel beam and its unique properties, some methods of generating a Bessel beam and in particular its reconstruction characteristics. First though, a short overview of the Gaussinan beams to which the Bessel beam is often compared is included.

4.1 Gaussian beam propagation

The fundamental Gaussian beam is recognisable by a single spot with an intensity profile which is described mathematically by a Gaussian function. Its

maximum is centred along the beam propagation. This beam diverges from its beam waist w_0, at an angle θ which for a beam of wavelength λ is expressed as

$$\theta = \frac{\lambda}{\pi w_0} \tag{4.1}$$

This divergence property leads to another important parameter which describes the how quickly the beam diverges. Known as the the Rayleigh range, Z_R, this is defined as the distance over which the cross-sectional area of the beam waist doubles and is given by

$$Z_R = \frac{\pi w_0^2}{\lambda} \tag{4.2}$$

The Rayleigh range is particularly useful for comparing a Gaussian beam with other beams. As an example, for a laser wavelength of $800nm$ and a beam waist of $3\mu m$, the Rayleigh range of a Gaussian beam is $35\mu m$ with a divergence angle of $4.9°$. For the purposes of trapping, a Gaussian beam with these parameters may indeed be useful. However, for guiding purposes, this is a short distance. By using other beams, such as Bessel beams, it is possible to generate extended propagation distances.

4.2 Propagation-invariant Bessel beams

Leaving Gaussian beams aside for the moment, let us now discuss the Bessel beam. It is easily recognisable by its transverse slice profile which shows a central spot of encircled by a series of rings as shown in figure 4.1. Taking a longitudinal slice along its beam axis will reveal that this central spot is a long rod which far exceeds the Rayleigh range of comparable Gaussian beams.

Like Gaussian beams, Bessel beams can be mathematically derived as exact solutions of the Helmholtz equation.

$$\nabla^2 \mathbf{E} + k_0 n^2 \mathbf{E} = 0 \tag{4.3}$$

where the electric field vector is $\mathbf{E} = \mathbf{E_0} \exp[i\omega t - kr]$ and k_0 is the wavevector in free space with refractive index n. The field distribution of the zeroth-order solution can be described by

$$E(r,t) = E_0 exp(-i(\omega t - k_z z)) J_0(k_r r) \tag{4.4}$$

where J_0 is the zeroth-order Bessel function, k_r and k_z are the radial and longitudinal components of the wave vector **k**. Thus the beam derives its name from the Bessel function which forms part of the expression describing its electric field distribution. From this it can be seen that for propagation in the z-axis, there is no change in the transverse profile and hence it is often described as being diffraction-free. A more satisfactory description that has been coined is *propagation-invariant*. It is this propagation-invariant property which has caused much of the interest in Bessel beams.

This ideal Bessel beam has an infinite propagation and a bright central spot of radius r_0

$$r_0 = \frac{2.405}{k_r} \tag{4.5}$$

surrounded by an infinite series of concentric rings. The power distribution is such that each ring contains the same power as the central spot. This property has been used to good effect in optical sorting techniques. The central spot and ring structure does not change with propagation distance however, in

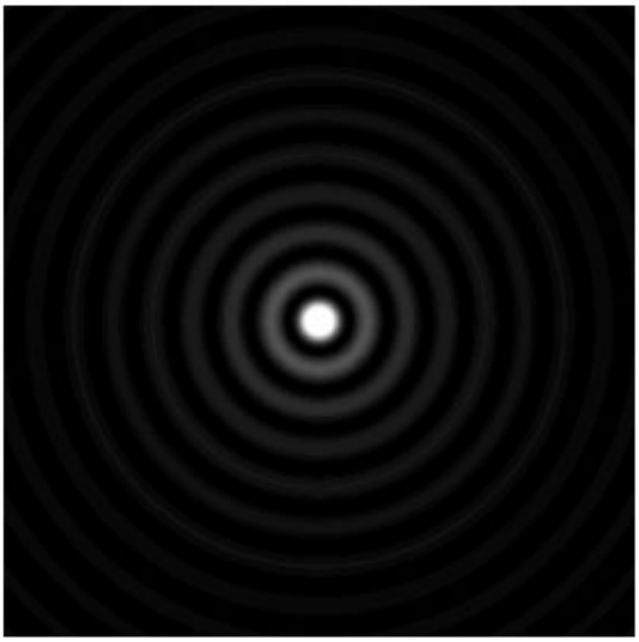

Figure 4.1: The central spot and concentric ring structure of a zeroth-order Bessel beam is evident in its transverse cross-section

practice, the intensity of the beam will vary with distance as the input beam diameter and power is limited. To achieve an ideal Bessel beam would require an infinite plane wave so the result is a limited propagation distance z_{max}. By using a geometrical approach it the propagation distance can be estimated to be approximately

$$z_{max} = R\frac{|\mathbf{k}|}{k_r} \tag{4.6}$$

when R is the radius of a hard aperture through which a plane wave illuminates a special optical element used to generate Bessel beams called an axicon. If the axicon is placed at waist w_0 of Gaussian beam the propagation distance can be approximated by

$$z_{max} = w_0\frac{|\mathbf{k}|}{k_r} = \frac{k}{2.405}w_0 r_0 \tag{4.7}$$

From these relationships it can be seen that the beam propagation is maximised by increasing either incident beam diameter R or w_0, or reducing the radial

component of the wavevector k_r. In practice this means by somehow 'focussing' the Bessel beam less strongly.

4.3 Self-healing properties of a Bessel beam

Aside from its comparatively long propagation distance, the Bessel beam is becoming increasingly appreciated for its self-healing properties. The idea that the Bessel beam is able to reform around objects can be understood if one considers it be created by an interference pattern from a set of plane waves propagating on cone. Each propagating wave undergoes a phase shift$k_z \Delta z$ over a distance Δz. This decomposition of the Bessel beam into plane waves leads to an angular spectrum of the beam. An alternative view is to consider the beam properties in k-space where it forms a ring. From this we can derive the

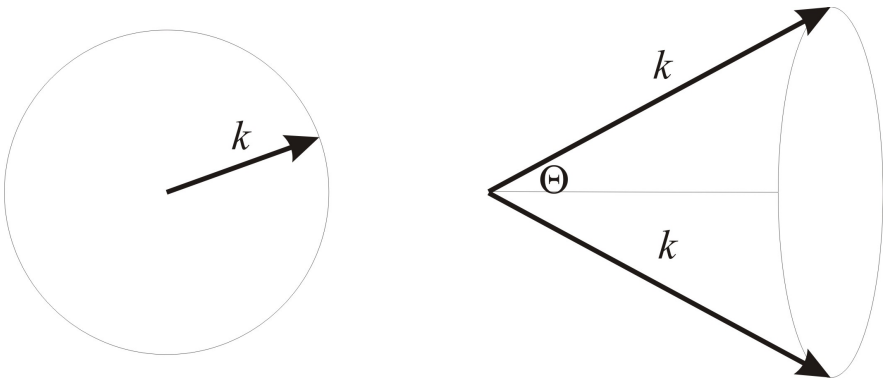

Figure 4.2: The Bessel beam has an angular spectrum which forms a ring when viewed in k-space (left). The k-vectors of wavefronts which form a Bessel beam are shown to form a cone (right).

Equation 4.5. Similarly, it may be possible to see that if an obstacle is placed at the centre of the beam, those wavefronts that are not obstructed can move past

the obstacle and start to reform the beam. From a simple geometric argument this reconstruction distance can approximated to

$$z_{min} = \frac{ak}{2k_z} \tag{4.8}$$

where a is the diameter of the obstruction. In an bid to demonstrate this self-healing property, a numerical simulation was developed by other researchers within the group [54]. An image generated from this simulation is shown in 4.3. The Bessel beam is 'mathematically' generated by a conical lens known as an axicon. The beam is shown to form to the right of the axicon until it meets the 'mathematical' obstruction. The reconstruction of the beam can be seen to the right of the obstruction. This reconstructive property has been demonstrated to

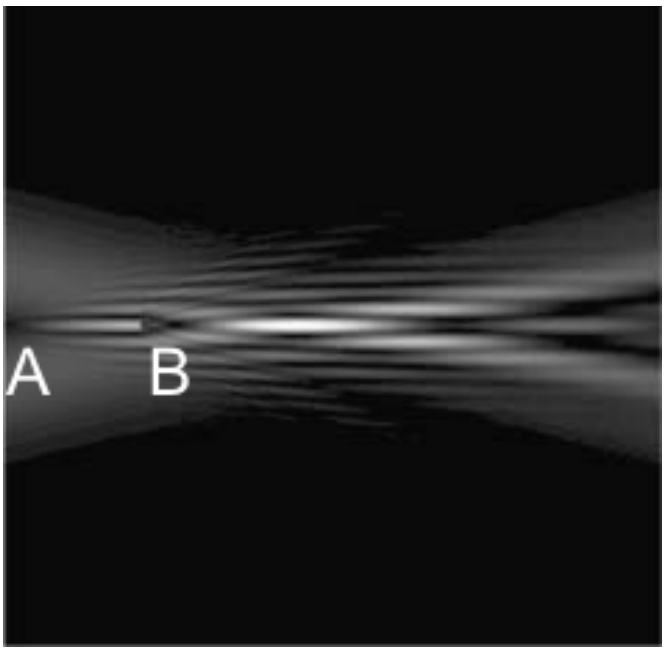

Figure 4.3: Image from a numerical simulation of the reconstruction of a Bessel beam around an object. The Bessel beam is generated by an axicon at A which is included within the simulation. The beam forms before the obstacle, B, and reforms after a discrete distance from the obstruction [55]

deliver simultaneous optical trapping of particles in multiple planes and offers

potential for deeper penetration of light past obstacles into busy media such as cell samples or biological tissues. One last question remains to be answered. How does one generate a Bessel beam? There are now many ways to do so including the use of spatially-modulated light beams but here we will discuss only two of these [47].

4.4 Generation of Bessel beams

Over the past few years, some attention has been given to the process of producing Bessel beams, with the prime aim of improving efficiency and power transfer. The first and simplest techniques to employ, relied on the spatial filtering of a Gaussian beam. Later, more complex methods were developed which generate the beams directly using resonators and nonlinear wave-mixing. Here, the focus will be on the methods using an annular slit and the axicon which has come to replace it as the method of choice.

4.4.1 Annular slit

In 1987 Durnin et al. used a very simple if inefficient method to create their Bessel beams [56]. By adopting the conical wavefront approach as described earlier Durnin was able to create a Bessel beam using an annular slit. As shown in figure 4.4, by placing an annular slit at the back focal plane of a lens this generates its Fourier transform to form the Bessel beam. The properties of

this beam are governed by the dimensions and properties of the lens, slit and input beam. From a geometric approach we find that the open angle, Θ, of the wave-vector cone is given by

$$\tan\Theta = \frac{d}{2f} \tag{4.9}$$

where d is the diameter of the annular slit and f is the focal length of the lens. From this the maximum propagation distance of the Bessel beam can be estimated from

$$Z_{max} = \frac{R}{\tan\Theta} \tag{4.10}$$

Again we can see that the propagation distance of the beam is maximised by increasing the focal length or transverse radius of the lens or by decreasing the diameter of the annular slit. The inefficiencies arise from the fact that a high proportion of the incident light is not transmitted and hence the energy transfer to the Bessel beam is greatly reduced. A much more efficient method is the use of an axicon.

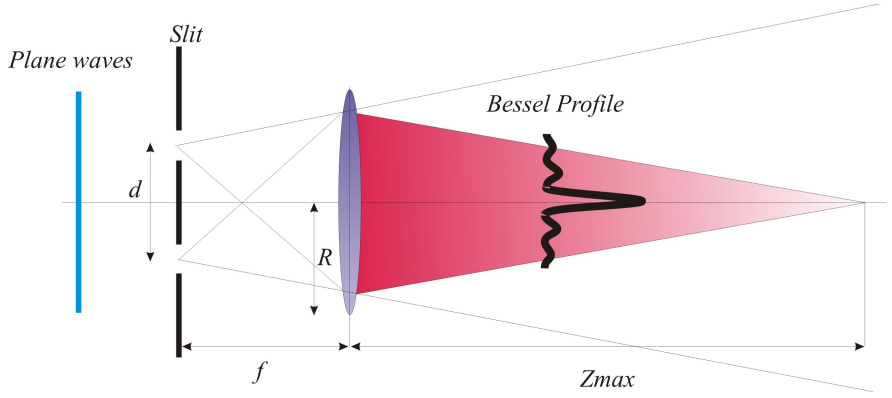

Figure 4.4: A Bessel beam is generated by illuminating an annular slit of diameter d. A lens of radius R is placed at its focal length, f from the slit. The propagation distance is Z_{max}.

4.4.2 Axicon

The axicon is an optical element that images a point source into a line focus [57]. More specifically it has come to mean a lens formed by a plane and a conical surface. Several papers were published in the seventies detailing their properties and uses. Though other methods are sometimes required the axicon is used almost exclusively in laboratories.

Its value became apparent as, in comparison to the annular slit, it could generate Bessel beams with a much higher power transfers [56]. For an axicon with a small angle γ, the opening angle, Θ, of the conical wavefronts is given by

$$\Theta = (n-1)\gamma \tag{4.11}$$

where n is the refractive index of the axicon. Therefore the propagation distance for an axicon-generated Bessel beam can also be written as

$$Z_{max} = \frac{k}{k_r} w_0 \approx \frac{w_0}{\Theta} \tag{4.12}$$

This proves to be a much more efficient method of beam generation. In practice, to produce the longest propagation beam then this relationship tells us that the beam waist of the incident beam should be as large as the axicon diamter. However, the propagation of the Bessel beam is affected by the experimental set-up. With a plane wave, the axicon acts as a hard aperture of diameter R, which through diffraction, produces a periodic variation in the intensity of the central spot along the axis of propagation [55].

This diffraction effect can be negated by using a soft aperture. By placing the axicon at the waist of Gaussian beam which is approximately $w_0 < R/2$ the oscillations in longitudinal intensity do not appear. As follows from equation 4.2 As illustrated in figure 4.5, the Gaussian beam is used to fully illuminate the axicon. As mentioned previously, the Bessel beam is created by the interference of the sets of planar wavefronts emitted from the axicon. It is the interplay of

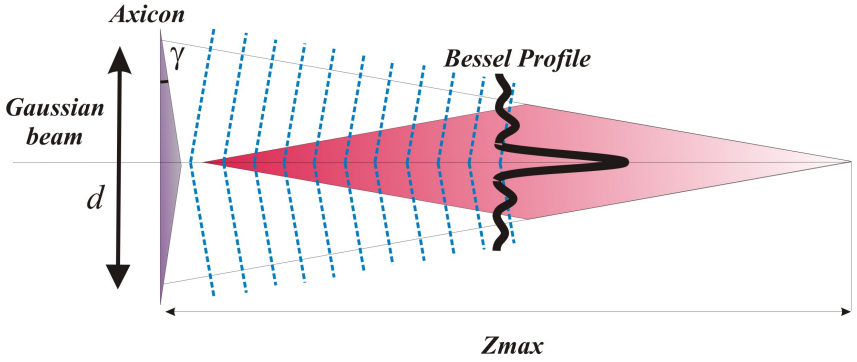

Figure 4.5: A Bessel beam is generated by illuminating an axicon with a Gaussian beam. The planar wavefronts are diffracted and interfere to create the Bessel beam. The maximum propagation distance, z_{max} is dictated by the diameter of the Gaussian beam and the axicon angle, ϕ

the beam and axicon properties which allows a Bessel beam to be tailored for a particular task. Choosing an axicon with a smaller angle γ will increase the number of rings, decrease the radius of the central spot, the width of the rings and increase the propagation distance of the beam. The spot size increases and power density decreases but the reduction in the number of rings brings an increase in the power per ring. Thus the total energy distribution over the beam should remain unchanged.

A Bessel beam can be imaged like any other beam. It can be manipulated using a telescope to either magnify or demagnify the beam to a more useful size. While a x10 telescope will act to increase the centre spot by a factor of 10, the

propagation will increase by a factor of 10^2. This manipulation of Bessel beams has been important in much of the research detailed within this thesis.

It is worth noting that while this research has used zeroth-order Bessel beams some work has been carried out using Laguerre-Gaussian with an axicon to create higher order Bessel beams. These have been particularly useful when manipulating particles of lower refractive index than the surrounding medium. These particles are pushed away from the peaks in the beam intensity profile towards local minima and so guiding is still possible.

4.5 Discussion

Since Bessel beams play such a significant part in the experimental work within this thesis, some consideration has been given in this chapter to its propagation and reconstruction properties. Also important is gaining an understanding of how to generate Bessel beams in the laboratory and so two common methods have been detailed here. The key points to take forward from this chapter are

- Bessel beams are propagation-invariant as its transverse profile does not alter with propagation distance. This property offers extended guiding distances of particles compared to conventional Gaussian beams

- A Bessel beams is self-healing. Its construction from a cone of planar wavefronts mean that the beam will begin to reform around an obstacle.

This lends itself to the simultaneous guiding and trapping of multiple particles and possibilities for deeper penetration into busy media

Now that we have discussed the three main theory elements to this thesis, in the next chapter a brief review of some of the key experiments in this field is given.

CHAPTER 5

Review of optical micromanipulation experiments

My research aim was to investigate the use of ultrashort-pulsed and broadband white-light lasers for multi-photon excitation and optical guiding in Bessel beams. This is just one aspect of what is developing into a wide and varied field of study. This chapter is by no means be a comprehensive review of optical manipulation research but rather, aims to give an flavour into some of the ground-breaking experiments carried out by those who were at the forefront of research in this subject. We will look in detail at the first demonstration of optical levitation by Arthur Ashkin which was published in 1971 as this was the experiment that started the whole phenomenon [58]. Later we will look at an experiment by Malmqvist et al. [59]. which looked at optical trapping experiments using pulsed lasers. To conclude, an early application of optical guiding by Buican is reviewed [60]. First, we shall discuss in brief some of the experiments that have been carried out in this growing field of research.

The experiments we will discuss in detail later in this chapter have led to the creation of an optical toolkit which has become invaluable in the biophysical and medical sciences. Optical micromanipulation techniques have been fun-

damental in expanding our understanding of the physics of even the smallest biological structures [61, 62]. Until the invention of optical trapping techniques, scientists had to be content with investigating bulk tissues to fathom their secrets. Now by using a combination of optical traps, in an optical tweezer configuration, it has enabled studies of interactions at the single molecule level [63].

By being able to measure intramolecular forces as tiny as femtoNewtons, and distances to one-tenth of a nanometre, scientists have been able to gain a better understanding across a range of topics which include biomolecular processes, colloidal dynamics, Brownian motion and even superconductivity [64].

Optical tweezers have been indispensable in the study of molecular motors. These convert chemical energy into mechanical energy and are fundamental in such basic cellular functions as the replication of DNA, RNA transcription and protein synthesis. In a cell, molecular motors are responsible processes such as cell division, endocytosis and vesicle transportation while in bulk tissue, these motors act together to contract muscle tissue. By using optical tweezers it has been possible to carry out key studies in DNA folding and transcription [65]. Perhaps the most powerful implementation of optical tweezers has been as a force transducer measuring femtoNewton forces for these molecular motors [66, 67]. A biological particle can be trapped within an optical tweezer with controlled perturbations applied to affect its motion. From measurements of its motion in response to these perturbations it is possible to gain quantitative information about the intramolecular forces. In 1993, researchers were able to measure the motion of kinesin as it walked along a fixed microtubule track [68]. In this experiment, a single kinesin molecule was attached to a plastic

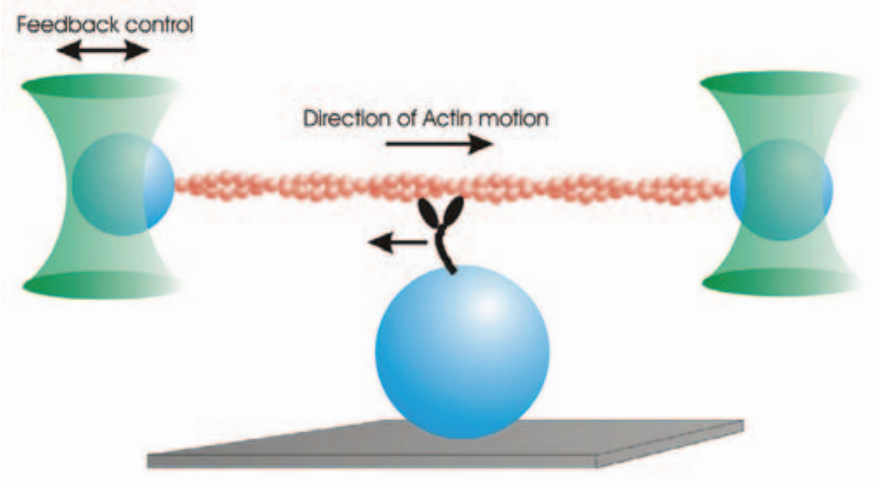

Figure 5.1: Illustration showing an actin filament suspended between two optically trapped microspheres. A third myosin-coated microsphere is brought close to the actin filament. The actin-myosin interactions are measured by the imaging of the trapped microspheres in a four-quadrant detector.[70]

microsphere and held within a low stiffness optical trap. When presented to a fixed microtubule, the kinesin molecule became bound and walked along it in steps that were measured to be $8nm$. A year later, twin optical traps were used to hold a single actin filament which was suspended between two microspheres. As illustrated in figure 5.1, the filament was then placed close to a third fixed microsphere coated in myosin. Movements caused by the actin-myosin interactions could be measured by movements of one of the trapped beads using a four-quadrant photodiode. Similar traps have been used to measure the binding interactions of DNA molecules [69].

In other studies, optical tweezer configurations have been used to study the transfer of angular momentum from light to particle. Both spin and orbital angular momentum were seen to cause rotation of birefringent and absorbing particles in light beams. Off-axis particles within a beam were seen to simultaneously rotate around their own axis and around the beam axis [45].

From the simple optical trap, there has been a flurry of activity in creating multiple arrays by means of spatial light modulators. This allows the simultaneous arrangement and manipulation of multiple particles within an array. The spatial light modulators can be programmed to changed the position of the traps and so controlled construction of 2-dimensional arrays could be possible [71].

Optical tweezers have also been used in microfluidic experiments to remotely control the rotation of tiny pumps and cogs in miniature labs-on-a-chip technology. The aspiration of the mini-labs is to reproduce standard large-scale experiments such as those used in testing for diseases to miniature [72, 73]. This would reduce the cost and turnaround times associated with current methods.

These are just some of the advances that have been made in optical micromanipulation. Now we will review some of the most influential experiments which have the most significance to the work carried out within this thesis.

5.1 Optical levitation using a laser beam

Arthur Ashkin is considered to be one of the pioneers of optical micromanipulation as it was his demonstration of optical levitation of small transparent spheres in a laser beam in 1971 which generated early interest in this field. In quite a simple and elegant experiment, Ashkin used a single vertically directed

focussed cw laser beam to lift a glass sphere upwards from a glass plate.

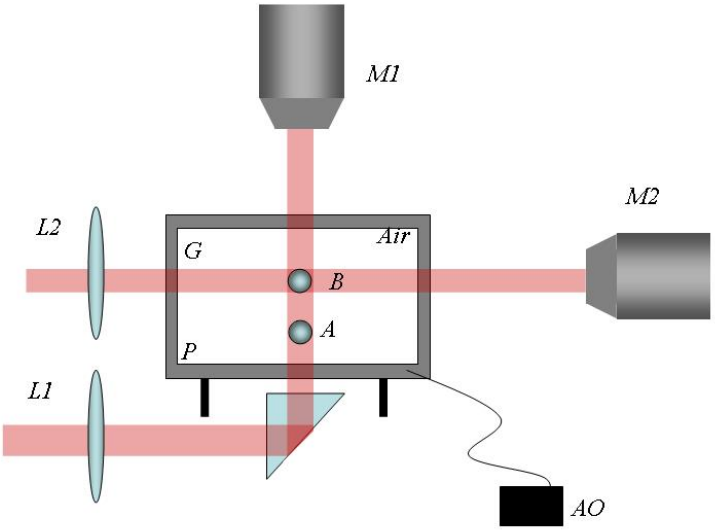

Figure 5.2: Schematic of experimental setup as used by Ashkin to demonstrate optical levitation of a glass microsphere within a vertical cw laser beam. The levitating beam (1) is focussed by a $5mm$ lens, L_1 and directed vertically to sample chamber containing glass microspheres. A particle at rest at point A on plate P is shaken loose by the vibrations provided by the acoustic modulator, AO. A second beam (2) is focussed by a second lens L_2 and directed horizontally into the chamber, G, is used for studies on axial and transverse stability. Microscopes $M1$ and $M2$ are used for imaging the particle displacement relative to each beam.

In figure 5.2 a TEM_{00} laser beam (1) which is the levitating beam with a wavelength of $514.5nm$ and a power ranging from 100 to $500nm$ is focussed by a $50mm$ lens before being directed upwards using a reflecting prism, RP. A sphere of a diameter between 15 and $25\mu m$ is at rest at point A. The arrangement is such that the particle is at rest at the beam waist of the beam which is measured to be $25\mu m$. By knowing the refractive index and size of the particle, Ashkin was able

to calculate the force acting on the particle. To overcome the strong Van der Waals forces of such a small particle, the glass plate is subjected to an acoustic vibration which momentarily shakes the particle loose. Once loose, the particle is guided upwards in the beam to a point of equilibrium. At this point, the radiation pressure and gravity forces balance. By moving the lens the sphere is observed to move around the chamber quite stably within the beam.

Ashkin then gradually reduced the pressure within the chamber to as little as 1 Torr and observed that the particle would drift downwards in the beam. At lower pressures the particles were observed to become unstable within the beam. Two forces are believed to have played a part. The first is a radiometric force which arises from the top of the sphere being hotter than the bottom due to a lensing effect. A thermal force, F_{th} is inversely proportional to the pressure down as far as 10 Torr. Below this pressure, the radiometric, thermal conductivity and viscosity begin to decrease. As the spheres became unstable at these pressures, they were seen to spin and rotate within the beam. Ashkin concluded that the radiometric forces which were dominated by the radiation pressure at atmospheric pressures became more influential at lower pressures.

The next step was to demonstrate his hypothesis that the transverse restoring force was much stronger than the axial force. By using a second horizontal beam with a power of $125mW$ compared to a levitating beam power of $250mW$ the sphere was observed to almost come out of the beam. From this it was deduced that the maximum trapping acceleration for the levitating beam was $1/2g$. This accounts for the high level of transverse stability of the beam. Small variations in the power manifested as pronounced fluctuations in the vertical plane which as expected, the axial restoring force was much less than the transverse restoring

force. These fluctuations were observed by using a microscope, $M2$, as levitating particle could be identified either by its shadow in the the horizontal beam or by the scattering light from the levitating beam. From the arguments used to explain the transverse stability of the particle within the levitating beam, the transverse beam acts to increase the stability of the sphere within the vertical beam. By adjusting the powers of both beams, Ashkin was able to demonstrate quite precise manipulation of the sphere within the two beams. Using the transverse beam he pushed the sphere down towards the waist of the levitating beam where it would become increasingly subjected to the vertical force and break free and without oscillations, return to the equilibrium point. Ashkin notes that this is due to the effects of viscous damping on the particle.

From this work, it was suggested that a third orthogonal beam could further increase the stability of the particle within a confined volume. In fact, this configuration is now used for in atom trapping experiments. This one experiment spawned many others, not least by Ashkin himself who went on to investigate and characterise the phenomenon more fully [11, 12, 39, 40].

5.2 Optical trapping using pulsed lasers

Ashkin's experiment generated considerable interest and spawned many others. Of particular interest, was an experiment carried out by Malmqvist et al in 1995 [59]. In the intervening years, some research had been done using cw lasers to trap microscopic particles of nonlinear crystals such as lithium niobate ($LiNbO_3$). The beam acts as both the trapping beam and the fundamental

for second harmonic generation. However, the power levels of the emitted frequency-doubled radiation was weak as it was limited by the cw laser output power. By using a Q-switched or modelocked laser as the trapping beam, Malmqvist was the first to demonstrate simultaneous optical trapping and second harmonic generation with pulsed lasers. The driver for this research was the potential of using microscopic nonlinear particles as probes in nonintrusive near-field optical microscopy. or fluorescence microscopy.

Figure 5.3 shows the experimental arrangement used by Malmqvist in this work. In the first experiment, a Q-switched $Nd:YAG$ operating at $1.06\mu m$ was used as the trapping beam through a 1.25 NA water immersion microscope objective. By grinding small pieces of KTP and $LiNbO_3$ nonlinear crystal in a mortar small particles were fabricated. Mixing the powders with distilled water a solution of each could be injected into a reservoir below the objective. The particles were trapped just below the focus and any frequency-doubled light generated collected by a second objective and focussed into a fiber. The light was coupled through two filters to a photomultiplier tube (PMT) and lock-in amplifier via a series of filters to reduce the spectral background radiation and block the IR fundamental beam. The collected power was determined from the measured current in conjunction with the manufacturers' data supplied with the PMT and filters. The experiment was repeated using a Ti:sapphire laser and similar suitable filters. Interestingly, the size of each trapped particle was determined by measuring the intensity of scattered light from the trapping beam with an IR camera at perpendicular to the beam. The intensity was compared to the intensity scattered by silica particles of a known size. Assuming Rayleigh scattering and correcting for refractive index, Malmqvist asserted that the diameter of the particle could be measured. For a series of trapped

particles, the emitted power was measured as the power of the fundamental trapping beam was varied. Data points for a series of trapped particles were normalised to that of an $80nm$ diameter particle. The results showed that for a fundamental beam power of $100mW$, the KTP particles gave up to $20pW$ of frequency-doubled light compared to $25pW$ from the $LiNbO_3$. However, there was greater variation in the emitted power between particles. Malmqvist purports the root of this variation to the larger spread in the magnitude of the nonlinear tensor components of $LiNbO_3$ compared to KTP. Malmqvist also investigated the effect of the repetition rate on the emitted power and trap stability. To do this, the average power was maintained and therefore when reducing the repetition rate, the pulse duration is also decreased. The effect therefore is to increase the peak power of the fundamental beam and consequently the power of the frequency-doubled radiation. However, it was observed that at lower repetition rates, the trapping became unstable especially at high trapping powers. The lower repetition rate gives more opportunity for a particle to diffuse out of the trap, and the increased trapping powers generate convection currents and increase the possibility that a trapped particle may be knocked out of the focus by another meandering particle.

To increase the frequency-doubled power the experiments were repeated with a Ti:sapphire laser producing $100 - fs$ pulses at a repetition rate of $76 - MHz$ at $795nm$. This produced peak powers 100 times greater than the Q-switched Nd:YAG laser. However, Malmqvist observed two interesting effects. First though relatively high frequency-doubled light was generated by trapped KTP particles, the $LiNbO_3$ particles were not successfully trapped. Second, Malmqvist noted that there was a degradation of the frequency-doubled light generated by the particles. Increasing the pulse duration went some way to

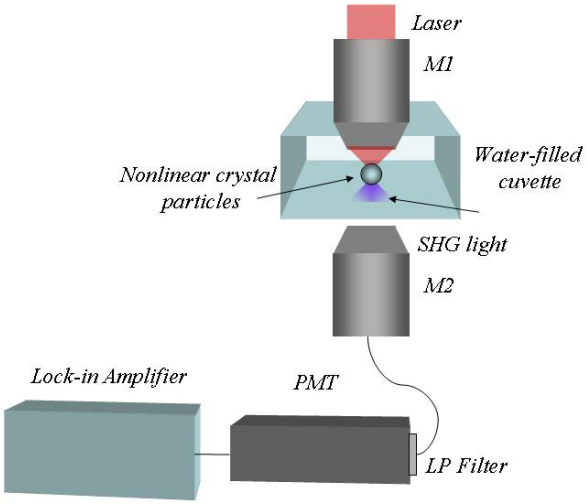

Figure 5.3: Malmqvist experimental arrangement for simultaneous optical trapping and second-harmonic generation. Laser light is coupled into a chamber containing nonlinear particles in water using a high NA objective. A second high NA objective collects any radiation which is coupled to a photomultiplier tube and lock-in amplifier via an optical fiber and series of filters.

reducing this effect. The cause of this was not identified but attributed to some alteration in the nonlinear properties of the material.

Assuming that the trap is a harmonic potential well the Brownian motion of a particle within in the trap leads to a root mean square (rms) displacement $\sqrt{\langle r^2 \rangle}$ from its equilibrium point of

$$\sqrt{\langle r^2 \rangle} = \left(\frac{kT}{k_r} \right)^{1/2} \tag{5.1}$$

where k is Boltzmann's constant and T is the temperature. When pulsed lasers are used for trapping the time between pulses allows for diffusion of the particle

out of the trap. In this case the rms displacement is given as

$$\sqrt{\langle r^2 \rangle} = \left(\frac{kT}{3\pi a \eta} \right)^{1/2} \tag{5.2}$$

where a is the particle radius, η is the viscosity and T is the time between pulses.

Theoretically the frequency-doubled power was determined using the assumption that the trapped particle is a sphere. The nonlinear polarisation was calculated as $\mathbf{P}(2\omega) = 2\epsilon_0 \mathbf{d} \mathbf{E}_1^2$ where ϵ_0 is the vacuum permittivity, $\mathbf{d}$ is the nonlinear susceptibility tensor and $\mathbf{E}_1$ are the electric-field components at the fundamental frequency inside the particle assumed to be

$$E_1 = \frac{3\epsilon_2}{\epsilon_1 + 2\epsilon_2} E_2 \tag{5.3}$$

where E_2 is the fundamental electric field due to the trapping beam in the water only, and ϵ_1 and ϵ_2 are linear permattivities of the particle and water respectively [17]. Due to the small size of the particle ($75nm$) it was treated as a dipole source at the second-harmonic frequency with a dipole moment of $(4/3)\pi a^3 P_i(2\omega)$ where $P_i(2\omega)$ are the elements of the nonlinear polarisation $(i = x, y, z)$. The total emitted power,W_{total} from a dipole is given as

$$W_{total} = \frac{64\pi^5 c a^6}{27\epsilon_0 n_2^3 \lambda^4} \sum \left[P_i(2\omega) \right]^2 \tag{5.4}$$

From this Malmqvist was able compare the theoretical second-harmonic powers with his experimental results. As show in figures 5.4 and 5.5, taken from the Malmqvist paper, there was good agreement between the two [59].

Furthermore, the gradient of the curves on a logarithmic scale indicate that

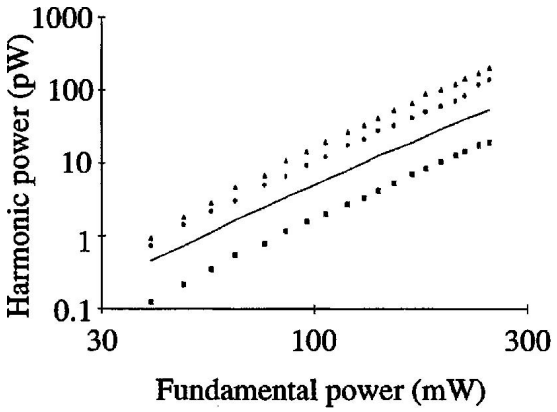

Figure 5.4: Plot showing the power of second-harmonic generated radiation from optically trapped nonlinear particles in a nanosecond Q-switched laser at $1.06\mu m$ as a function of power. [59]

there is quadratic dependence between incident power and that of the second-harmonic generation powers.

5.3 Optical guiding in biology

In the previous sections we discussed the first optical trapping experiments using cw and pulsed laser sources. Here an experiment with real applications in the field of biology is reviewed. The ability to manipulate and select single cells is highly desirable in experimental cell biology and immunology as well as in other areas of biomedical research. Two techniques have become widely used for the purposes of cell separation or positioning. Flow sorting is a fast automated process used to sort cells within a volume of fluid based on their optical or electrical properties. In this method, positional accuracy is sacrificed for high speed, density and volume. In contrast, optical micromanipulation offers cell positioning to within a micron.

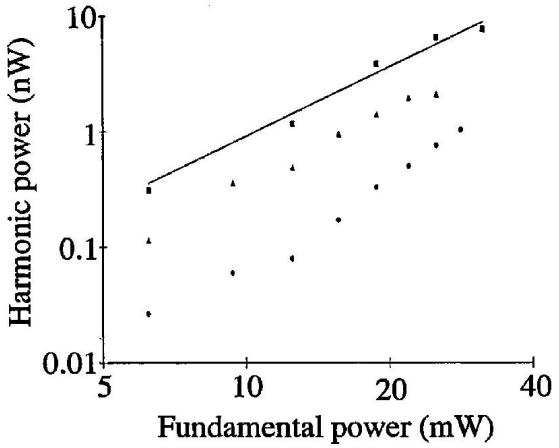

Figure 5.5: Plot showing the power of second-harmonic generated radiation from optically trapped nonlinear particles in a $100fs$, $76MHz$, $800nm$ laser as a function of power [59]

One of the earliest experiments in cell manipulation was carried out by Buican et al in 1987 [60]. This experiment set out to develop a simple instrument to first position and then transport single cells a few millimetres where they could be automatically sorted based on their optical properties. In the first part of the experiment, a simple optical trap as was used to manipulate a mixture of cells, microorganisms and polystyrene microspheres in solution. Having successfully trapped these particles, the apparatus was adapted to allow the introduction of cells at a defined location within the chamber. This was done by using two orthogonal beams from an Argon-ion laser ($\lambda = 488nm$), one to propel the particles and a second to deflect as illustrated in figure 5.6. The particle suspension was injected at a low speed into the propulsion beam where they are trapped and guided along the axis. A probe beam from a He-Ne laser ($\lambda = 633nm$) also intersects the propulsion beam orthogonally (A short-pass filter blocks it from the propulsion beam). The intensity of scattered light is measured perpendicularly to the probe beam. The deflection beam, based on this measured value can be automatically switched momentarily to a higher intensity thereby deflecting the particle into one channel. If no signal

is detected, the particle is able to continue along the axis of the propulsion beam into a second channel. A limitation to the technique is that it relies on

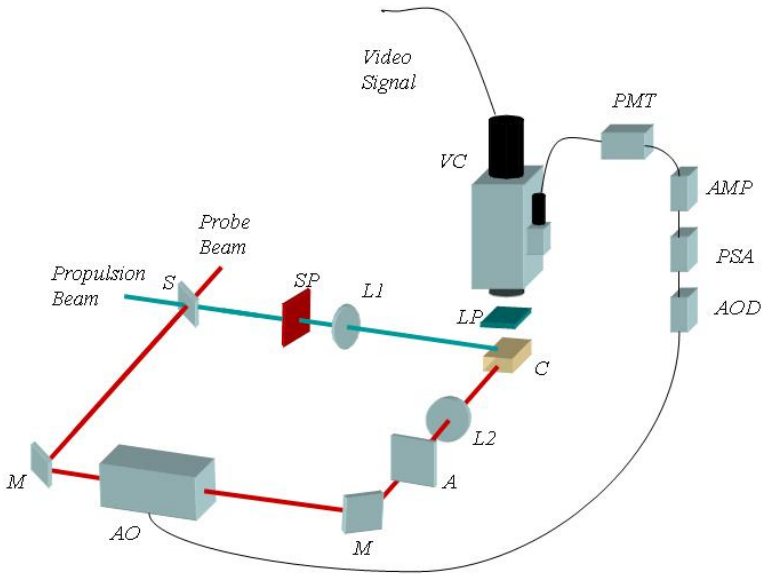

Figure 5.6: In the setup used by Buican, the output from an Argon ion laser is split by splitter S into two orthogonal beams to form a propulsion and a deflection beam. The probe and deflection beams travel together through a series of mirrors , M, an acouto-optic modulator, AO, an aperture A and focussing lens L_2 into the chamber C. The propulsion beam travels through a short pass filter, SP,and a focussing lens L_1 into the chamber. Scattered light from the particles passes through a long pass filter LP is collected by a high NA microscope objective and coupled to a camera and an optical fiber OF. The photomultiplier tube PMT measures the signal strength. This signal is amplified, AMP and analysed, PSA, and coupled to the acoustic optic modulator where it controls the deflection beam.

the detection of the scattered signal at $90°$ to the deflection beam. For this reason enhancements would be required to the signal detection components to produce a more robust and automated selection instrument. Developments in research since 1987 have resulted in such instruments.

However, the experiment demonstrated that optical based selection of single biological cells was possible. Other interesting findings from the experiment include the observation that when several polystyrene microspheres are present int the propulsion beam, the particles coming from behind catch up with the ones ahead and form clumps or agglomerations. Buican proposes that this is due to the fact that the trailing spheres scatter some of the beam away from the beam axis behind the leading ones. This causes a decrease in the propulsion beam force and consequently the particle velocity. However, the same phenomenon does not occur with CHO cells. Here it was observed that the cell separation decreased to a minimum value but was maintained and the cells continued with equal velocities.

5.4 Discussion

In this chapter we have reviewed in brief some of the key experiments to date in optical trapping and guiding. In particular, we looked at some of the applications to studies in biomolecular physics. We then looked in detail at some of the key experiments which are relevant to the research contained within this thesis. These experiments include optical levitation of a particle within a beam, two-photon excitation in optical trapping and the optical guiding of cells. From this review, the focus moves towards a detailed discussion of the experimental work. This will be the subjects of the next three chapters.

CHAPTER 6

Experiments in optical guiding with pulsed lasers

In this first experimental chapter we bring together the theory and background of ultrashort pulses, multi-photon excitation and Bessel beams from the previous chapters. In this chapter we will discuss experiments using ultrashort-pulsed and cw lasers to compare Bessel and Gaussian beam guiding. We will also begin to combine these optical guiding techniques with multi-photon excitation.

Prior to this work, most if not all guiding experiments were carried out using continuous wave lasers. This work was undertaken to investigate whether particle guiding was determined by the *average* or the *peak* power of the laser. In effect would a particle be guided more quickly by a repeated but short, intense momentum kick than by a gentle continuous force? If the optical guiding was influenced by the high-peak powers we would expect to see greater guiding velocities. Second, if there was any enhancement would it be present in both Gaussian and Bessel beams? We shall now go on to discuss the experiments which aim to answer these questions.

6.1 Optical guiding with a ultrashort-pulsed and cw lasers

Successful guiding experiments had already been carried out by members of the group using cw lasers and the aim here was to carry out the first set of guiding experiments using an ultrashort-pulsed laser. Some members of the Ultrafast Photonics Group had recently developed a compact and low-cost femtosecond Chromium-doped:Lithium Strontium Aluminium Fluorite(Cr:LiSAF) solid-state laser [7]. The laser had modest output powers of approximately compared to other sources in the department, however, based on other experiments carried out by the Optical Trapping Group it was anticipated that the output powers could be sufficient [74]. However, for reasons that will be become clear, the Cr:LiSAF was not a suitable source for guiding experiments which explore multi-photon excitation and optical guiding in Bessel beams. The Cr:LiSAF laser could give up to $40mW$ of pulsed radiation at between 750 and $850nm$. It soon became apparent however that the experiments would require significantly higher output powers and consequently I moved to using two Ti:sapphire lasers each with different output characteristics. The first could provide average output powers of up to $1.2W$ and a pulse duration of approximately $100fs$ at a wavelength of $800nm$. The second was able to provide pulses as short as $12fs$ with an average power of approximately $500mW$ at $800nm$

6.2 Optical guiding with a Chromium-doped:LiSAF laser

The laser, which is illustrated by figure 6.1, consists of a $3mm$ Brewster-angled Cr:LiSAF crystal pumped by two pairs of AlGaInP laser diodes operating in the visible red with their wavelengths, $660nm$ and $685nm$, aligned with the absorption maxima of the gain medium. The combined outputs totaling $100mW$ from the laser diode pairs, D1 to D4, are coupled using a system of polarising beam splitters and filters, into the cavity through a specially-coated mirror, M3. This mirror is coated to transmit the pump beam but reflect the intracavity beam. As shown in figure 6.2, the emission spectrum of the Cr:LiSAF extends from $700nm$ to $1\mu m$ with a peak at around $850nm$. The compact nature, low-cost operation and infrared output makes the Cr:LiSAF laser a possible alternative to the more costly and bulky Ti:sapphire lasers. After arranging the diodes so

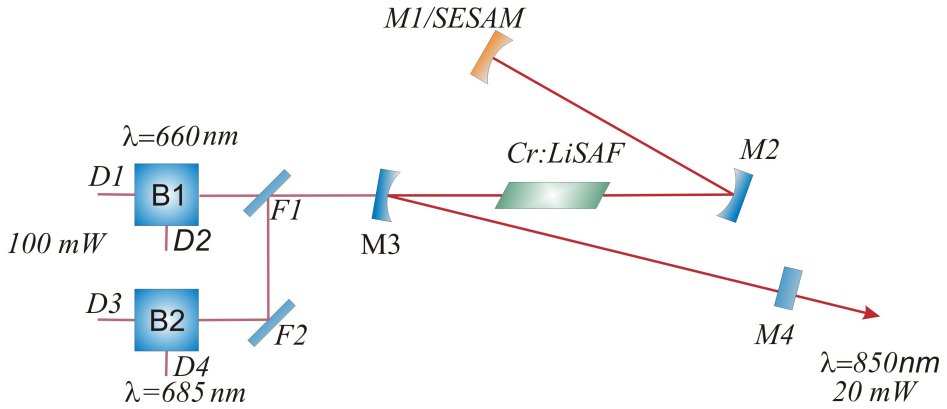

Figure 6.1: Schematic of a Cr:LiSAF laser cavity. Two pairs of laser diodes, D1 through D4 with wavelength $\lambda = 660nm$ and $685nm$ are coupled using a series of dichroic mirrors F1, F2 and beamsplitters B1, B2, into the cavity via mirror M3. This beam is used to pump to a Brewster-angled Cr:LiSAF crystal. The cavity comprises of four mirrors M1, M2, M3 and M4 which have high-reflection (HR) coatings to minimise loss within the cavity. The mirror M1 is replaced by a Semiconductor Saturable Absorber Mirror (SESAM) to permit self-modelocking

that their spots overlap in the far distance, I placed the highly reflective mirrors

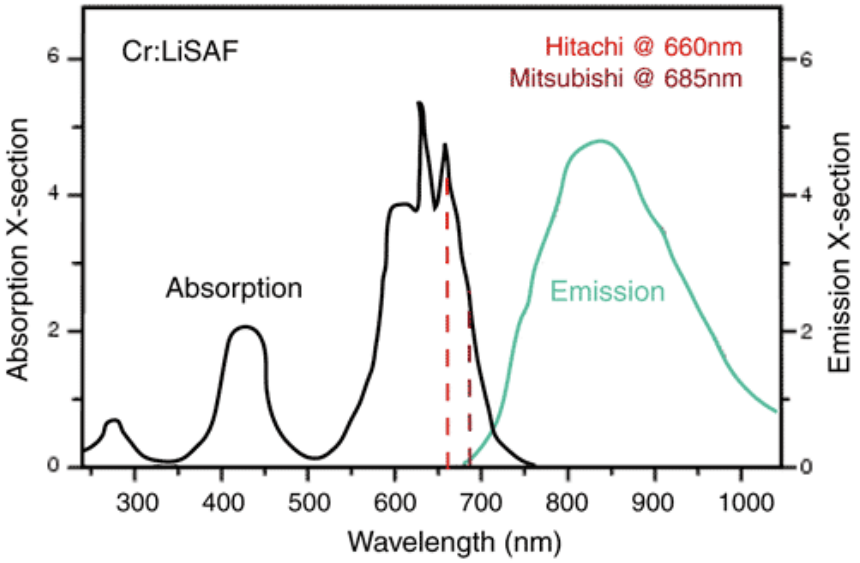

Figure 6.2: The absorption and emission spectra of the Cr:LiSAF laser with maxima in the red and infrared regions of the electromagnetic spectrum. This is amenable to excitation with diode lasers emitting at $660nm$ and $685nm$

M1 through to M4 according to the calculations made using ELCAV software. This software allows the design and optimisation of a laser cavity. Once in place, I used a low-range power meter to measure the signal from between mirrors M3 and M4 while slowly adjusting the alignment of mirrors M1 and the crystal. Once aligned correctly, the back fluorescence from the crystal showed as a sharp increase in the measured signal. Mirror M4, was initially 99.5% high reflector, but was replaced with a 1.5% output coupler. Once cw lasing was achieved, I swapped out mirrors M2 and M3 for dispersion compensating mirrors. Finally, mirror M1 is replaced with a semiconductor saturable absorber mirror (SESAM) which facilitates the self-modelocking process within the cavity. By using a SESAM to modelock the laser the output was approximately $20mW$ of average output power. However, after rebuilding the cavity together, Ben Agate and I were able to achieve up to $40mW$ of average output power.

To determine the pulse duration of the output pulses, I carried out an autocorrelation measurement. This relies on a method akin to a Michelson interferometer. In this case, the interference fringes reveal properties of the duration of the pulse as well as its shape. From the trace, the fringe separation and full width half maximum were measured and a pulse duration of $100fs$ at a central wavelength of $846nm$ was calculated. Using a spectrum analyser I measured the bandwidth of the output pulses to have a FWHM of approximately $6nm$.

This laser was set up for Gaussian and Bessel beam guiding experiments as shown in figure 6.3. The original laser was improved by upgrading the SESAM to give higher intracavity and output powers. With approximately $40mW$ of output power, it was hoped that Bessel beam guiding could be achieved and characterised. Once aligned, the output was collimated and measured. This was necessary to allow us to determine what extra-cavity apparatus would be needed to give the a Bessel beam with the desired properties. Using BeamMaster apparatus and software, the transverse profile of the beam was analysed to have a FWHM diameter of approximately $6mm$. For efficient Bessel beam generation it is important to fully illuminate the axicon. Two AR-coated lenses of focal length 50 and $300mm$ are used to make a $1:6$ telescope which expanded the beam to approximately $25mm$ which is the diameter of the axicon. A 1° axicon was used to generate a Bessel beam whose transverse profile was imaged using a x10 microscope objective coupled to a CCD camera which had a response in the infrared region of the spectrum. An image of the transverse profile of this beam is shown in figure 6.4. The central spot size was measured as approximately $57\mu m$. The propagation distance of this Bessel beam was found to be in excess of a metre. For effective guiding, the Bessel beam must be of the order of the particles to be guided. Here, a spot size of less than $6\mu m$

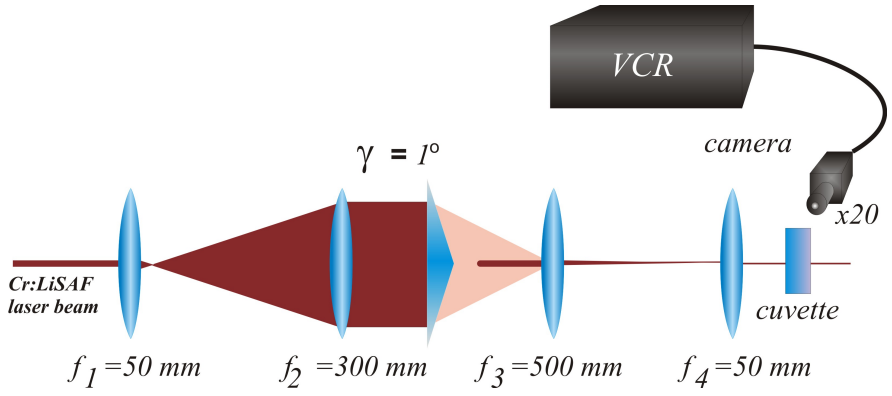

Figure 6.3: The experimental apparatus for guiding with a Cr:LiSAF laser shows the beam from the Cr:LiSAF laser is expanded using AR-coated lenses f_1 and f_2a 1:6 telescope to fully illuminate the 1 degree axicon. The Bessel beam is then demagnified using AR-coated lenses f_1 and f_2 to give a 10:1 demagnifying telescope. The Bessel beam propagates through a glass cuvette containing the particles in solution. A high NA x20 microscope objective is coupled to a CCD which is used to record images of the guided particles

was required, therefore using two AR-coated lenses with focal lengths 500 and $50mm$ respectively, a $10:1$ demagnifying telescope was required. Analysis of the beam after the telescope gave a central spot size of approximately $6\mu m$ and a propagation distance of between 2 to $3mm$. For guiding, the particles need to be in solution as this provides buoyancy which helps to overcome the force of gravity. Therefore a tiny container in the form of a cuvette was needed. These open-topped chambers are made from optical quality glass and in a variety of sizes. To fully enclose the Bessel beam, I selected a cuvette measuring $3mm \times 3mm \times 10mm$ (length $\times$width $\times$ height). A water-based solution of 3 μm spheres was placed using a pipette into the cuvette which was mounted in a holder on an XYZ-translation stage. On advice, a little heavy water was added to suppress heating effects. The absorption spectra of heavy and normal water have not been subjected to much investigation across the entire visible and infrared spectrum but from figure 6.5, it can be seen that heavy water (D_2O) has a different absorption spectrum to the distilled H_2O. In the red to infrared

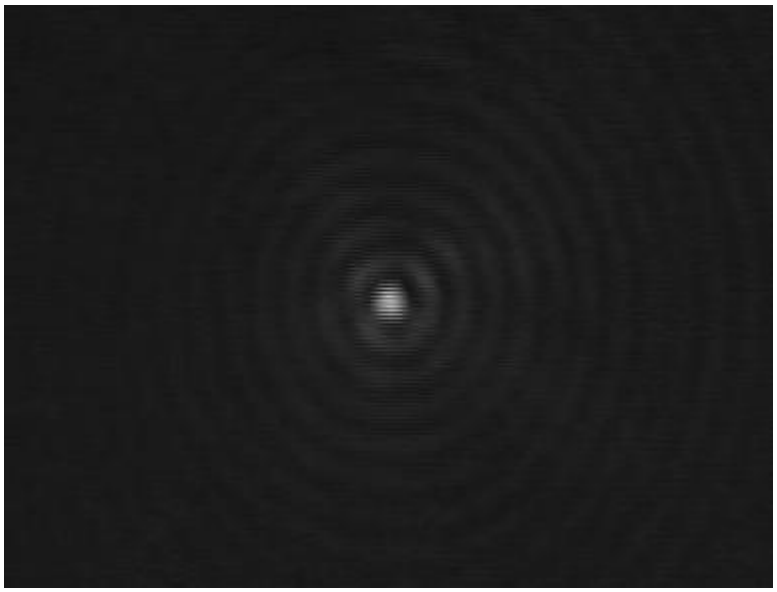

Figure 6.4: Image of Bessel beam as generated by a Cr:LiSAF laser incident on a 1° axicon. The central spot size is measured to be approximately 57 microns.

region the absorption of heavy water is much less than that of normal water [75]. By using one part heavy water to ten parts of normal water, the convection which results from high absorption are suppressed enough to provide the an environment suitable for optical guiding. In contrast, adding too much heavy water would suppress the convection currents to such an extent that very few particles would be loaded into the guiding beam. The microscope objective and camera were oriented to capture images of particles as the would be guided along the beam axis. As the camera was coupled to a monitor, it was possible to move the cuvette relative to the Bessel beam. Some time was spent trying to see particles being guided within the beam. After no success, the experiment was repeated but with a simple Gaussian beam with a spot size of approximately $5\mu m$. Some limited evidence of guiding within the beam was observed.

A comparison of Bessel beam and Gaussian beam guiding could not be carried

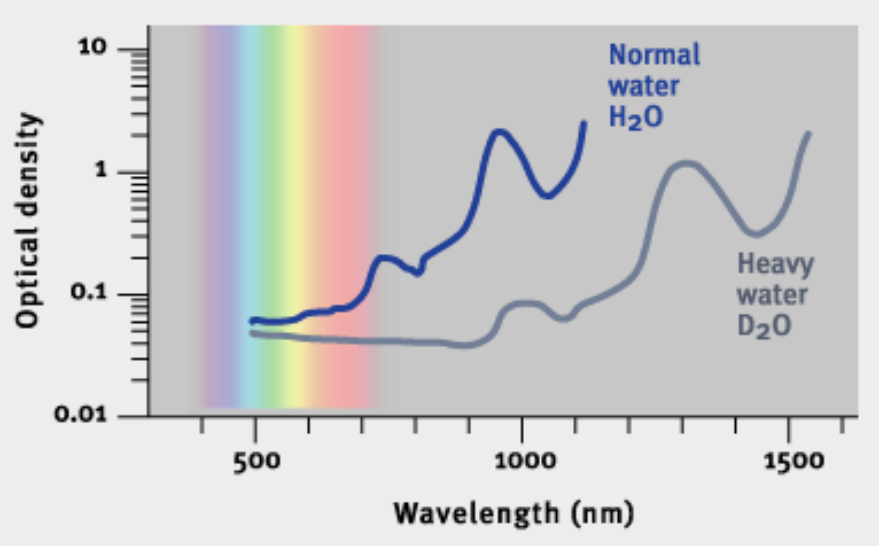

Figure 6.5: The absorption spectra of heavy and normal water show that in the region of the infrared and visible spectrum, heavy water has much less absorption than that of normal water [20]

out using this laser as it was concluded that the power contained within the central spot and each ring was approximately $2mW$ which simply too low to enable guiding. A calculation using the relationships as detailed in Chapter 2 show that for this laser the power density contained within the central spot is approximately $4.15 \times 10^8 W/cm^2$. In comparison, a Gaussian beam with the same spot size had a power density of approximately $1.70 \times 10^{10} W/cm^2$. Since guiding was achieved with a Gaussian beam from this laser, the requirement was to find a source that had comparable or better power densities within the Bessel beam.

It may have been possible to compare cw and femtosecond guiding with this source, however, the extended guiding distances offered by Bessel beams remained attractive as this would permit more accurate measurements of the guiding distances and velocities. For this reason, the apparatus was re-

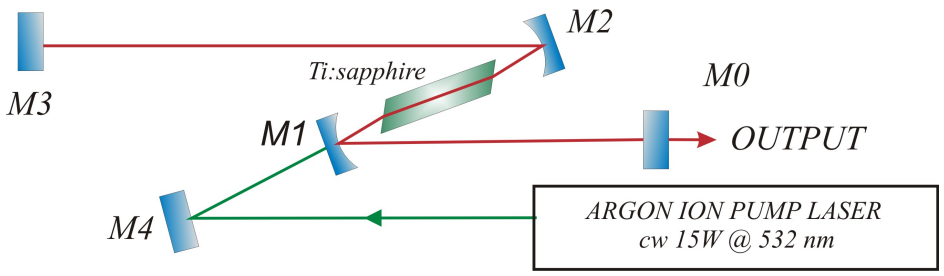

Figure 6.6: Schematic diagram of the Spectra-Physics 3900 Ti:sapphire laser. The laser cavity comprises high reflectivity mirrors M0 to M3 with Brewster-cut Ti:sapphire crystal and an argon-ion pump beam coupled into cavity via mirror M4

assembled for use with a far more powerful Ti:sapphire laser. These experiments will be described in the following section.

6.3 Optical guiding with a 110 fs Ti:sapphire laser

The majority of my research was carried out using a modified Spectra-Physics Model 3900 laser which is illustrated in figure 6.6. The main laser cavity consists of a system of mirrors M0 to M3 with a Brewster-angled Ti:sapphire crystal placed at between two spherical mirrors M1 and M2. The pump laser was a Spectra-Physics Model 2030 argon-ion laser with an output of up to $20W$ in a TEM_{00} mode. The pump beam first passes through a periscope arrangement to rotate the polarisation by $90°$ before being coupled into the cavity by mirror M4. Figure 6.7 show the modifications made to the laser cavity. First, a set of SP14 glass prisms are introduced into the arm between mirrors M2 and M3. This double-prism pair provides intracavity dispersion compensation which as described in chapter 2is vital for achieving ultrashort pulses. With a pump power of $20W$ it was possible to produce a cw output of

up to $2W$. The second modification was replacing the birefringent filter with a

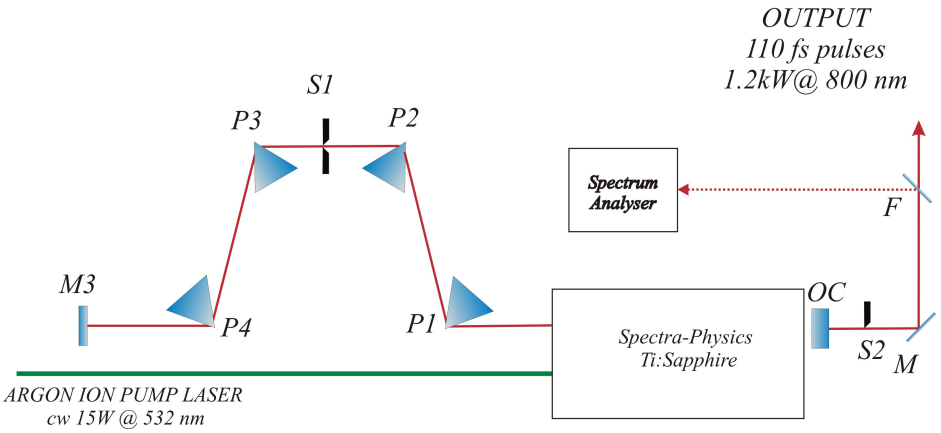

Figure 6.7: Schematic diagram of the Spectra-Physics 3900 Ti:sapphire laser with additional prisms P1 to P4 providing intracavity dispersion compensation and variable-aperture slits S1 and S2 to facilitate pulsed operation.

variable-aperture slit, S1, between prisms P2 and P3. This slit is used to tune the range of wavelengths that can propagate through the cavity but reduced the output power to a maximum of $1.2W$. The slit, S2, before the output coupler is a second variable-aperture slit and acts as a hard aperture which can encourage the modelocking process.

As one of the earliest solid-state lasers, this Ti:sapphire laser, in its modified state, is not a simple turn-key laser. The argon-ion pump laser requires a three-phase power supply and, like the Ti:sapphire laser itself, continuous water-cooling. The self-modelocking process required introducing a transient intense spike into the cavity. This in theory is done by simply tapping either end cavity mirrors. In practice, the cavity had to be aligned carefully to optimise the cw output which was measured using a high-range power meter. The laser would not modelock if the cw output power was less than $1W$. By carefully walking the end mirrors of the cavity, I was able to increase the power. If that alone was not effective in raising the output power, I had to carefully clean

the intracavity optics which were prone to becoming dusty. Occasionally, this would misalign the laser and I would have to go through the lengthy process of realigning the cavity using a pinhole and low-range power meter until it started lasing once more.

Once I had a sufficiently high cw output, I was then able to modelock the laser. To enable this I used a partially reflecting mirror to couple a tiny amount of the output beam into a spectrum analyser which was connected to an oscilloscope. While I quickly moved the end mirror M4 back and forth and tweaked mirror M3, I was able to watch for spectral output of the beam to transform from a narrow line profile to the broader bandwidth profile which is characteristic of a pulsed laser. If required, I was able to tune the central wavelength using the variable-aperture slit, S1. Modelocking was terminated simply by temporarily obstructing the intracavity beam.

The output of the laser was characterised spectrally by measuring the profiles on the oscilloscope from the spectrum analyser. Using an autocorrelator, I was able to measure the temporal properties of the pulses by means of the interferometric and intensity methods. In the interferometric method, the profile should be symmetrical with the height of the peak a factor of eight greater than the trough. The pulse duration is derived by measuring the separation between fringes within the pulse envelope. In the intensity method, the full width half maximum gives the pulse duration. A trace obtained using the interference autocorrelation method is shown in figure 6.8. While the pulse duration can be measured from the intensity method, more information about the temporal shape of the pulses can be gleaned from the profile obtained by the interferometric method. This laser was the first to demonstrate Kerr lens

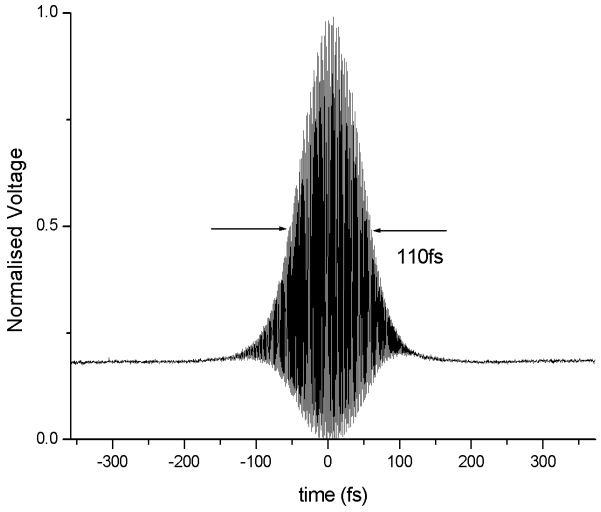

Figure 6.8: Interferometric autocorrelations of pulses from a Ti:sapphire laser. The interferometric autocorrelation shows that the pulses are not chirped and the pulse duration is $110fs$

modelocking by Spence et al. in 1990 [76]. I used this laser to carry out my first experiments in optical guiding. Since this experiment in 1990, smaller self-modelocking ultrashort pulse lasers have been developed which produce even shorter pulses including the Femtosource Ti:sapphire laser which I also used in my research. A description of this laser now follows.

In this work the laser of choice was the modified Spectra-Physics laser which is also described in detail in Chapter 2. As per the previous experiment, it was important to characterise the output from the laser to enable me to configure the apparatus for effective guiding. Using the same calculations as earlier, the power density for a Bessel beam with 40 rings and centre spot with a diameter of 5 μm was estimated at $1.1 \times 10^{11} W/cm^2$.

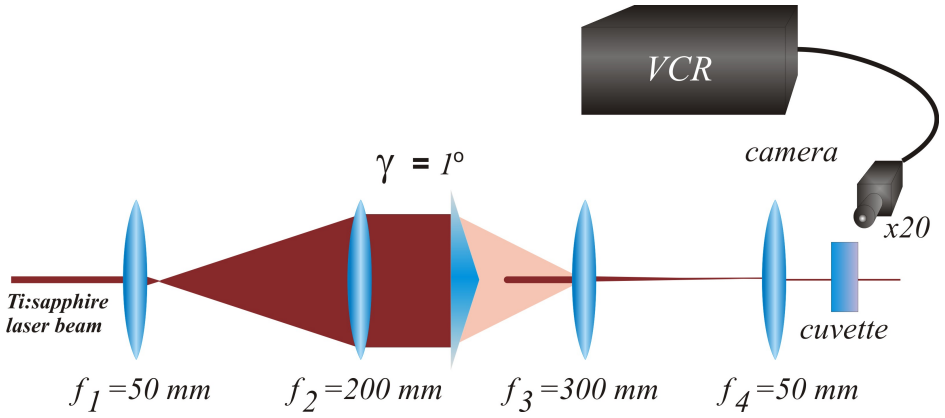

Figure 6.9: Schematic of experimental apparatus used to optically guide particles within a Bessel beam using a pulsed/cw Ti:sapphire laser source providing pulses with a duration of $110fs$. The first two lenses with $f1 = 50mm$ and $f2 = 200mm$ act as a 1:4 magnifying telescope. The axicon produces a Bessel beam which is then demagnified by the lenses $f3 = 300mm$ and $f4 = 50mm$ to produce a Bessel beam with a central spot diameter of approximately $5\mu m$ and propagation distance of approximately $3mm$. The images by are captured by a CCD camera via a microscope objective with a magnification of x20 and numerical aperture of 0.75

As depicted in figure 6.9 the laser source was a Ti:Sapphire laser pumped by a Spectra Physics 2040 argon-ion laser which provided up to $1.2W$ of output power that could be tuned between $790nm$ and $850nm$. The pulse duration was measured using an intensity autocorrelation. After several measurements, the pulse duration was found to be $110fs$ at the centre wavelength of $800nm$. Using oscilloscope measurements, the bandwidth was determined as $9nm$. Assuming the profile to be that of a $sech^2$ pulse implied that the duration-bandwidth product was 0.46. The repetition frequency between pulses in modelocked operation was $80MHz$. The Ti:Sapphire laser could be easily switched between modelocked and cw operation simply by introducing a transient obstruction within the intracavity beam. This change of operation mode effected changes in the beam properties that were not at first fully understood nor quantified. It was recognised that there may be alterations to the beam profile, significant or otherwise, that would preclude a fair comparison being drawn between

the two sets of results. Therefore, the beam profiles were measured using a BeamMaster, with the change in spot size between the two modes measured to be less than 3%.

The TEM_{00} laser output was passed through a $1:4$ telescope arrangement to fully illuminate the 1 degree axicon used to generate the Bessel beam. With careful alignment of the preceding optics, this produced a Bessel beam with a central beam diameter of $30\mu m$. This was measured by analysing still images from video footage of the experiment using LabView IMAQ software. A calibration of the images was possible by measuring the imaging distances and camera pixel dimensions. By the same method, the beam was analysed and found to have a diffraction-free propagation distance of over $25cm$. For the purpose of this experiment, a shorter guiding distance, and smaller core size was needed and this was achieved by placing a $6:1$ demagnifying telescope arrangement after the axicon. Consideration was given to the effect of the axicon on the pulse duration and bandwidth. An autocorrelation measurement taken after the axicon showed that the pulse broadened from $95fs$ to $130fs$ while the full width half maximum (FWHM) bandwidth remained effectively unchanged at $9nm$. Before any guiding experiments were carried out, I wanted to know whether the Bessel beam would change when generated by the femtosecond beam compared to the cw beam. I imaged the transverse cross-section of the Bessel beam at intervals along the beam axis for both. I measured the diameter of central spot cross-section in eight directions and determined the average diameter. A plot of this data as shown in figure 6.10 shows that there is no discernible difference between the two modes of laser operation. The demagnified Bessel beam was passed through a small glass cuvette with dimensions of $3mm \times 3mm \times 10cm$ (length x width x height). By this stage of the experiment,

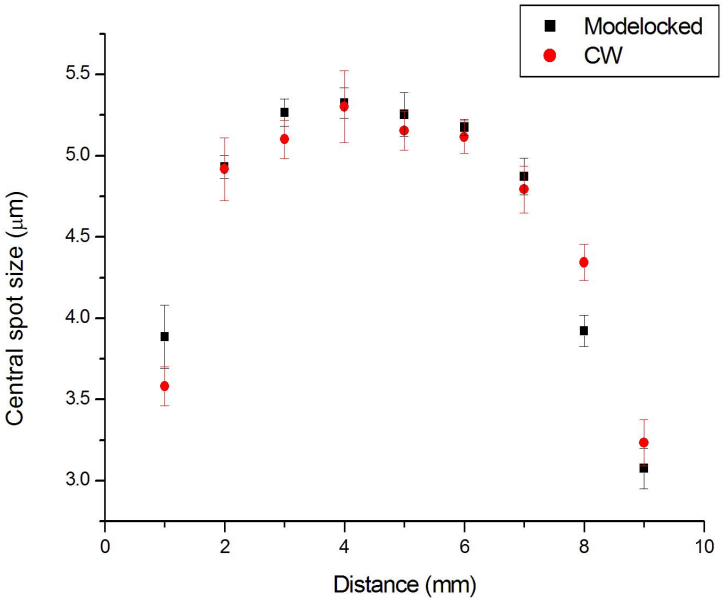

Figure 6.10: Plot shows how the central spot diameter varies the along beam axis of Bessel beam when generated by a $110fs$ modelocked and cw Ti:sapphire laser

heating effects had been observed within the cuvette and so heavy water was added to help reduce the water absorption at this infrared part of the spectrum. Using a pipette, a $120\mu l$ measure of micron sized polymer spheres in a $10:1$ mixture of H_2O and D_2O was deposited into the cuvette. A x20 microscope objective and CCD camera were again oriented to view the side of the cuvette parallel to the beam axis. After viewing on the monitor that particles were being successfully guided within the beam, video footage of the guided particles was recorded and analysed using IMAQ software to measure the guiding velocity of the particles.

Particle velocity was determined by taking frames from the video footage and measuring the distance travelled by each particle between frames. With a known video capture rate of 25 frames per second and the IMAQ software

calibrated, it was possible to directly calculated the velocity of each particle as it traversed the cuvette. The particle guiding velocity was measured for a variety of particle sizes and at a range of powers.

Initial data taken for a variety of particle sizes showed that the guiding velocities were comparable for pulsed and cw guiding. As figure. 6.11 below shows, the particle velocities were greatest for the $2.3\mu m$ particles. Given that the $2.3\mu m$

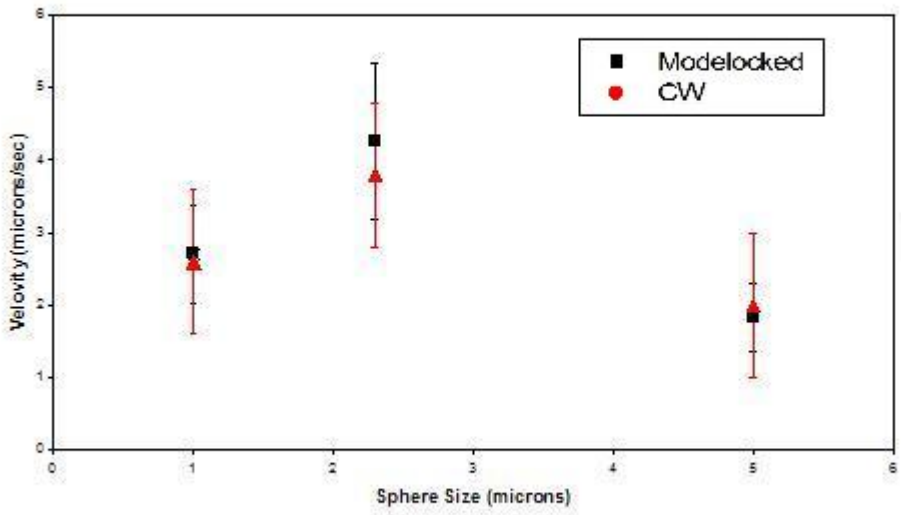

Figure 6.11: Plot shows the averaged guiding velocities of 15-20 particles in a femtosecond and cw Ti:sapphire laser beam with centre wavelengths of 800nm for three different particle diameters: $1\mu m, 2.3\mu m$ and $5\mu m$

particles had higher guiding velocities, these were used in a further experiment in which guiding velocities were measured with laser power for both cw and pulsed operation of the guiding laser. This was done by measuring the velocity of the particles as they traversed a single screen shot. While it would have

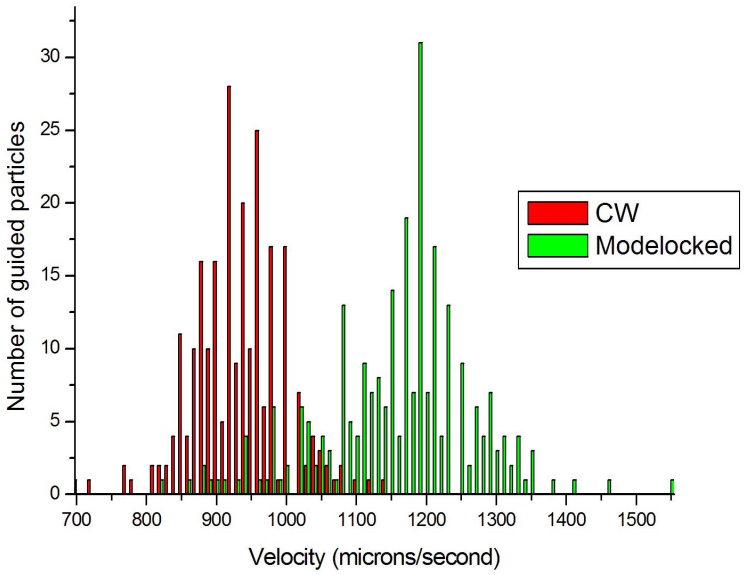

Figure 6.12: Plot shows the distribution of particle velocities for guiding of $2.3\mu m$ polymer spheres in a femtosecond beam compared to a cw Ti:sapphire beam with an output power of $800mW$

been desirable to measure the velocity over a longer distance, this would have introduced other uncertainties as the XYZ-translation stage would have to be translated. By using a microscope objective with a higher magnification power, it would have been possible to measure the particle velocities over a longer distance. I tried this, however the working distance of the x40 microscope objective was $2.1mm$ compared to $6.1mm$ for the x20 objective and this proved to be too short to allow imaging of the particles within the cuvette. The average output of the beam was measured at $800mW$. As shown in figure 6.12 the particles within the modelocked beam have a higher guiding velocity compared to those guided in the cw beam. This was an exciting result. As good experimental practice dictates, the experiment was repeated. In this instance, analysis showed that there was no discernible difference in the guiding velocities. As the experimental results were not able to be consistently repeated, I investigated any possible

reasons for the inconsistency in the results. The first observation was that some of the spheres used within the experiment were doped with a blue fluorophore. A comparison using these spheres is shown in figure 6.14 where it can be seen that the particle have a higher velocity when guided in the modelocked beam. Given the high peak powers of the pulsed beam it was possible that this affected the fluorescing polymer spheres in some way. Furthermore, it became notice-

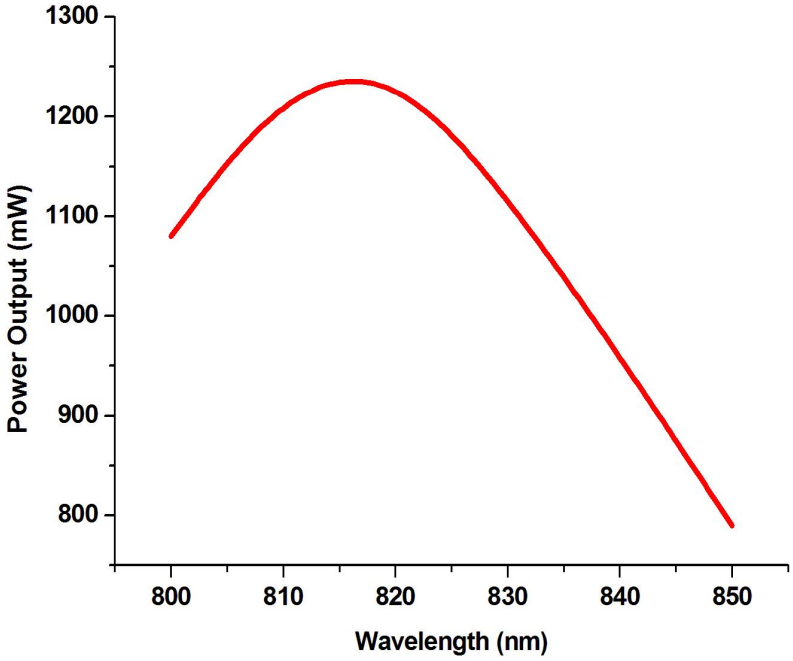

Figure 6.13: Plot shows the variation of output power of the cw Ti:sapphire laser with wavelength across the gain bandwidth. This was measured after removing the intracavity slit which is used for wavelength tuning.

able during the course of the experiments that the centre wavelength of the laser in modelocked operation did not naturally map to the cw wavelength. To understand whether this would have any impact on the results, I measured the output power of the laser as a function of wavelength. As shown in figure 6.13 a change in the wavelength can have an impact on the output power of the laser.

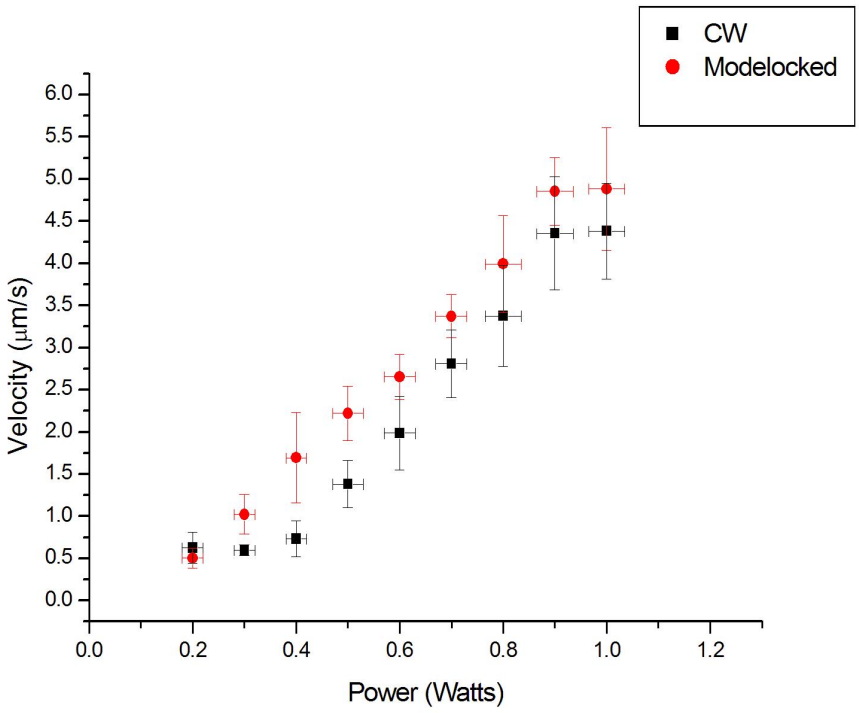

Figure 6.14: Plot shows the particle velocity ($\mu m/s$)for doped microspheres guided in a femtosecond and cw Ti:sapphire beam varying with output power

This could have been a contributing factor to the inconsistency of the experimental results. For this reason, subsequent my experimental practice included ensuring that the central wavelength for both modelocked and cw operation of the laser matched before adjusting the output power to the required level.

Water absorption was also a factor that could have affected the results. After researching the literature it became clear that small changes in the wavelength of the laser could lead to dramatic changes in the water absorption [20]. As figure 6.5 shows, water is particularly sensitive to wavelength around the infrared region of the electromagnetic spectrum. Excess heating can make optical guiding difficult as particles will drift out of the beam by thermal vibrations. This

realisation led me to try to qualitative understand the impact of wavelength and larger bandwidth of the modelocked laser output on guiding. I carried out another experiment to measure the heating effects across the region of 800 to $850nm$.

Using a pipette, I placed a water-based solution of $2.3\mu m$ polymer spheres into a cuvette I measured the particle velocities in the convection currents by the same method of analysing video footage as in the previous experiment. The laser wavelength was varied by translating the intra-cavity slit between the dispersion prisms. The power of the laser was kept constant by using a neutral density filter wheel. The particles within the cuvette could be seen to move upwards in the convection currents. Video footage was recorded for cw laser outputs at wavelengths between $790nm$ and $850nm$ at $10nm$ intervals. Using IMAQ software to grab frames and measure distances travelled, the velocities could be determined. The experiment was repeated with the laser in modelocked operation and with a centre wavelength of $819nm$ and a FWHM of $9nm$. It was not possible to move the spectral profile of the laser in the same way when it was in pulsed operation. The distribution of particle velocities is shown in figure 6.15. It can be seen from the results that the particle velocities within the convection currents increase significantly with wavelength. Also, the data for the modelocked case is consistent with the cw results. It would have been preferable to repeat the experiment in modelocked operation at longer wavelengths. Any difference between the cw and modelocked heating effects would have been more pronounced, however, it was not possible to achieve modelocking at wavelengths higher than the measured $819nm$.

The results of this study underlined the importance of selecting wavelength

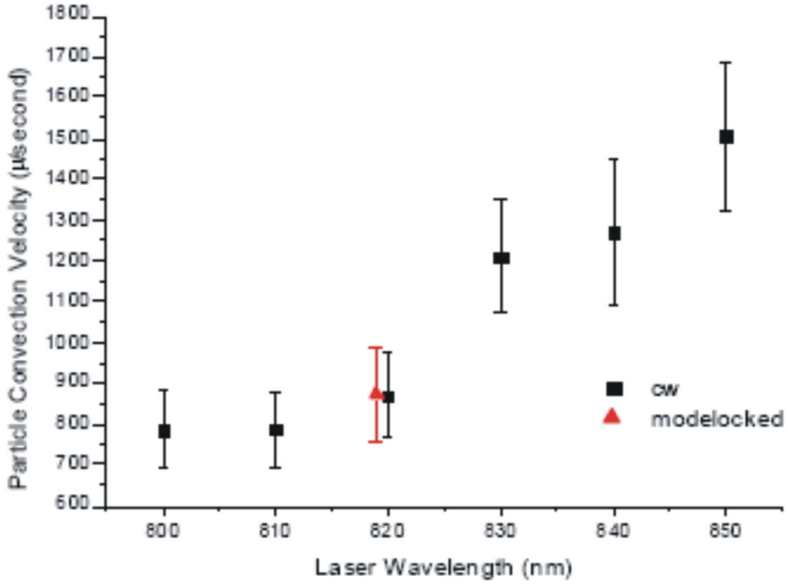

Figure 6.15: Plot shows how the convection velocities ($\mu m/s$) varies with laser wavelength for cw and femtosecond operation

in comparative guiding experiments. Furthermore, it alerted the team to the fact that water absorption would play a key role in designing experiments for biological applications.

A secondary observation from the video footage of the experiment showed that some particles were also guided in the outer rings of the Bessel beam though at a much lower velocity. At the point where the intensity gradient across the outer rings was insufficient to guide the particle, the particles would migrate outwards or hop into the inner rings and eventually into the central spot. This exhibited the "washboard phenomenon" that was explored in the research carried out by Dholakia et al. in 2003 [77].

Armed with this understanding the experiments were carried out once more.

With the improved experimental procedure I repeated the experiments using non-fluorescing $2.3\mu m$ polymer spheres. The results of this experiment which are shown in figure 6.16 show that the guiding velocities are comparable for both pulsed and cw laser beams. This leads to the conclusion that the guiding velocity of the particles is indeed governed by the average power, and not the peak power as might have been expected.

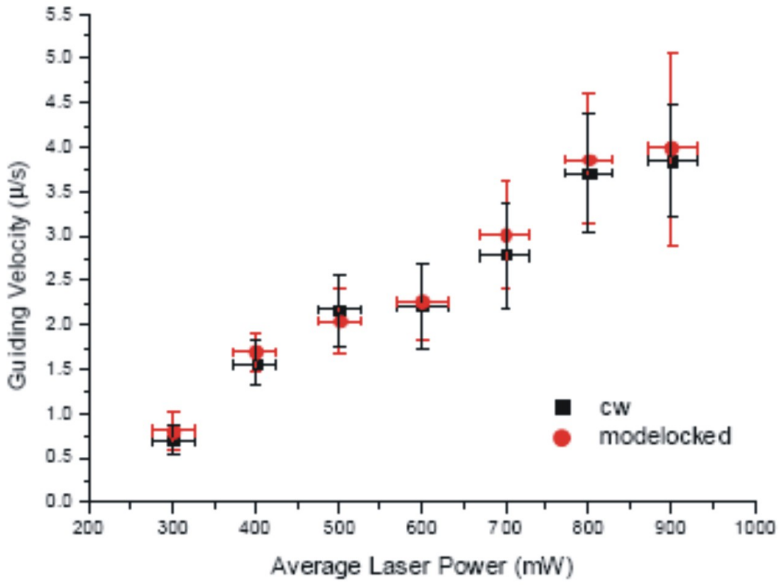

Figure 6.16: Plot shows velocities ($\mu m/s$) for $2\mu m$ polymer spheres in a Bessel beam for particles guided in cw and ultrashort-pulsed laser beams

To compare, I guided some particles in a Gaussian beam. This was done by replacing the axicon with a convex lens with a focal length of 5cm. This gave a beam waist with a diameter of $3\mu m$ and a confocal parameter of $70\mu m$. The beam was focused through the same cuvette and data was taken and analysed as for the Bessel beam guiding experiment. Again, as shown in Table 6.1 the cw guiding velocities were comparable to the modelocked case.

Average Power	**CW Velocity** $\mu m/s$	**Modelocked Velocity** $\mu m/s$
50 mW	51.9 ± 8.7	49.8 ± 5.7
100 mW	65.0 ± 11.4	67.6 ± 11.9
150 mW	94.1 ± 16.7	117.1 ± 22.4

Table 6.1: Table of averaged guiding velocities for 30 $2.3\mu m$ polymer spheres in continous wave and ultrashort-pulse Gaussian beam

Due to the power distribution property of the Bessel beam, a lower power Gaussian beam was used to enable more accurate measurements to be made. If the power was too high then the particles were guided too quickly to make measurements. The experiment was repeated with larger beam waists and confocal parameters and for a range of sphere diameters. In all instances, no significant difference in guiding velocity between the cw and modelocked case was observed. The main contributing factor to the measurement uncertainty in this experiment was that for the greater guiding velocities, the greater the error in the measurement as transit time across the screen was shorter.

From this work the conclusion was that femtosecond lasers were comparable to cw lasers in optical guiding where velocity was concerned. In a further experiment I became concerned with determining whether it would be possible to simultaneously guide a particle and excite any nonlinear effects within it. This will be discussed in the next section.

6.4 Second harmonic generation & optical guiding

At this stage the conclusion reached was that femtosecond lasers are of the same value as cw lasers in optical micromanipulation techniques. The fact cw lasers are cheaper and easier to operate would suggest it is better to use these in preference to femtosecond lasers. However, the high peak powers may not increase the guiding velocity of a particle but it may produce some phenomena that cw lasers cannot. Here, a guiding experiment is carried out which uses the output from the pulsed Ti:sapphire and guiding apparatus as before but with nonlinear crystallites as the guiding particles. First, a suitable nonlinear material was needed and I arranged for a discarded lithium niobate crystal to be crushed into particles of the order of 1 to 10 μm. This was mixed with a solution of 10:1 normal to heavy water and placed within the cuvette. Though the particles were not spherical, guiding of some of the particles was observed. If there was any second harmonic generated light from these particles it would be visible through an IR filter which would block out the fundamental beam. Even with the highest powers, no second harmonic radiation was visible. The reason for this was attributed to tight requirements of phase-matching conditions for second-harmonic generation. A different nonlinear material with higher nonlinear susceptibility was required such as potassium titanium phosphate (KTP). A broken crystal was crushed, placed into a water mixture and pipetted into the cuvette. In contrast to the lithium niobate crystals light was visible from the particles even when viewed through an IR filter. A colour image of a guided KTP fragment is shown in figure 6.17. The blue-purple radiation emitted as a result of the second-harmonic generation may be seen. Also visible is the two-photon excitation-induced fluorescence of the medium through which the

particle is being guided. This multi-photon excitation and its uses will be the subject of discussion in Chapter 7. This colour image is used here as it is much easier to identify the second-harmonic generated radiation by its colour.

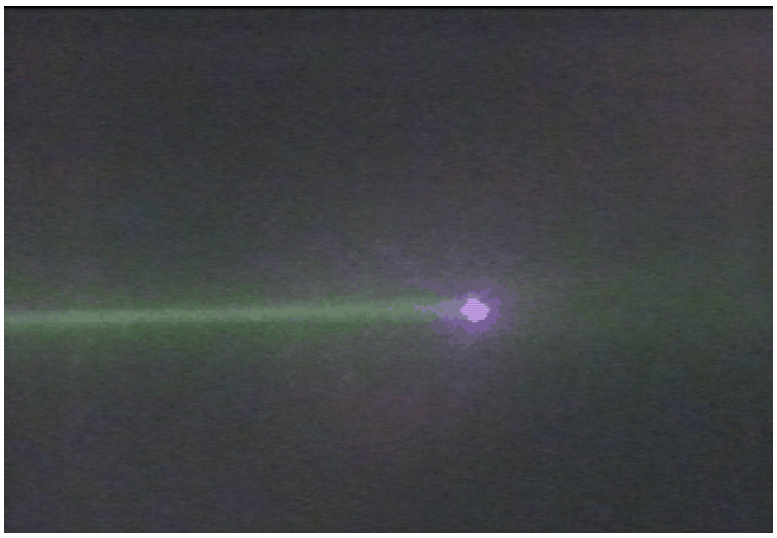

Figure 6.17: Colour image of a KTP crystal fragment, emitting a blue-purple second-harmonic radiation, being guided in a Bessel beam. The beam path can also be seen in yellow-green. This arises from the fluorescence of the medium it traverses.

This strongly suggested that a two-photon nonlinear process was taking place at the same time as the particles were being guided. The particles rotated within the beam and as this happened, the phase-matching conditions meant that there were variations in the intensity of the second-harmonic signal. Since the second harmonic intensity is dependent on the crystal length, the variation in the fragment size also contributes the variation in signal. Although proof that this was a nonlinear phenomenon was evident in the fact that no signal was visible when the laser was in cw operation, to verify this I conducted an experiment where the power of the guiding beam was varied and the two-photon signal from the particles measured. The rotation of the particles caused a

problem as a consistent measurement would not be possible. However, as the particles were guided to the end of the cuvette, the crystals pieces actually stuck together into a mass which had a significant amount of harmonic radiation. This agglomeration was relatively static and so proved to give good measurements. The measurements were taken by analysing images from the camera as viewed through an IR filter. The mean pixel intensity was measured around the agglomeration of crystals. This pixel intensity was renormalised against the background and the results are displayed in a log-log plot of intensity against power as shown in figure 6.18. A gradient of the best fit line was calculated

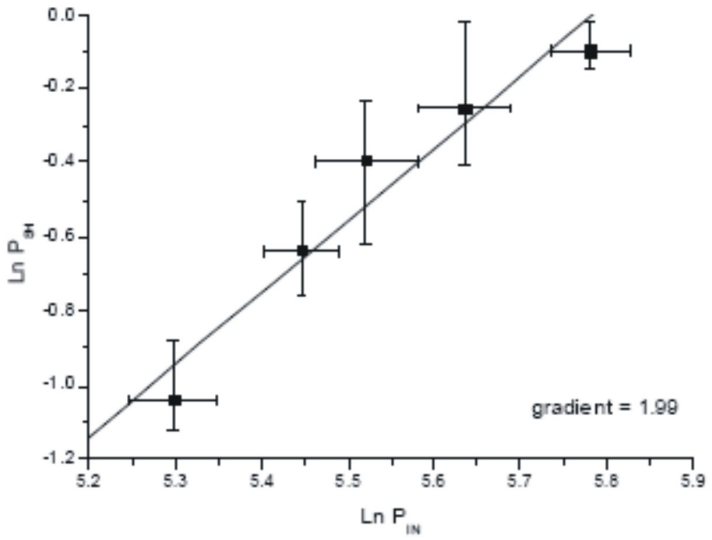

Figure 6.18: Logarithmic plot of the second-harmonic generated signal as measured by the mean pixel intensity from KTP crystallites guided in a pulsed Ti:sapphire laser beam. The gradient of the line of best fit is $y = 1.99x$ which indicates that there is a quadratic relationship between incident power and the power of the emitted radiation.

through these points as being 1.99 which confirms that the light emitted from the KTP particles had a quadratic relationship with the laser input power. As discussed in Chapter 2, multi-photon excitation is a nonlinear effect. From this

we can deduce that this was the first demonstration of simultaneous guiding and two-photon excitation in a particle.

6.5 Optical guiding with a 10 fs Ti:sapphire laser

This work which uses extremely short pulses follows the experiments which are detailed in Chapter 8 but will be discussed here. In retrospect, the experiments carried out as described earlier in this chapter could possibly have yielded more insights into femtosecond guiding if carried out using the shortest available pulses. The decision to use the higher power Ti:sapphire laser was based on the assumption that any benefits in femtosecond guiding would be from the peak power of the guiding beam rather than the brevity of the pulse duration and associated broader bandwidth. From work carried out with extremely broad bandwidth lasers, it became apparent that it is perhaps the bandwidth of the laser that could dictate the guiding properties of a beam. In the experiments carried out with the $110fs$ Ti:sapphire laser the bandwidth was in the order of 9 to $12nm$ which is perhaps not broad enough to convincingly demonstrate a difference in guiding properties of the modelocked and cw beam. However, based on the experimental results which will be discussed in detail in Chapter 8, this experiment was briefly and only qualitatively revisited at the conclusion of my research using the Femtosource laser which is capable of producing pulses with a duration as short as $10fs$.

The Femtosource laser differs greatly from its argon-ion counterpart in terms of size, ease of operation and output. As illustrated in figure 6.19, the laser

comprises a prepackaged box and a set of optical elements which must be aligned to build the laser. The box contains a system of aligned mirrors and the Ti:sapphire crystal. The pump laser comprises two of semiconductor diode lasers which are water-cooled and emit at a wavelength of $532nm$. A periscope lowers the beam path from the semiconductor diode-pumped solid state laser into the Femtosource module and also rotates the polarisation of the light by $90°$. To build and complete the laser, I had to carefully align mirrors M2 and M3 to ensure that the beam travelled twice between the two and remained horizontal. Using a power meter, I was able to maneuvre the output coupler and compensation prism in place until I measured a signal. By gently adjusting the mirrors and some controls for the Femtosource, I was able to achieve lasing. In contrast to the Spectra-Physics Ti:sapphire laser, the dispersion compensation in this laser is provided by an external cavity dispersion compensation (ECDC). With a pump laser power of $5W$ a cw output of up to $800mW$ is possible if the laser is optimised. To initiate modelocking, a transient noise spike is introduced by depressing a button on the Femtosource module. Instead of using a spectral analyser, I was able to determine whether the laser was modelocked by the change in shape and intensity of the output beam. As a commercial laser system, the output is well characterised. The spectral bandwidth of the pulses is approximately $75nm$ at central wavelength of $800nm$ and with a peak power of over $330kW$. The output beam is a TEM_{00} mode of approximately $2mm$ in diameter and a beam quality of M^2 of less than 1.3. In the previous work, the focus had been on determining whether guiding was a single or two-photon dominated effect. At the time little investigation was carried out to compare the guiding distances of particles in the two regimes. The previous work had used $110fs$ pulses from a Ti:sapphire laser. Here the experiment was performed using a Ti:sapphire laser capable of producing pulses as short as $10fs$ with a

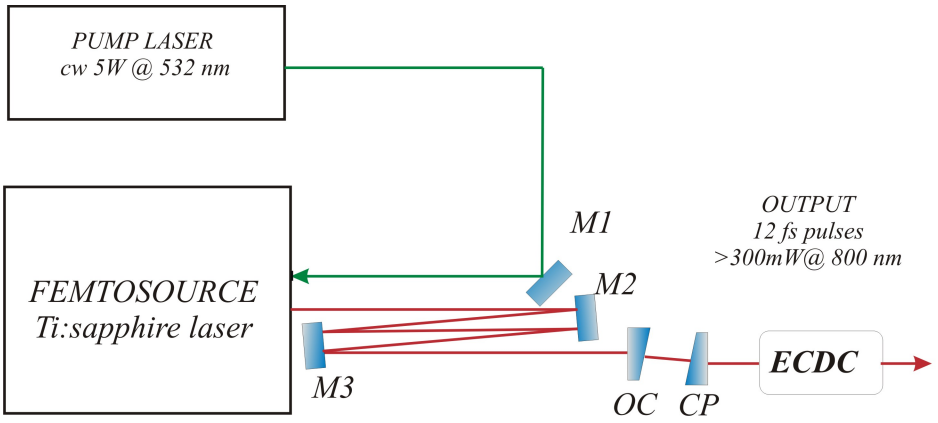

Figure 6.19: Schematic diagram of the Femtosource Ti:sapphire laser with periscope M1, mirrors, M2, M3 and output coupler , OC, compensating prism, CP, and external cavity dispersion compensation, ECDC. The periscope rotates the polarisation of the pump beam by 90°

bandwidth of approximately $120nm$ compared to $9nm$. In the previous work it was determined that cw and pulsed guiding velocities were comparable, but the same cannot be said of the guiding distances. It is, at this time, understood that it is the bandwidth of the laser source which contributes to the increased guiding distances observed in this experiment. This will be explored more fully in chapter 8, however, for completeness, images showing the distances over which the particles are guided are shown below. In figure 6.20, the $2.3\mu m$ polymer spheres are being guided by a Ti:sapphire laser with a centre wavelength of $790nm$ and $500mW$ average power. To improve visibility, these images have been processed from monochrome to intensity-related colour. The blue to red spectrum relates to increasing intensity. It can clearly be seen that more particles are guided when the laser is modelocked than when operating in cw mode, and over larger distances. Further images are shown in figure 6.21. These show that there is a marked difference in the guiding distances of particles in a cw Bessel beam as opposed to a 10-femtosecond Bessel beam. Due to the a lack of time I was not able to pursue this any further. However, the work was carried on by Pascal Fischer and Antonia Carruthers after my departure

Figure 6.20: False-colour images showing the relative guiding distances of particles within a cw Bessel beam (top) and femtosecond Bessel beam (bottom) for an output power of $500mW$.

and resulted in some very exciting results [78]. The extended guiding distances arise from the increased bandwidth of the laser when modelocked. As will be discussed further in Chapter 8, by using pulsed lasers this increases the bandwidth of the guiding beam. A superposition of beams forms to create an extended line of focus.

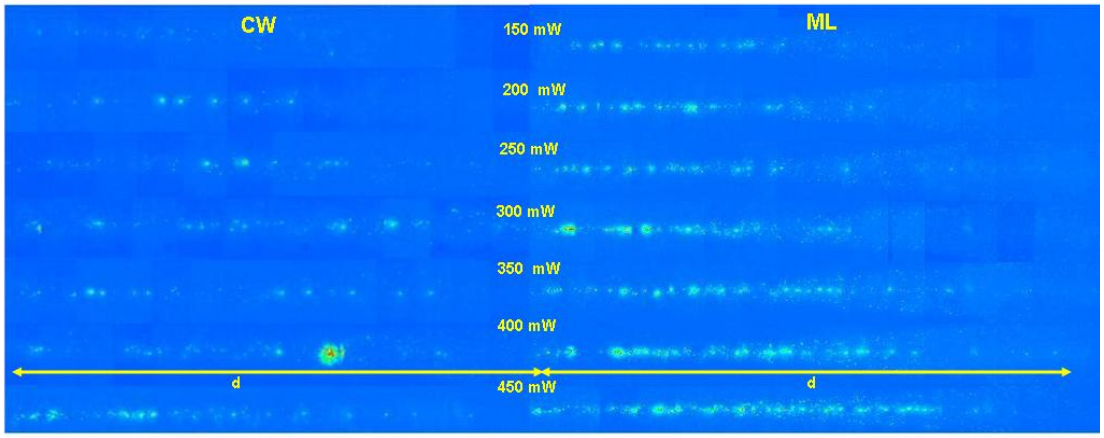

Figure 6.21: False-colour images compiled to show the approximate guiding distances of $2.3\mu m$ polymer spheres across a cuvette of length $d = 3mm$ using a Ti:sapphire laser with output powers from 150 to $500mW$ (top-bottom)

6.6 Discussion

In this chapter I have detailed the experiments which set out to compare optical guiding in ultrashort-pulsed and cw lasers in Bessel and Gaussian beam guiding. At the start of this chapter several questions were asked. From the work contained within this chapter these questions have now been answered. The outcomes can be summarised as:

- Optical guiding is governed by a one-photon effect. A comparison of the guiding velocities shows that there is no discernible difference for guiding in cw and femtosecond Bessel beams. Similarly there is no discernible difference to guiding velocities in cw and femtosecond Gaussian beams.

- The high peak powers associated with ultrashort pulses can be used to exploit nonlinear phenomena such as second-harmonic generation in microscopic objects at the same time as they are guided.

- The absorption of water at the infrared region of the electromagnetic spectrum is particularly sensitive to wavelength and must be considered in guiding work.

- There is evidence which shows that extended guiding distances are possible by using ultrashort pulsed lasers with broad bandwidths. This will be discussed further in the final experimental chapter of this thesis.

These outcomes were positive and they led to other work. The simultaneous multi-photon excitation and guiding prompted similar investigations by other members of the group into optical tweezing [79]. It also encourage further work into multi-photon excitation which will be the subject of the next chapter.

In retrospect it would have been preferable to carry out all the guiding experiments with the shortest pulses using the Femtosource laser. However, the sequence of experiments led to a wider understanding of various femtosecond lasers as well as better understanding of the relative properties of Gaussian and Bessel beams.

Personally I gained familiarity with laser construction as the Cr:LiSAF was not a turn-key laser. The work allowed me to gain experience in laser modelling and autocorrelation techniques as well as setting up Bessel beam generation experiments. Moving to the $110fs$ Ti:sapphire laser gave me the opportunity to gain experience in laser maintenance and optimisation as it often needed realignment. Finally, the Femtosource laser provided further opportunities in cavity alignment.

The lack of results with the experiments with the Cr:LiSAF led to a better understanding of the power distribution in Bessel and Gaussian beams. Armed with more knowledge of Bessel beams at the time, I would have been able to calculate that the power density within the central spot of a Bessel beam would have been unlikely to allow guiding. Similarly a Bessel beam generated by the Femtosource would have had a power density in the central spot of approximately forty times that of the $110fs$ Ti:sapphire laser. However, at the

time, the laser was being used by a colleague for other research. Also, there were concerns that the extremely short pulses could lead and unwanted dispersion effects which could obfuscate the underlying results of the experiments. For this reason, the alternative $110 - fs$ Ti:sapphire source was considered to be the optimum ultra-short pulse laser.

There was several repetitions of the experiments through which I gained a better understanding of the factors which could influence optical guiding. Since absorption of water was wavelength depended, most critical was ensuring that the centre wavelength of the laser was maintained in both cw and femtosecond operation. The comparison of Bessel and Gaussian beams raised some discussion. How can a fair comparison be made when the power distribution and propagation distances are so different between the two? A comparison could be made with the same power and for the same spot size or for the same propagation distance but not simultaneously. Since it was not possible to exactly measure the number of rings in a Bessel beam it was not possible to isolate the power contained within the central spot. Hence it was not possible to accurately choose a comparable power for a Gaussian beam with a spot size of the same size as the central spot of a Bessel beam. As we were more interested in guiding over extended distances, the focus of the experiments was on Bessel beam guiding, though experiments were also carried out to verify that consistent results came from guiding with femtosecond and cw Gaussian beams.

An ambition was to measure the guiding distances of particles within the beam. At the time, I was not able to develop a method that could accurately do this. It was not possible to record the transit of a single particle across the whole cuvette without translating the microscope objective and camera. For later experiments

I was able use a higher quality XYZ-translation stage to take images along the length of the cuvette at known intervals. Some particles were imaged more than once this way but I was able to get an approximation for the propagation distance as shown in figure 6.20. If I had developed this technique in earlier experiments I would have identified whether guiding distance in femtosecond laser beams were greater than in comparable cw beams.

In summary, the learning and exciting results from this experimental work provided a good foundation from which to develop further work. In working with Bessel beams, I was aware of the self-healing nature of the beam. Many particles could be guided along the propagation of the beam. The use of the pulsed lasers prompted the question - could we somehow use the high peak powers to somehow help us visualise and then characterise this self-healing property? The answer lay in the two-photon excitation-induced fluorescence of a substance called fluorescein. We will now go on to discuss this exploration in the next chapter.

CHAPTER 7

Two-photon excitation in optical manipulation

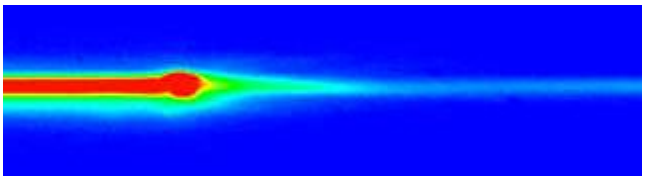

In Chapter 6 we learned that optical guiding was governed by the average power of laser. One could be forgiven for thinking that there was no real benefit for using the often more costly femtosecond lasers in place of cw lasers. However, as was successfully demonstrated it is possible to use use the high-peak power of these ultrashort pulses for multiphoton excitation which is just not possible with conventional cw lasers. Having carried out *simultaneous* optical guiding and second-harmonic generation in a Bessel beam the idea of using these ultrashort pulses to explore other multi-photon techniques became very attractive. The ability to visualise rather than model particle interactions would be of considerable interest. From the work detailed in this chapter, some steps have been taken to realise this.

7.1 Fluorescein & fluorescent markers

In 1871 von Baeyer first synthesised an organic compound that became the first dye to be used *in vivo* to track the secretion of aqueous humour in the eye and until relatively recently, fluorescein remained the most dominant fluorophore. Used diversely in applications from fluorescence microscopy to large scale water route mapping, it is characterised by its high absorptivity, high fluorescence quantum yield and good water solubility, however, in its purest form it suffers from photobleaching and a pH-sensitive fluorescence emission. As shown in figure 7.1 it is excited in the visible spectrum and has a maximum excitation at approximately 494 nm and an emission maximum at approximately 520 nm. Research into fluoroscein synthesis has continued with amine-reactive enabling labelling of proteins as well as a series of photostable pH-insensitive derivatives. In microscopy, fluorescent probes have been used extensively for the tracking of subcellular organelles. Fluorescein and its derivatives have been overtaken by the use of fluorescent proteins as probes. A green fluorescent protein (GFP) is naturally produced by the jellyfish *Aequorea victoria*. By cloning the GFP gene, variants of the protein with different excitation and emission spectra have been produced. Characterised by their emission maxima in the blue, yellow and red regions of the visible spectrum, blue, yellow and red fluorescent proteins are increasingly in use as fluorescent probes. By combining genes coding for a specific protein with GFP and its variants, functional and fluorescent chimera were created thus allowing more sophisticated tracking of organelles and their functions. However, their precursor, fluorescein, remains a key fluorophore in diagnostics. Another property of fluorescein that is of keen interest and has not been exploited until very recently is that it undergoes two-photon excitation.

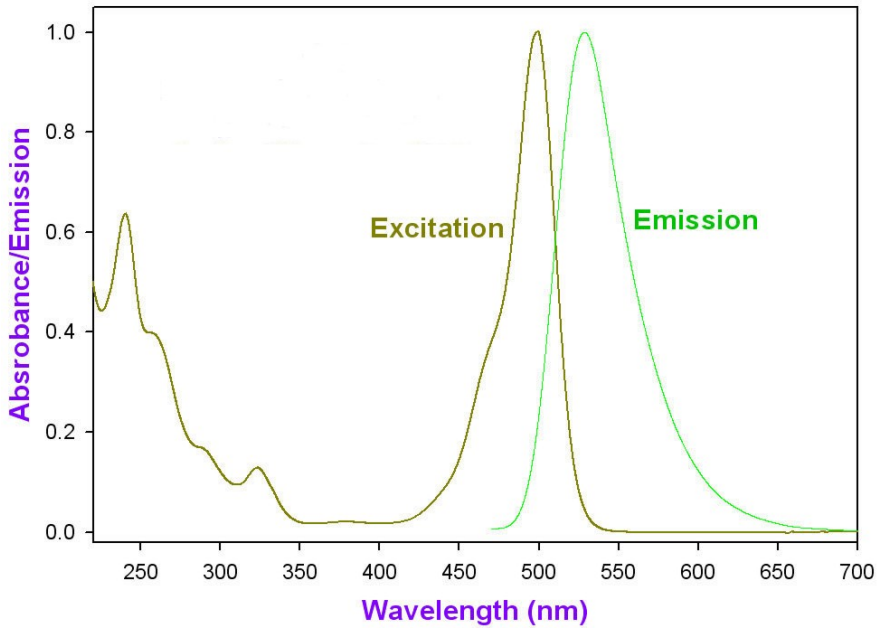

Figure 7.1: Plot showing the absorption and emission spectra of fluorescein in pH neutral solution[80].

The excitation spectrum of fluorescein extends into the blue-green region of the spectrum meaning that it can be excited by wavelengths in the infrared.

Fluorescein in its solid form, is a yellow-orange crystalline substance which is soluble in water or methanol to make an orange liquid which has a strange hue. When placed in the path of an infrared beam there is no discernible change in the liquid. Unless that is, the output from the laser beam is pulsed and therefore offers high enough intensity to produce two-photon excitation of the fluorescein. It is then possible to observe with the naked eye a green glow marking the beam path of the laser. It is possible to see the fluorescence in the images shown in figure 7.2. A Gaussian beam is directed upwards through a containing fluorescein. Due to the response of the camera, the fluorescence shows as purple glow. In a larger container it is possible to see the extent of the

beam as shown in figure 7.3. After first observing this effect, we set out to use fluorescein to visualise, compare and investigate the properties of the Bessel and Gaussian beam shapes.

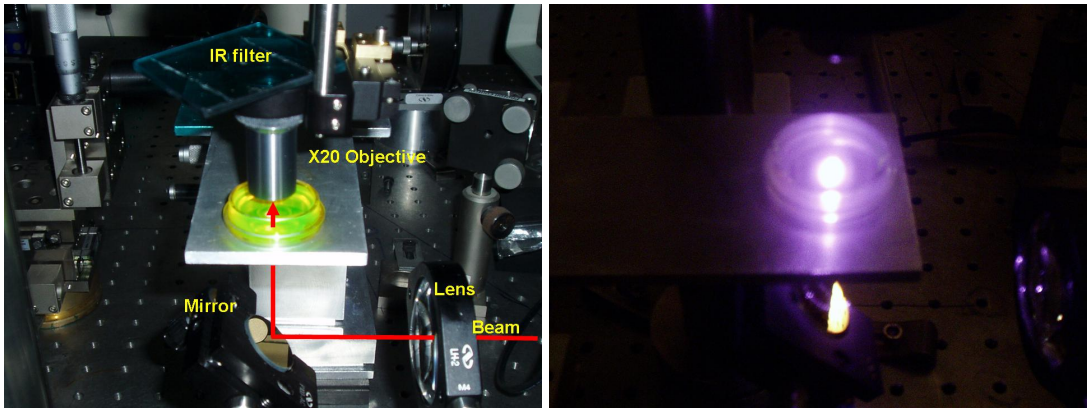

Figure 7.2: A femtosecond Gaussian beam is directed by a mirror upwards through a chamber containing fluorescein (l) which is imaged through an infrared filter to allow measurement of the two-photon excitation-induced fluorescence signal(r).

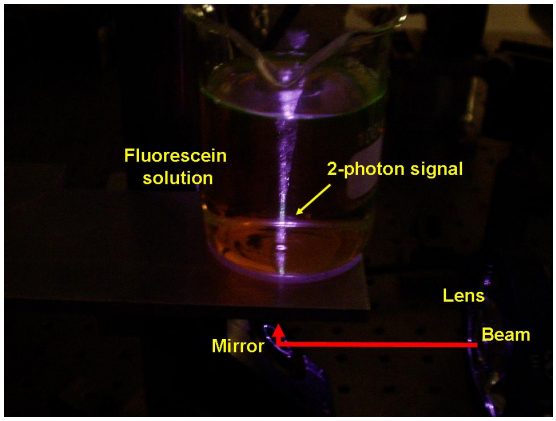

Figure 7.3: A femtosecond Gaussian beam is directed by a mirror upwards through a beaker containing fluorescein showing a visible two-photon signal.

7.2 Visualisation of Bessel & Gaussian beams

To investigate the propagation of the Bessel and Gaussian beams a Ti:sapphire laser operating at a central wavelength of $790nm$ was used. It was possible for me to switch operation from cw to modelocked by introducing a transient perturbation of the end cavity mirror. Equally simple was moving to cw operation by introducing a transient intra-cavity obstruction. First, the Bessel beam was investigated and so for this experiment, I used the same guiding apparatus as in previous work previously. Here, the central spot size was approximately $5\mu m$. A water-based solution of fluorescein was placed in a clean cuvette situated at the beam focus. Using a translation stage, microscope objective (x20), CCD camera (Pulnix) and video cassette recorder (VCR) I was able to take images along the beam axis. I used a neutral density to filter to vary power levels as I took a series of images at different, discrete powers. By using IMAQ Vision Builder software (National Instruments) I was able to capture and transform still images from grainy, monochrome to sharp, vibrant false-colour pictures. These were then collated into a single image which shows the whole beam as it transverses the cuvette. The experiment was repeated using a Gaussian beam with a spot size of approximately $5\mu m$ as illustrated in figure **??**. Due to the power distribution over the Bessel beam structure, lower powers were needed to generate similar levels of fluorescence intensity for the Gaussian beam images. The images were captured, processed and collated as for the Bessel beam images above. A comparison of the images shows how the central maximum of the Bessel extends far greater than a Gaussian beam with similar spot sizes. It also shows how the extended guiding distance comes at the cost of power within the central core. It is worth noting that these images are generated by the

nonlinear response of the beam within the fluorescein. The region over which Gaussian guiding can take place is still constrained to a region smaller than the high intensity profile would suggest. Figure 7.4 show the profiles generated for a Bessel beam with $950mW$ of average power (top), a Gaussian beam with an average power $950mW$ (middle) and finally $100mW$ (bottom). As shown

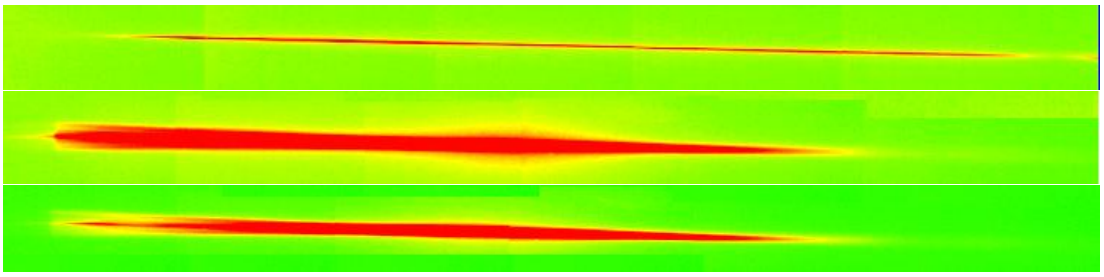

Figure 7.4: False colour images show the beam propagation of a Bessel beam of 950mW of average power (top) Gaussian beam of 950 mW average power (middle) and a Gaussian beam of 100 mW average power (bottom).

in figures 7.4, the Gaussian beam (top) has a much higher intensity compared to that of the Bessel beam (bottom), however the propagation distance of the Bessel beam exceeds that of the Gaussian beam.

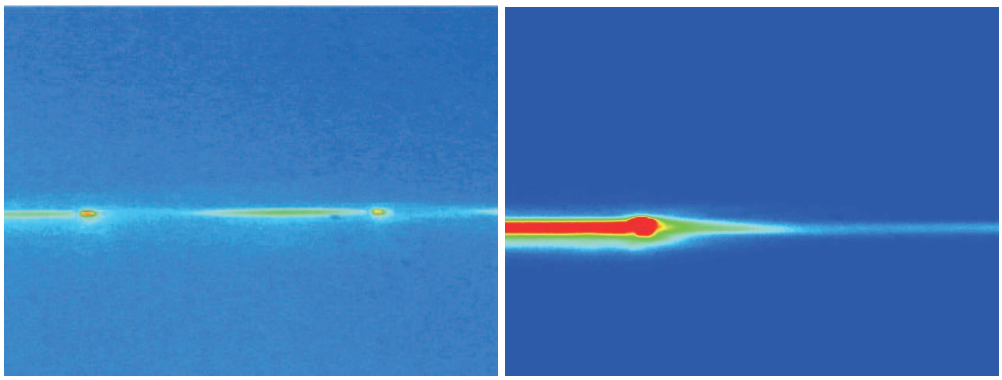

Figure 7.5: False-colour images show the beam propagating through fluorescein and guiding particles in a Bessel beam (l) and a Gaussian beam (r). The two-photon excitation-induced fluorescence indicates the relative intensity of the beams and the reconstruction property of the Bessel beam

From this work, we were able to use the technique to visualise and compare the reconstruction properties of Gaussian and Bessel beams. In this experiment, I placed a sample of non-fluorescing polymer $2.3\mu m$ spheres in the fluorescein solution. Optical guiding was observed in both beams however the images also reinforced the theory. As can be seen in figures 7.5, the Gaussian beam (right image) shows an intense beam guiding a single particle from left to right. There is no evidence of a beam downstream of the particle. In contrast, the self-healing properties of the Bessel beam which were discussed in Chapter 4 can be seen as two particles are guided from left to right with a two-photon signal present in between (left image).

I was able to use these images to estimate the reconstruction distance of the particle within the beam. By using IMAQ software I took a line profile of the image and analysed it within Microcal. A renormalised plot as shown in figure 7.6 gives a measurement of 65 and 68 μm respectively for the two particles. We were able to compare this result with a simulation created by a colleague. In a comparison with the theory as detailed in Chapter 4, for a $2.3\mu m$ particle in a beam with axicon of angle $\gamma = 1$ and refractive index $n = 1.5$, the reconstruction distance is approximately 66 μm.

This work shows good comparison of experimental results to the theory of self-healing Bessel beams. In the next section, the aim was to investigate whether this property would show allow for deeper penetration through turbid media.

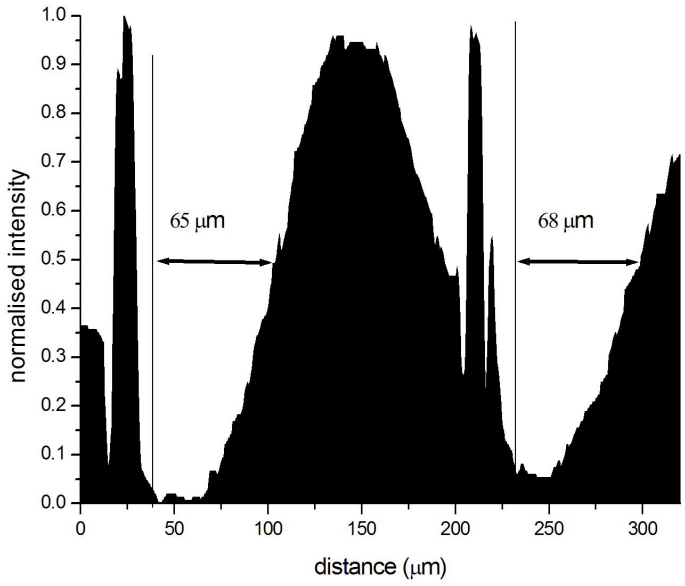

Figure 7.6: Line profile to show reconstruction of Bessel beam around guided microspheres of diameter $2.3\mu m$

7.3 Multi-photon processes in turbid media

In this section we explore the reformation of Bessel beams for nonlinear excitation through turbid media. The self-healing properties of Bessel beams which were this basis of this work was driven by a desire to better understand the penetration of Bessel light beams into turbid media with potential applications for deep tissue penetration. Initially we look qualitatively at two-photon excitation of blue fluorescing spheres, KTP crystallites and fluorescein through very turbid media. Subsequently, we set about trying to qualitatively measure the penetration of Bessel beams versus equivalent Gaussian beams through turbid media. The aspiration is to translate any positive findings into applications in the probing of deep tissue.

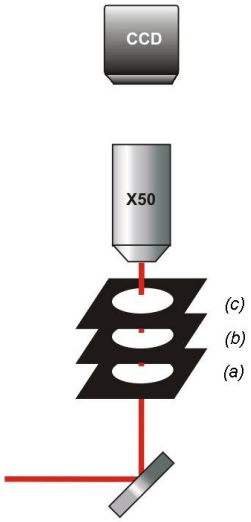

Figure 7.7: Schematic showing a vertical Bessel beam travelling through a series of chambers containing nonlinear materials in solutions. (a) blue fluoresecing spheres, (b) KTP crystalites and (c) fluorescein

In the first experiment, we use a series of small chambers each containing different substance which, under the correct conditions would exhibit either 2-photon excitation or second harmonic generation. An illustration of the simple experimantal apparatus is set out in figure 7.7. To make the sample chambers, I used a series of microscope slides and cover slips. Sheets of sticky-backed plastic were pre-fabricated into a mesh of squares with holes cut out. These were stacked to make the sample chambers. I used pipette to place a measured solution of fluorescing particles into the chamber which was sealed with a small thin cover slip. As a demonstration, some images were captured to determine whether further experiments were warranted. As the images show, it was possible to excite fluorescing spheres, KTP crystal fragemnts and fluorescein even when the samples were highly concentrated. Figure 7.8 shows the Bessel beam as imaged through a sample with a low concentration (left) and high concentration (right) of non-fluorescing $5\mu m$ polymer spheres. Above this, a second sample chamber contained 5 μm green fluorescing spheres. Finally a

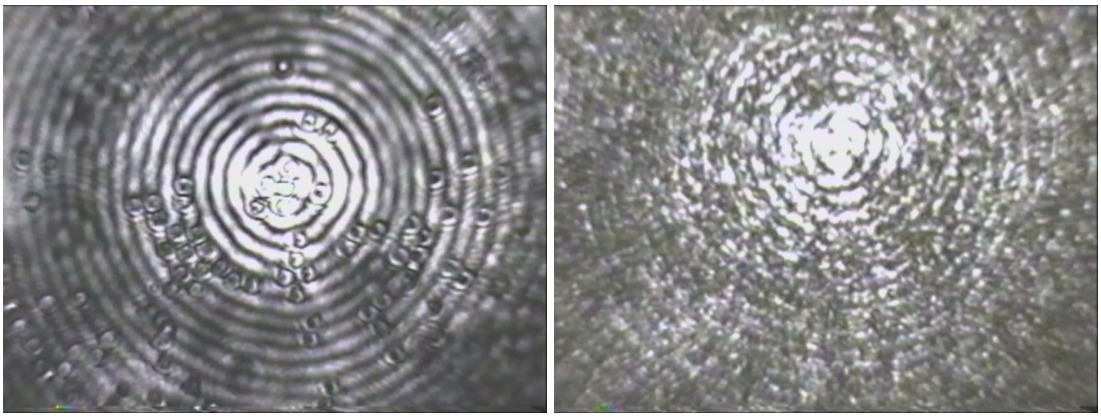

Figure 7.8: Images of Bessel beam within first sample stage with no IR filter. (l) with dilute concentration of non-fluorescing spheres; (r) with high concentration of non-fluorescing spheres as used in experiment

third chamber containing KTP crystal fragments was placed on top. I was able to image through the sample chamber using an IR filter to determine if there was any two photon signal from the spheres or KTP fragemnts. As is showm in figure 7.9, a strong signal is emitted from both.

I also noted that the beam itself introduced convection effects within the sample chamber. Particles trapped within the Bessel beam were guided upwards to the top of the chamber where they would arrange themselves within the high intensity areas of the central spot and outer rings. The two images in figure 7.10 shows how 1 micron blue fluorescing spheres arrange themselves within a Bessel beam with a 2 micron diameter central spot.

These investigations showed that it was possible to achieve nonlinear excitation of materials even through a turbid material. From this, the aspiration was to qualitatively determine whether Bessel beams exceeded Gaussian beams in penetration depth through turbid media.

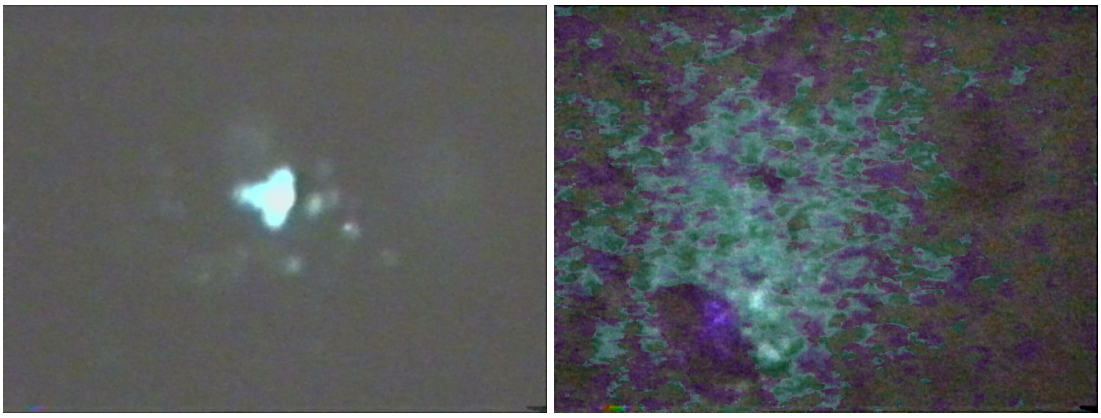

Figure 7.9: Images of Bessel beam through in second and third chambers: (l)as imaged in middle chamber with strong concentration of green fluorescing spheres; (r) as imaged in top sample containing KTP crystallites

Figure 7.10: $1\mu m$ blue fluorescing spheres within a femtosecond Bessel beam with a central spot size of $2\mu m$. The particles self-assemble into the Bessel beam pattern

7.4 Penetration through turbid media with Bessel beams

In this experiment, the two-photon signal from fluorescein is used to measure how well a beam penetrates through a high concentration solution of non-fluorescing polymer spheres. Using 5 different beam powers (20 to 100 mW), 3 solution concentration, 3 different particle sizes and several chamber depths, images of the fluorescein chamber were captured and analysed using IMAQ software. For this experiment, I used a Bessel beam with a central core of 5 μm

and a length of 6 mm. Initial I used large polymer spheres with a diameter of 25 μm. The size of the spheres proved to be too large to allow the Bessel beam to reform. Equally, the Gaussian beam was quickly attenuated. Therefore, I moved to using particles with a diameter of 1 and 6.53 μm non-fluorescing polymer spheres. For Mie particles I used smaller 470 nm particles labelled with a red fluorophore. As illustrated in 7.11, the polymer solutions were placed into a chamber (C) of a known thickness (B). The beam (C) enters the chamber and the two photon signal from the fluorescein in the chamber (A) is measured. To avoid contamination, a chamber was made for each sample. The chamber was constructed by overlaying a series of plastic chambers each measuring $80\mu m$ thick. The concentrations of polymer spheres to water were 1:30, 1:60 and 1:90. To make the solution more turbid, I refrained from adding any heavy water to the solution. To compare, a Gaussian beam with a spot size $5\mu m$. I conducted the experiment with the same powers. As confirmed earlier in the chapter, the Gaussian beam contains much more power within the spot size compared to the same size of central core in a Bessel beam. For this reason, I observed greater signals at shallower chamber depth and therefore commenced my experiment at greater depths.

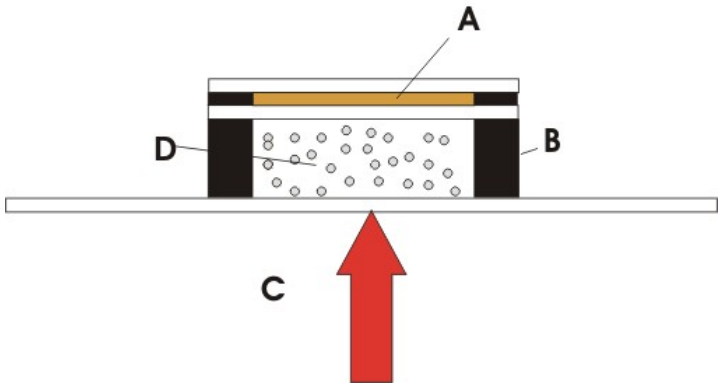

Figure 7.11: Schematic of sample chamber used to determine the penetration of beam through sample. (A) fluorescein chamber for measurement of 2 photon signal (B) chamber wall (C) beam path (D) polymer sphere solution

In the course of this experiment, I captured and imaged over one thousand images. Some of these images are shown in figure 7.12. Each image was characterised by its mean pixel intensity and plotted with depth of chamber for each of the samples at each of the beam output powers.

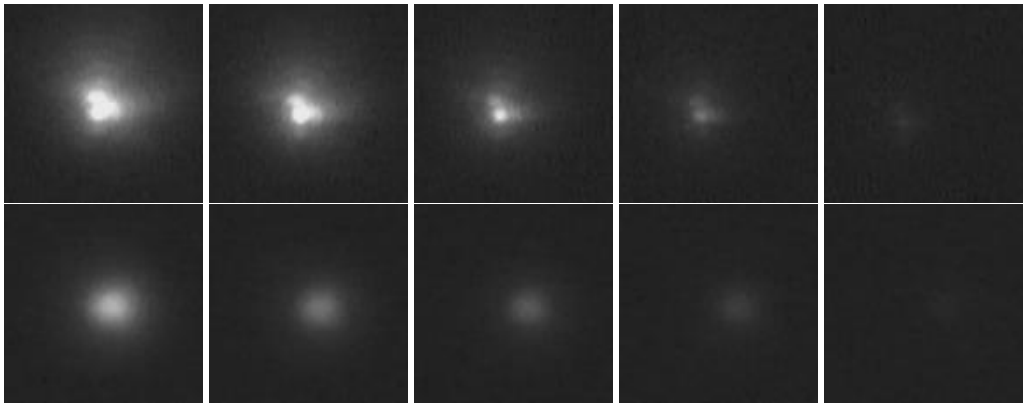

Figure 7.12: Images of two-photon excitation-induced fluorescence from fluorescein as generated by a Bessel beam (upper) and Gaussian beam (lower) propagating through a chamber containing a concentrated solution of 1 micron polymer spheres. Output power from laser is decreased from 100mW to 20mW (l-r) and the sample depth is approximately 2.4 mm

From the results it appeared that the Bessel beam had better penetration through the chamber with 1:30 in solution of red polymer spheres of diameter $470nm$ as shown in figure 7.13.

The first observation was that the signal was quickly attenuated for the $6.53\mu m$ diameter particles. This reinforces the observation that for effective penetration, the core or spot size of the beam should be greater than the particle size. The second observation was that the signal was greater for penetration through the smaller 0.47 μm spheres. However, this could be explained by the fluorescence of the spheres themselves. From the results it became evident that the experimental data was inconclusive. As shown in **??**, there was no clear trends to be seen across the piece.

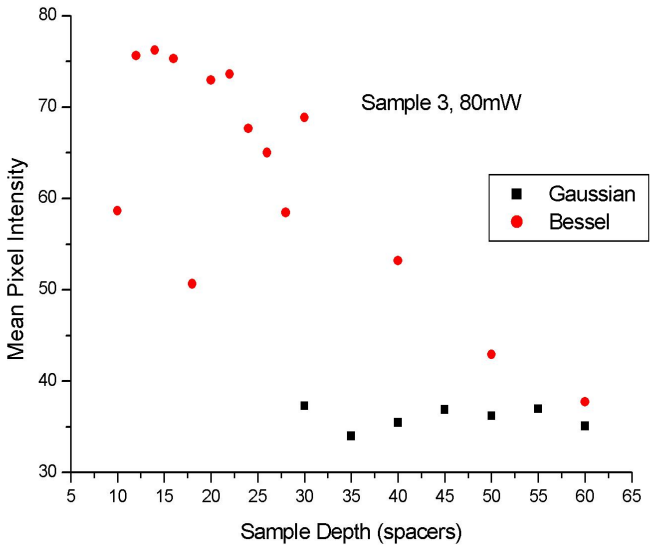

Figure 7.13: Plots show the mean pixel intensity of two-photon excitation-induced fluorescence signal for Bessel and Gaussian beams with an average power of $80mW$ propagating through a chamber containing particles of and $470nm$

For conclusive results, a better experimental methodology was required. First and foremost, the measurements should have been made for the same sample chamber depth for each beam. This was done in work continued by a colleague. In that work, a cuvette was used as a container for different concentrations of solution. A silicon-diode detector was used to measure any signal from both the Bessel and Gaussian beams for varying powers and solution concentrations.

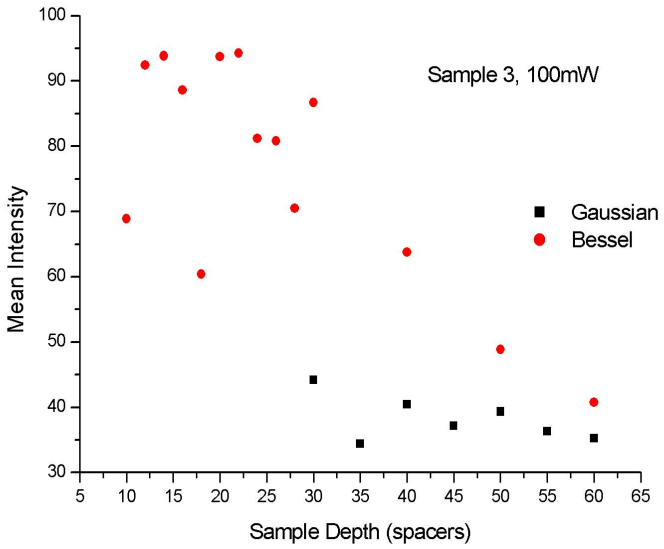

Figure 7.14: Plots show the mean pixel intensity of two-photon excitation-induced fluorescence signal for Bessel and Gaussian beams with an average power of $100mW$ propagating through a chamber containing particles of diameter $470nm$

7.5 Discussion

There were several positive outcomes from the work detailed in this chapter.

- Most significantly we successfully exploit multiphoton excitation by ultrashort pulsed lasers as a visualisation technique. From this it was possible to compare the theoretical reconstruction distance of a Bessel beam around an object by direct measurement. This image was derived from the two-photon excitation-induced fluorescence generated by a femtosecond laser Bessel beam as it reformed around the object.

- By exploiting the self-healing properties of a Bessel beam it was possible to generate second-harmonic generation and two-photon excitation-induced fluoresence through solutions with extremely high concentrations.

- The self-healing properties of the Bessel beam through turbid media were observed for particles with a diameter smaller than the central spot size of the Bessel beam.

From the previous work on the reconstructive properties of the Bessel beam the aim was to investigate the potential of Bessel beams for deeper penetration into tissue. In this set of experiments, I set out to measure the penetration of Gaussian and Bessel beams through turbid media as a function of particle concentration and depth.

After reviewing the work, a much more fruitful approach would first be to measure the penetration of the beams as a function of only one variable. The main flaw in the experiments I carried out was the construction of the chambers. Though the idea was sound in theory, the practicalities of making chambers of different depths led to the inconclusive results. It was not possible to measure accurately the chamber depth. An alternative method was to use a chamber of a standard size and measure the penetration of the beams as function of particle concentration. Rather than measure the two-photon excitation-induced fluorescence from the fluorescein chamber, a better method would be to simply measure the output power from the sample chamber using a photo-multiplier tube through an IR filter.

This experiment was not as successful as I had hoped. The intention was to redesign the experiment and repeat the experiment. However, this work was picked up by others in the group as part of another group of experiments using longer wavelength lasers. It should be noted that a paper published in 2004 by another group successfully carried this work to completion.

CHAPTER 8

White-light Bessel beams

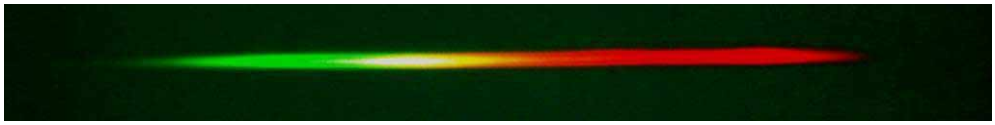

In this final chapter some very exciting research is detailed. My work until this point had been to explore multiphoton excitation and optical guiding using ultrashort pulsed lasers and Bessel beams. As my research was coming to an end, some members of the group had started working with white-light sources to explore the generation of broadband beams. I was keen to get involved with this work as it seemed to be a natural extension of my research. In this work, we used a femtosecond laser to investigate the generation and properties of Bessel beams with spatially coherent white-light sources. Given the broad bandwidth of this source, it was not known whether it would be possible to generate Bessel beams using an axicon. It was possible that the bandwidth would lead to a washing out of the Bessel beam structure. Alternatively it might behave as a superposition of many Bessel beams at incremental wavelengths. This work subsequently led to some initial experiments into optical guiding with white-light Bessel beams. Although I was unable to finish this work myself, it led to related investigations by others within the group [78]. Before, detailing this work, we will discuss the creation of this white-light source called the

supercontinuum which could find very useful applications in optical imaging.

For optical imaging techniques, the ultimate light source would have the coherence and intensity of a laser source and a spectral range that spans the UV to IR wavelengths. The use of such coherent white-light sources could potentially revolutionise *in vivo* optical imaging techniques as it is here that the aspiration is to obtain functional images of inside the body. This is best achieved when spatial and multi-wavelength information is combined. As we will discuss, the key properties of the supercontinuum that could be exploited in for such optical imaging techniques are its extremely broad spectral range, coherence and high intensity.

First it is worth considering contrasting and comparing the supercontinuum light with other white-light sources. The obvious comparison is to the light-bulb. The benefits of the incandescent light-bulb are limited to its low manufacturing and operating costs. While supercontinuum sources require sometimes expensive pump sources, it is easily coupled into a waveguide and has a coherent, intense output. Alternatives have included coupling three lasers with from the green, red and blue regions of the spectrum to produce a pseudo-white light source [81]. Although such a configuration would overcome the limitations of the light-bulb, the costs and limited spectral range render it far inferior to the supercontinuum for applications in optical coherence tomography and spectral characterisation. More technically, the coherence of the white light sources is an important consideration. In an earlier experiment by Fischer et al., a halogen bulb and a supercontinuum light source were characterised[82]. Both of these approximate to a white light source, however, the halogen bulb has a far lower spatial coherence than the supercontinuum. A series of pinholes were

used to spatially filter the light from the halogen bulb incident on an axicon. The pinhole diameter was increased, and the Bessel beam formation imaged. It was found that the outer rings in the Bessel beam became degraded with increasing pinhole diameter. It was deduced that the spatial coherence of a source limited its ability to fully form a Bessel beam in this manner. Consequently, the supercontinuum, with its high spatial coherence, is a superior white light source.

8.1 Supercontinuum generation

Before setting out the experimental work, it is important to discuss the physics of supercontinuum generation itself. The technique of converting the output from a narrow bandwidth pulsed laser source into this amazingly broad spectrum of pulses is relatively new. For this reason, a complete understanding of the mechanisms which contribute to the process has, at the time of writing, not yet been achieved. However, there are several nonlinear mechanisms which are believed to combine to launch the process. In the following section, these nonlinear processes are mentioned however the reader is referred to Chapter 2 for an more in-depth treatment.

First let us consider an early method used for generating a supercontinuum [83]. In an experiment which borrowed techniques from pump-probe spectroscopy the feasibility of simultaneously acquiring time-resolved data at a continuum of wavelengths was explored. The output from a modelocked Ti:sapphire laser producing 38 mJ optical pulses at 780 nm with a duration of 200 fs was focussed

into a cell containing water. The resulting strong nonlinear optical processes and high power densities combined to broaden the spectral bandwidth of the ultrashort pulses. With the aid of a polychromator and a streak camera, it was possible to record temporal profiles against wavelength simultaneously. From this, the researchers were successfully able to transilluminate and image breast tissue and subsequently identify inclusion.

Since then, supercontinuum generation techniques have advanced. Highly dispersive photonic crystal fibres have replaced water as the broadening medium. "Holey", microstructured, and tapered photonic crystal fibres (PCFs) are descendants of the optical fibres used in modern telecommunications technology. In traditional optical fibres, the light is guided by virtue of total internal reflection which is made possible by the relative refractive index of the core and cladding. In photonic crystal fibres, the guiding mechanism is a more subtle one; the index differential is obtained by creating a matrix of materials with various refractive indices. This matrix formation allows the manufacturer to create materials with novel dispersion properties or simply with very low refractive index. The title would suggest that the fibres are made from some crystalline material however it is in fact the distinctive cross-sectional pattern which gives photonic crystal fibres their name. Some examples of these structures are shown in figure 8.1 .

These "holey fibres" comprise a solid-index core encased in an array of air tubes are arranged along the length of the fibre. The result is a hybrid air-silica material with a refractive index lower surrounding a higher index core. The relative dimensions of the core diameter, hole diameter and separation determine, to a great extent, the properties of the optical fibre. Single-mode guiding is achieved

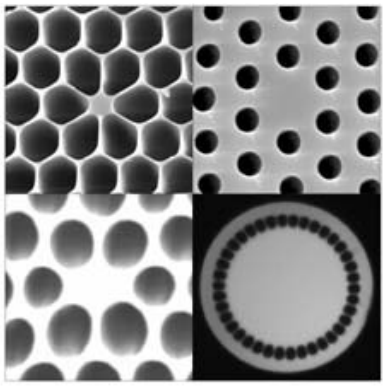

Figure 8.1: PCF structures developed for different applications. From top left clockwise (a) highly nonlinear fibre (b) endlessly single-mode fibre (c) high NA fibre and (d) polarisation maintaining fibre

by fabricating a matrix of small holes around a larger core; for multi-mode guiding, the reverse holds. In either case it is the large refractive index step which enables confinement of the light to the silica core. The dispersive properties of the fibre act to shift the zero dispersive wavelength of silica, 1270 nm, to a much shorter wavelength. For telecommunications applications, the wavelength of the pulses are matched to the zero dispersion wavelength of the material as the desire is to minimise the spectral broadening of the pulses as they propagate through the fibre. In supercontinuum generation the aim is to encourage the spectral broadening. For this reason the wavelength of the pump source should reside in the lower end of the desired spectrum.

The broadening mechanisms are not yet fully understood but it is believed that the interplay of four-wave mixing, stimulated Raman scattering and self-phase modulation are integral in the broadening effect. The determining factors for the supercontinuum generation are the dispersion of the fibre relative to the pumping wavelength, the pulse length and the peak power. The magnitude and sign of the dispersion is key in determining the particular nonlinear

processes which will dictate the stability and spectral profile of the continuum. Low dispersion is required to achieve efficient broadening as it facilitates the phase-matching needed for nonlinear processes. The high peak powers of the pulses increases the nonlinearity of the fibre and boosts the dramatic super-broadening of the laser pulses and therefore allows for shorter fibre lengths. Consider a photonic crystal fibre with a zero dispersion wavelength at $900nm$. When the PCF is pumped with femtosecond pulses at 800 nm in the normal dispersion regime, self-phase modulation is the dominating broadening mechanism with Raman scattering acting to broaden the longer wavelengths. The result will be a spectrum with a smooth and stable profile. Figure 8.2 shows that as the pump wavelength moves closer to the zero dispersion wavelength other nonlinear processes will come into effect. The Raman scattering and self-phase modulation will broaden the spectrum into the anomalous dispersion regime and therefore form a soliton at approximately $940nm$. As the peak power of the pump pulses increases, this soliton will move to longer wavelengths.

Supercontinuum generation techniques, being relatively novel, are being explored and developed. In essence, the technique involves coupling a carefully crafted photonic crystal fibre structure to a suitable laser source near the zero dispersion wavelength to generate a supercontinuum output. If the PCF is manufactured in such a way as to blue-shift the zero dispersion wavelength from the IR to the NIR, it becomes possible to use high-power Ti:sapphire lasers as the source for supercontinuum generation. Figure 8.3 shows how the spectrum of an input pulse with a centre wavelength of approximately $800nm$ broadens over the length of the fibre to a bandwidth extending into the blue and mid-infrared regions, 400 to $1250nm$).

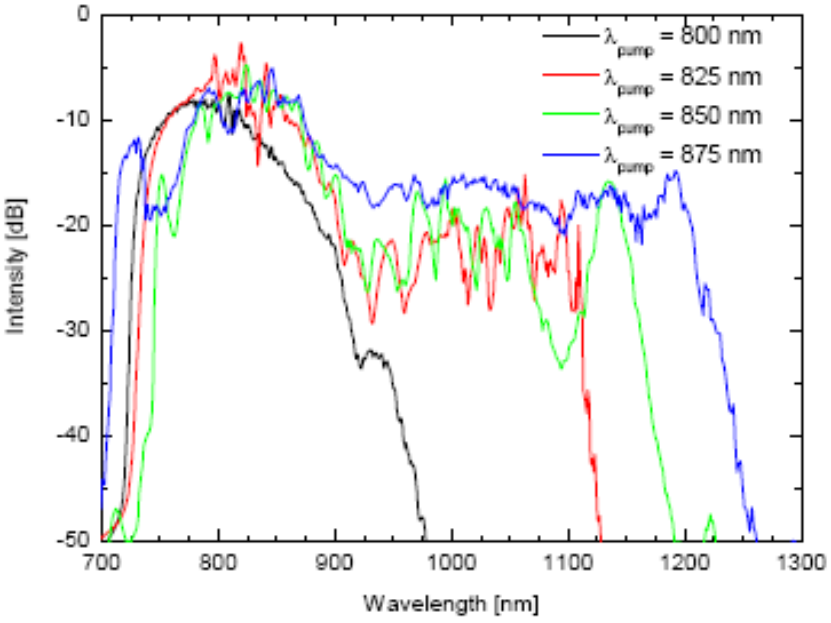

Figure 8.2: Spectra of supercontinuua generated by pumping with a femtosecond laser. As the pump wavelength moves towards the zero dispersion wavelength, the spectrum increases in bandwidth

Supercontinuum generation techniques have included the generation of submicron diameter fibres which shift the zero dispersion wavelength as far as $500nm$. This means that other sources can be used such as a low power microchip lasers operating at $532nm$ [85]. The use of cw lasers as pump sources have also been well documented [86]. Prahbu et al. have demonstrated how the integration of a Bragg grating can give extreme enhancement near the Bragg resonance wavelength [87]. It has also been demonstrated that irradiation of the fibre by UV light can be used to modify the refractive index and hence increase the waveguide dispersion thereby shifting the zero dispersion wavelength even further. It should be noted that supercontinuum generation is not restricted to the visible spectrum. There would be many potential applications for an broad infrared supercontinuum. One such application is in optical coherence tomography. As discussed in Chapter 2, sources in the infrared spectrum

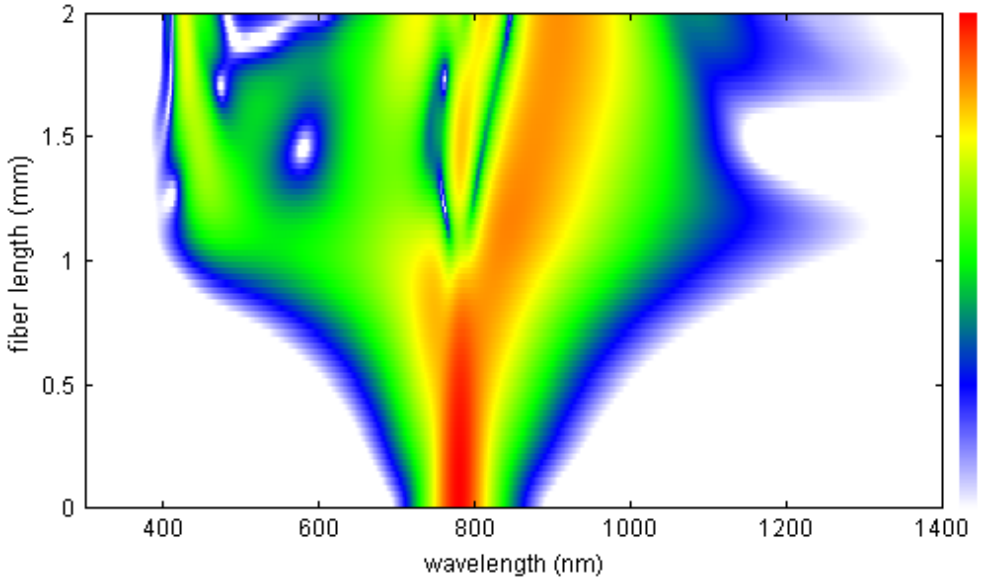

Figure 8.3: Intensity contour plot to illustrate how the spectral bandwidth (x-axis)of an infrared pulse broadens with increasing length of photonic crystal fibre (y-axis)[84]

give enhanced penetration of tissue but the resolution of OCT techniques is inversely proportional to the bandwidth of the laser. With the vast bandwidth of an IR supercontinuum can provide both high resolution and deep penetration. The output of the supercontinuum is dependent on the amount of pump light coupled into the fibre. The efficiency of the conversion from pump source to supercontinuum is enhanced by optimising and aligning the coupling of the laser beam into the photonic crystal fibre using an optical element such as a lens or microscope objective. To achieve optimum coupling, the pump source must be focussed into one end of the fibre. Equally, to enable the output to be used efficiently, another optical element is used to direct the beam as desired. The amount of intensity transferred successfully to the fibre from the laser source dictates the extent of the spectral broadening and hence the bandwidth of the output pulses. From this general overview of supercontinuum generation and its potential applications we shall now discuss the specific apparatus we used to generate the supercontinuum for use in subsequent experiments.

8.2 Supercontinuum generation experimental apparatus

Figure 8.4 shows a schematic of the experimental set-up used for a white light supercontinuum generation. For this work, the shortest pulses were required

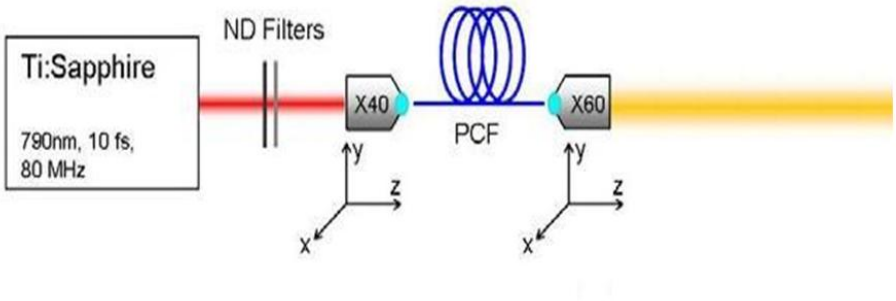

Figure 8.4: Schematic illustration of the experimental set-up for white-light supercontinuum generation. The 10 fs, 780 nm pulses from a Ti:sapphire is coupled in and out of the Femtowhite PCF using micrscope objectives mounted on XYZ-translation stages.

so the Femtosource Ti:sapphire laser as described in Chapter 6 was used. The pulse characteristics were measured and found to have a pulse duration of $10fs$ at $780nm$. The repetition rate of the cavity was approximately $80MHz$. To set up the apparatus, the output from the Ti:sapphire laser was raised using a series of mirrors to bring the height of the beam to $12.5cm$. The height of the beam was measured in the far distance to ensure that it remained at his height. The neutral density filters were used to reduce the power of the beam to approximately $60mW$. It was important to keep the average power below $120mW$ as extremely high peak powers can optically damage the PCF. Next, I placed a x40 objective within the beam path and using the XYZ-translation stage the objective was maneuvered so that the output from the laser remained

at the correct height. Next, the Femtowhite (NL-PM-750) PCF was placed in front of the objective. Again the, PCF was mounted on an XYZ-translation stage to permit fine positioning. Using a low-range power meter connected to an oscilloscope, I was able to finely adjust the positions of the objective and the PCF to maximise the IR output from the PCF. Eventually the coupling of the laser into the PCF was sufficient to initiate launch the supercontinuum. It was then possible to place the second microscope to couple the output of the PCF. I was then able to align and collimate the supercontinuum beam. The beam could then be manipulated as required by using mirrors or lenses. By using a prism I was able to view and image the spectrum of the supercontinuum. A photograph showing the spectral output I generated in the laboratory is shown in figure 8.5. As may be observed the intensity of the light generated across the spectrum is non-uniform as shown by the dips within the spectral range.

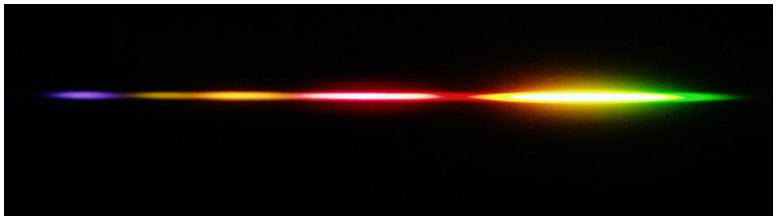

Figure 8.5: Image of supercontinuum spectrum generated by a dispersive prism

8.3 Experiments to characterise white-light Bessel beams

These experiments sought to investigate how the spatial and temporal coherence properties of a source influenced Bessel beam formation and the subsequent suitability in optical micro-manipulation. Generation of a monochromatic, temporally and spatially coherent Bessel beam had been demonstrated and investigated quite fully. Here, given the vast spectrum, the Bessel beam could be considered a superposition of hundreds of Bessel beams at successive and incremental wavelengths. Perhaps it could exhibit some other valuable characteristics. From the work carried out in the course of this research, it appears that the supercontinuum Bessel beam not only behaves as a superposition of monochromatic Bessel beams, but it also offers some benefits over a single wavelength Bessel beam of the same power.

Preceding research into Bessel beam generation was carried out by members of the research group using a variety of sources including cw lasers, femtosecond lasers, a supercontinuum source and even a halogen bulb[78]. From this, a simple theory of broad-bandwidth Bessel beams was developed and this will now be discussed.

8.3.1 Theory of white-light Bessel beams

The theory detailed in Chapter 4 was developed by Fischer et al. which could be used for Bessel beams generated by a broad bandwidth source. Here it is

proposed that the Bessel beam would have a central core encircled by number of rings, N_{rings} given by

$$N_{rings} \approx Integer\left(\frac{1.67(\Delta\omega_{FWMH}/\omega_0)^{-1} - 1/2}{2}\right) \tag{8.1}$$

where ω_{FWHM} is the source bandwidth and ω_0 is the centre wavelength. It follows that the number of rings will decrease as the bandwidth increases. Also the number of rings will decrease with centre wavelength ($\omega_0 = 2\pi c/\lambda$). We set about verifying this relationship in the experiments detailed in Section 8.3.2. The propagation distance, z_{max} of a Bessel beam is approximated by the ratio of the beam waist ω_0 to the angle of the cone of k vectors Ω. From this the propagation can be written as

$$z_{max}(\lambda) = \frac{\omega_0}{(n(\lambda) - 1)\gamma} \tag{8.2}$$

where γ is $(90 - \Omega/2)$. Figure 8.6 shows this relation plotted for a BK7 axicon with $\gamma = 1°$. It shows that the propagation distance should increase with wavelength. Consequently, in a supercontinuum, the shorter wavelengths will dominate the focal line closer to the axicon and slowly give way to the longer wavelengths as the propagation distance increases. As shown in figure 8.7 three discrete wavelengths λ_1, λ_2 and λ_3 will form Bessel beams at different points in space. We attempt to measure the propagation of a Bessel beam with wavelength in Section 8.3.3

Finally, let us consider the reconstruction properties of a supercontinuum beam. As set out in Chapter 4, the distance, z_{min} after which a Bessel beam starts to reform when the central core is blocked by an obstruction of radius r_{ob}

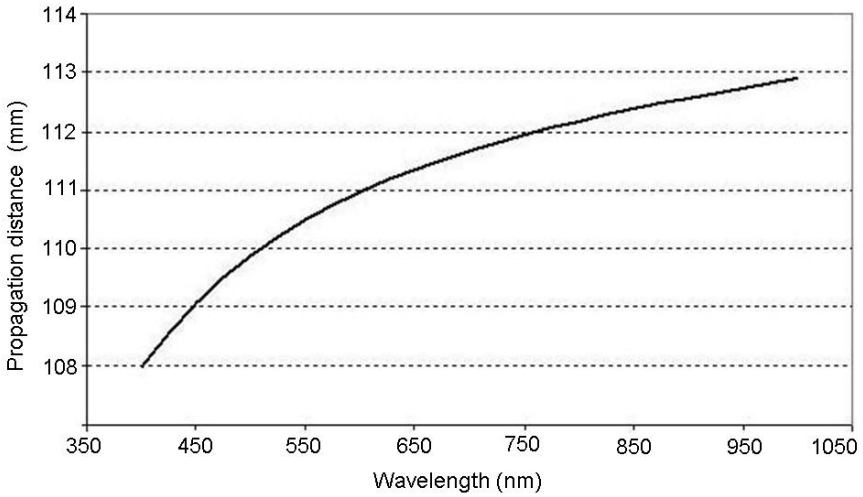

Figure 8.6: Theoretical propagation distance of the spectral components of a Bessel beam generated by a supercontinuum beam with a beam diameter of ω_0

is approximated by

$$z_{min} = r_{ob}\frac{k}{k_r} \tag{8.3}$$

This can be approximated by the relationship

$$z_{min}(\lambda) \approx \frac{r_{ob}}{(n(\lambda)-1)\gamma}$$

where γ is the apex angle of the axicon and $n(\lambda)$ is its wavelength-dependent refractive index. A plot of reconstruction distance around a $50\mu m$ obstacle against wavelength is shown in figure 8.8. In Section 8.3.4 we will set out to verify this relationship experimentally.

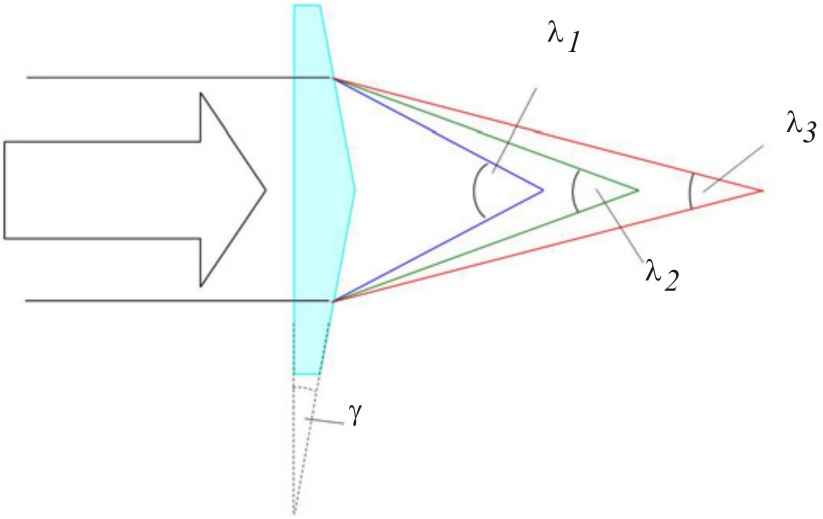

Figure 8.7: An axicon of angle γ will act to focus the wavelength λ_1, λ_2 and λ_3 at different points past the axicon

8.3.2 White-light Bessel beam profile

The cross-section of the Bessel beam is quite distinctive and, by now, familiar. This pattern is created by the interference pattern of the conical wavefronts generated by the optical element such as the axicon or spatial-light modulator. How would the coexistence of so many wavelengths affect this interference effect? Would the wavefronts combine to obliterate the core and ring structure? To investigate, this experiment entailed photographing the beam cross-sections at discrete wavelength intervals within the spectral range of the supercontinuum.

From the theory, it is understood that the point of maximum intensity for a Bessel beam is determined by the wavelength and size of the light incident on the axicon. In this experiment, that point would vary with the chosen tranche of wavelength. Furthermore, the intensity across the spectral range of the

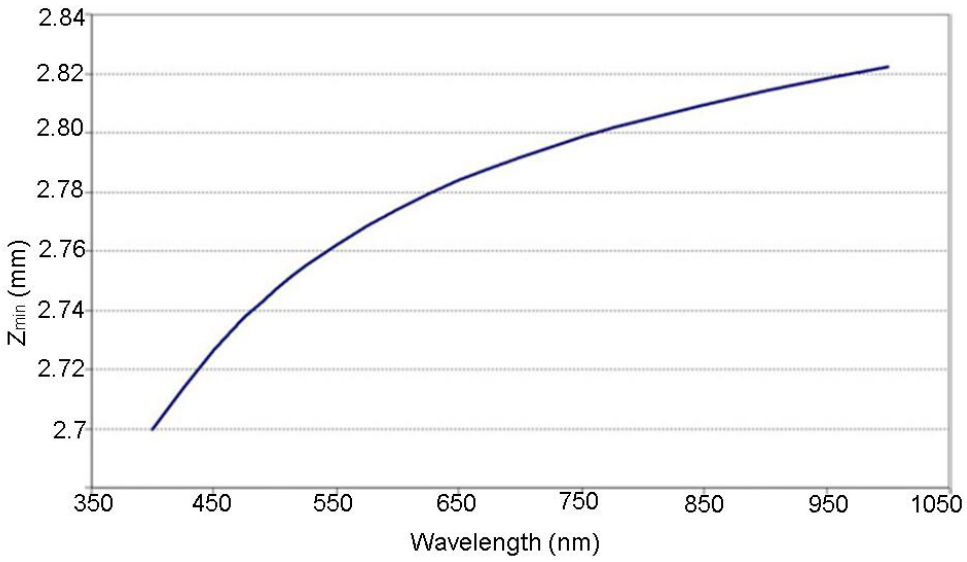

Figure 8.8: Plot showing wavelength dependent reconstruction distance after a spherical obstacle with a $50\mu m$ diameter. The Bessel beam is generated using an axicon with an opening angle of $1°$

supercontinuum is not uniform. For this reason, the photographs of the cross-section had to analysed with reference to a normalised intensity. Consequently, there was a wide variation in the resolution of the images. To illustrate how the diameters of the central spot and outer rings increase with wavelength figure 8.9 shows a selection of cross-section images at various discrete wavelengths within the spectral range of the supercontinuum. The image taken with no filtering shows that the Bessel beam is a superposition of the individual Bessel beams over the range of wavelengths.

For comparison, we plot the theoretical Bessel beam profile at the wavelengths $450nm$, $850nm$ and $1\mu m$ in figure 8.10. Now, by using National Instruments

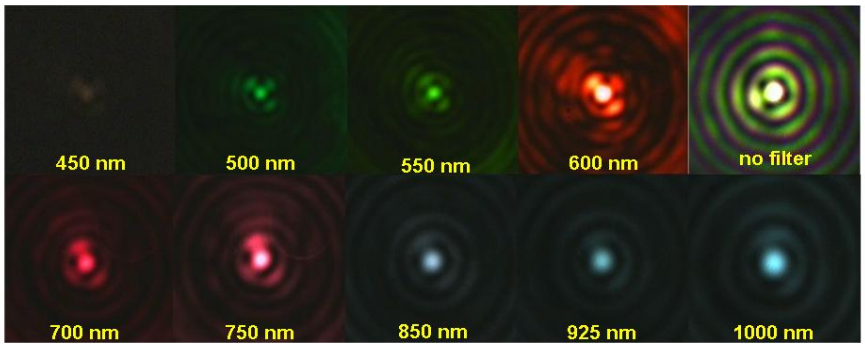

Figure 8.9: Photographs capturing the cross-sections of the white-light supercontinuum beam at various wavelengths within the spectral range as viewed through interference filters ranging from $450nm$ to 1micron

IMAQ and Mathcad software packages, to take line profiles from these images I was able to map the Bessel beam cross-section to the theoretical profiles. Figure 8.11 shows profiles taken from images at the different wavelengths with a best fit line. Here there is evidence of the variation in spectral intensity along the supercontinuum profile. In fact, some images were saturated within the central spot area. That aside, the plots show good agreement between the captured Bessel beam profiles and those derived from theory.

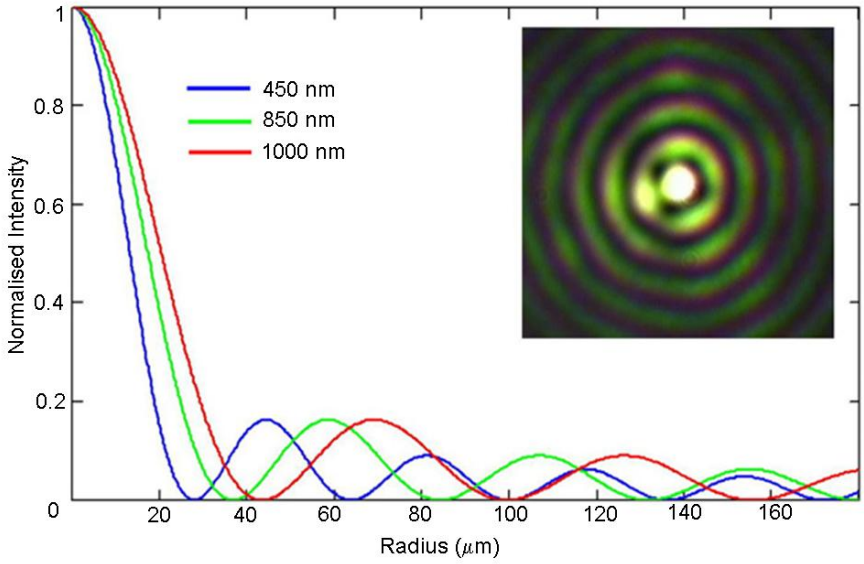

Figure 8.10: Plot to show the theoretical cross-section profiles of a Bessel beam at 450, 850 & 1000 nm as expected by theory

8.3.3 White-light Bessel beam propagation

The next stage of characterisation was to investigate the longitudinal propagation of the supercontinuum Bessel beam. Again, this was done by analysing cross-section images captured using a CCD camera.

First, the experiment aimed to measure the propagation distance of the Bessel beam as a function of wavelength. This was done by inserting each interference filter in turn. A transverse image of the Bessel beam was captured using a Watec CCD camera which could be translated on a XY-translation translation stage. Images were captured at 10 micron intervals along the longitudinal axis of the Bessel beam. A line profile bisecting the Bessel central spot gave a

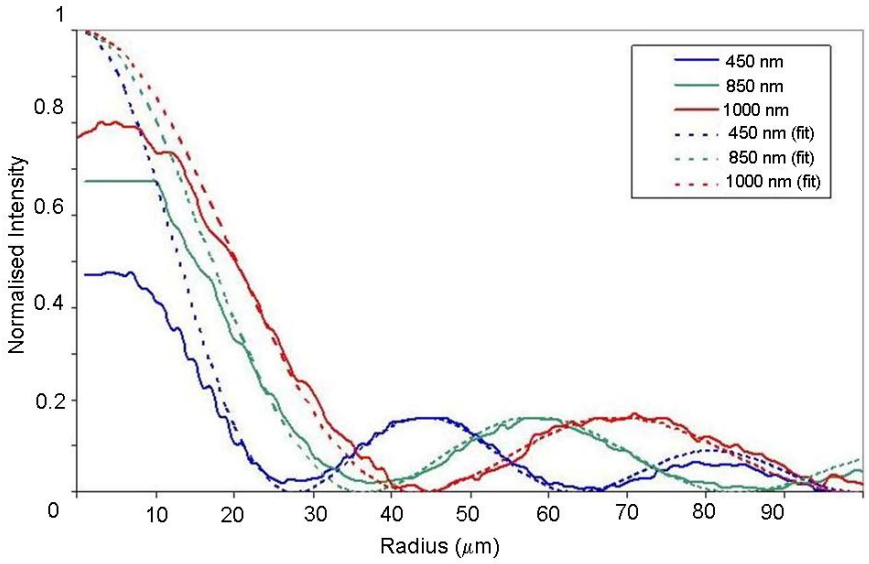

Figure 8.11: Plot to show the experimental cross-section profiles of a Bessel beam at 450, 850 and 1000 nm as measured using a CCD camera and interference filters

succession of line profiles which were normalised and compiled using MathCad into a representation of the beam profile as shown in figure 8.12. From this work, measurements of the propagation distances of the Bessel beam at various wavelengths could be made. This laborious approach gave some encouraging results at first. The number of images involved in this work exceeded $10,000$.

Again, variation in intensity over the spectral range of the supercontinuum meant analysis of the data proved difficult. I used MathCad to compile contour plots from the line profiles along the line of propagation. One such contour plot is shown in figure 8.13. The image suggests that the propagation of the Bessel beam starts closer to the axicon for the shorter wavelengths as expected. However, when compared to a contour plot generated from renormalised line profiles, that assertion no longer seems valid. The next experiment was to

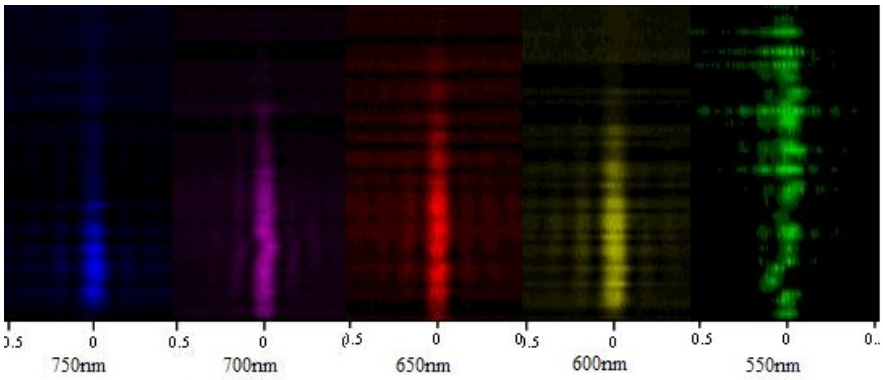

Figure 8.12: Examples of profiles obtained using line profiles from cross-section images of beam

investigate the reconstructive properties of a supercontinuum Bessel beam. We will discuss this now.

8.3.4 White-light Bessel beam reconstruction distance

Having characterised the profile and the propagation distance, the next task was to measure the reconstruction distance of each colour within a white light Bessel beam as it reforms behind an object. As detailed earlier in this chapter the reconstruction distance of a Bessel beam is dependent on the wavelength-dependent refractive index of the axicon. This was plotted for a BK7 axicon in figure 8.8 which shows that the reconstruction distance should increase with with wavelength.

To verify this I needed a circular obstacle. Creation of a suitable obstacle was difficult. In previous work carried out by the group, the scale dictated that small spheres or pen dots could be used. I attempted to carry out this

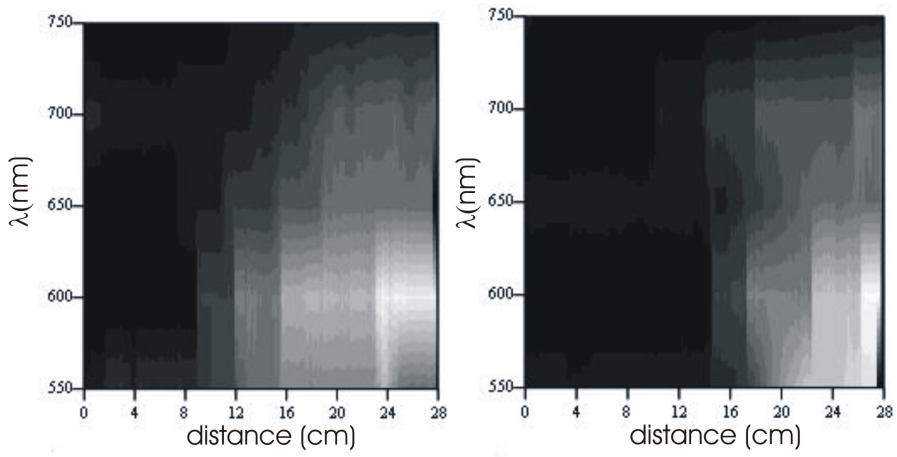

Figure 8.13: Contour maps generated by MathCad to show how the propagation distance of the Bessel beam varies with wavelengths between 500 and 750 nm unnormalised(l), normalised(r)

experiment using tiny pen dots as the object. The shape of these obstacles were not uniform and therefore an alternative obstacle was required. One was created by Steve Neale who deposited gold atoms onto a glass slide using a 50 micron mask. To measure the diameter of the obstacle, the beam was imaged with a graticule replacing the obstacle as shown in figure 8.14. This shows

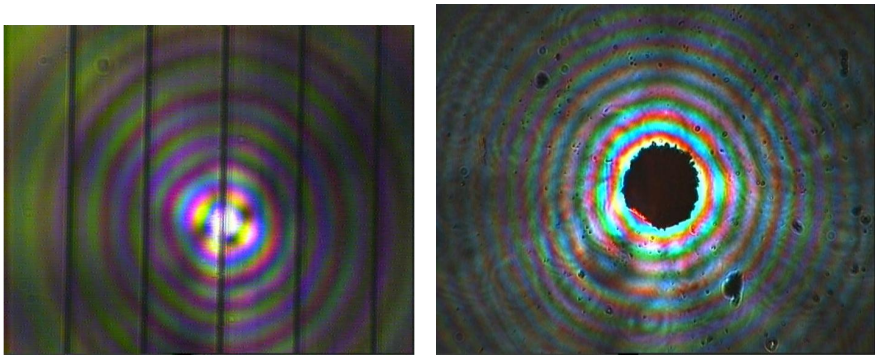

Figure 8.14: Image shows the how the obstacle (r) was measured by first imaging a graticule (l) and then the obstacle (r) placed in the same plane.

both the supercontinuum Bessel beam profile and the obstacle. By knowing the dimensions of the graticule the obstacle was imaged and measured using IMAQ software as having a diameter of $49.6\mu m \pm 0.5\mu m$. From this the theoretical

reconstruction distance could be calculated and this is shown in figure 8.15 Following good practice, the obstacle was placed at a suitable distance from

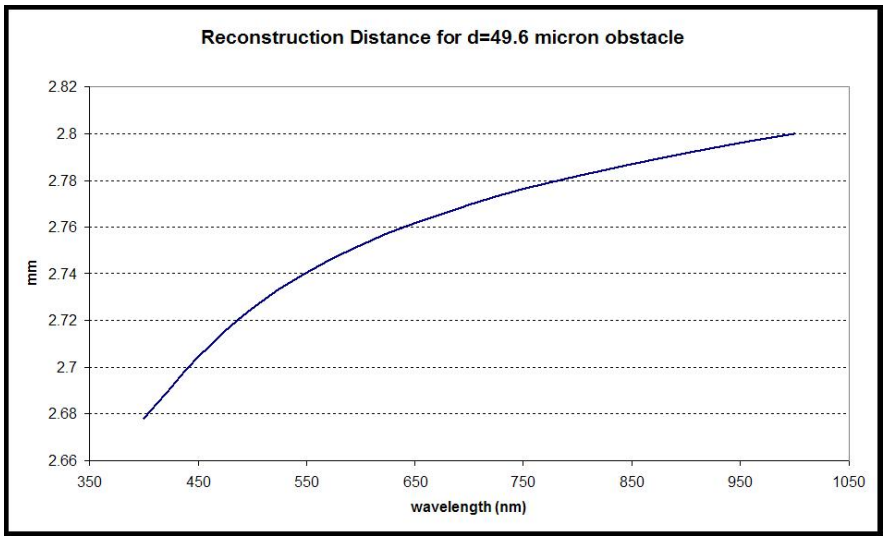

Figure 8.15: Plot shows the theoretical reconstruction distance of a Bessel beam as a function of radiation wavelength

the axicon which was measured to be approximately $5cm$. First, the CCD camera was mounted on an XY translation stage which had a resolution of $10\mu m$. Thousands of images were captured at discrete interval along the beam propagation at each wavelength. As in the propagation distance experiment, line profiles bisecting the Bessel central spot were taken and compiled using MathCad into a representation of the beam profile. It was hoped that the labour would result in a determination of the reconstruction distance. A comparison of the reconstruction distance at 400 nm with that at 850 nm is shown in figure 8.16.

In this image, the reconstruction distance of the $850nm$ wavelength beam appears to be shorter than that of the $400nm$. However, the resolution of the images captured at the longer wavelength is superior. This variation in resolu-

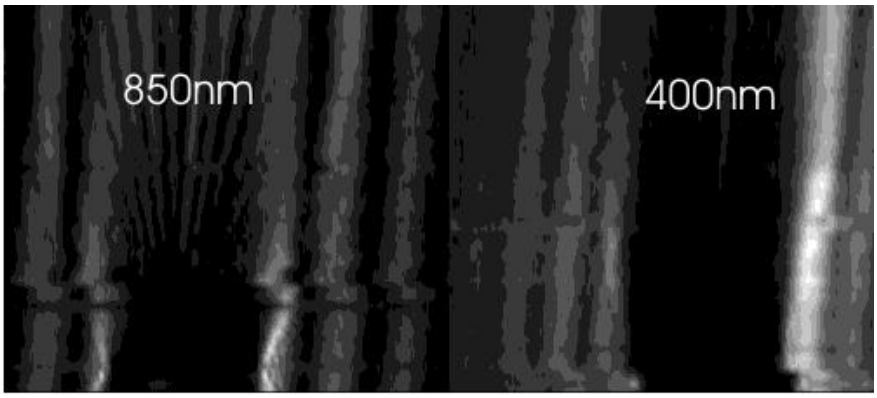

Figure 8.16: Images generated to show how the profile of a Bessel beam reconstructs after an object at two wavelengths (a) $850nm$ and (b) $400nm$

tion and spectral intensity obfuscates the underlying results. In an alternative method, I extracted the line profiles into an excel spreadsheet where the values were renormalised. A plot showing the reconstruction distances after an obstacle for wavelengths 450, 650 and $850nm$ is shown in figure 8.17. From this the reconstruction distances could be estimated. The resolution issues introduce errors and furthermore hysteresis in the equipment and fluctuations in the illumination meant that the errors associated with these measurements were large. An alternative method was sought.

According to the theory, the change in reconstruction distance over the 400 to $1000nm$ range was expected to take place within $40nm$. An alternative approach involved visually determining the point at which reconstruction of the spot was deemed to occur. However, while the eye is very good at detection rapid movement but it is not the best tool for observing gradual changes in patterns. After many attempts to determine the point of reconstruction this way, I measured the point at which the spot began to appear and the point at which translating the stage did not seem to affect the change of size or intensity of the central spot. An interpolation gave a measurement of the reconstruction point. The

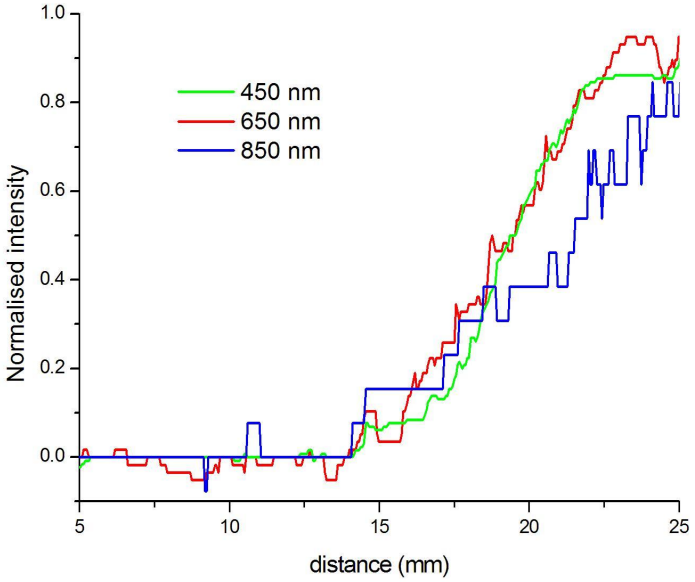

Figure 8.17: Plot of reconstruction distance after obstacle for beams at 450, 650 and 850nm.

results of this method are shown in figure 8.18.

While there was good agreement of the measurements and the theory, again this method contained significant reading errors. For successful publication a better experimental method was required.

In a repeat of the experiment, this time the CCD camera was mounted on an XYZ-translation stage which was computer controlled in the axis parallel to beam propagation as depicted in figure 8.19. Wavelength selection was made by using a suite of COMAR interference filters. Neutral density filters were used to prevent saturation of the camera. Photographs were initially taken at $10\mu m$ intervals along the axis of beam propagation. At the end of each run, the camera was returned to the starting point to determine if there was any

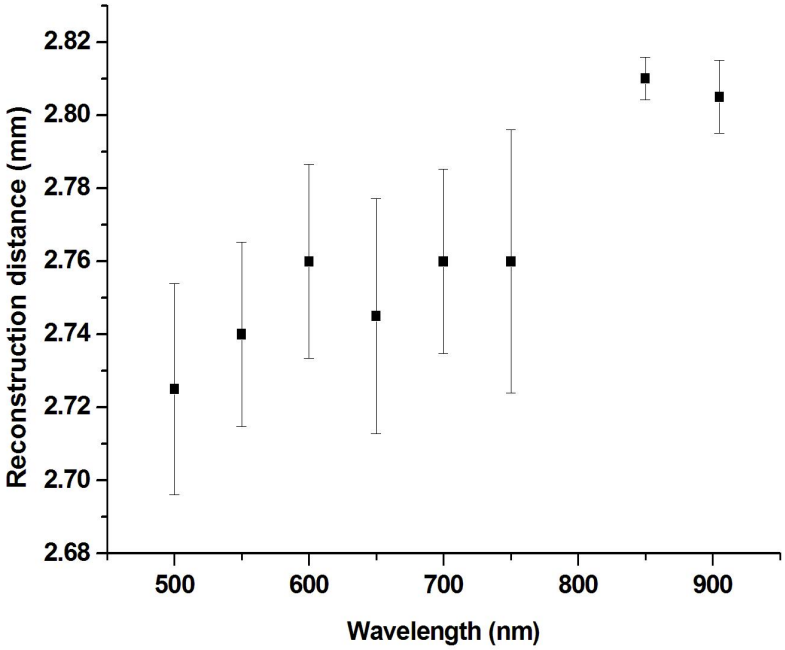

Figure 8.18: Plot showing the reconstruction distances around a 49.6 micron object as a function of wavelength. These measurements were made by an interpolation method and has large errors associated with the readings.

significant hysteresis error arising during the experiment. None was observed.

Initially the experiment was carried out along the range of 0 to $3mm$ for the $650nm$ wavelength. The images were analysed and collated into an excel spreadsheet. A plot showed that the reconstruction appeared to occur in the region of 2.6 to $2.7mm$. This was determined by the fact that the central spot ceased to increase in size between these two points. This permitted the experiment to be repeated in the region of 2.65 to $2.83mm$ but at a higher resolution of $1\mu m$ intervals. Again the experiment was repeated 3 times for each wavelength. This method proved to be far more profitable. Each set of images was analysed

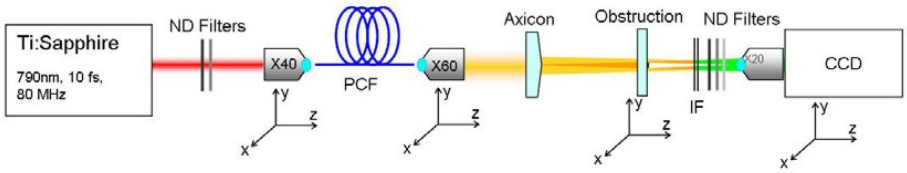

Figure 8.19: Schematic of experimental apparatus used for imaging the reconstruction of a supercontinuum Bessel beam around a circular obstacle. Interference filters are used to select the wavelength.

as in the previous experiments, however, the higher resolution allowed a determination of where the central spot had reconstructed. The limiting factor in these measurements was no longer human error but the camera resolution. It followed therefore that at the longer wavelengths which have larger central spots, the measurement error was reduced. The results are shown in figure 8.20. From the theory in chapter 4 and the experimental results just discussed,

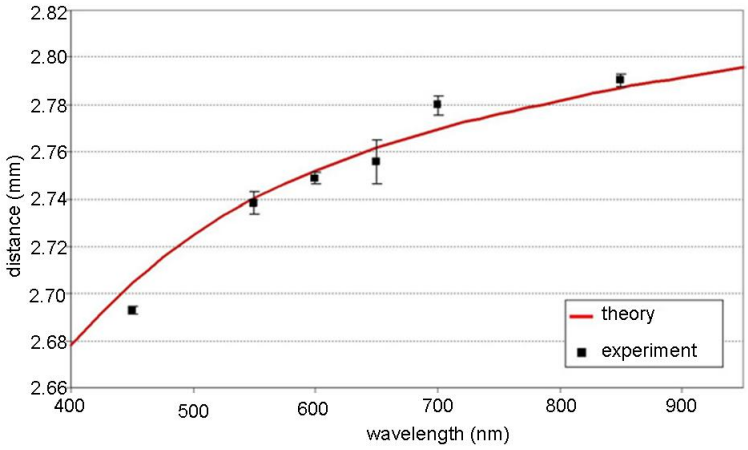

Figure 8.20: Plot shows the experimental reconstruction distance (mm) of a Bessel beam after an $49.7\mu m$obstacle at discrete wavelengths in the supercontinuum spectral bandwidth $400nm$ to $1000nm$)

it is clear that the expectation is that the shorter wavelengths would reform as

a Bessel a beam earlier than the longer wavelengths. Thus, a blue central spot should be visible prior to the addition of other colours with distance to form a visible white central spot. Similarly, the shorter wavelengths will disappear before the longer wavelengths leaving a red and infra-red tail to the central spot. Figure 8.21 shows the cross sections of the beam along the central axis with no spectrum filtering which reinforces the experimental result above.

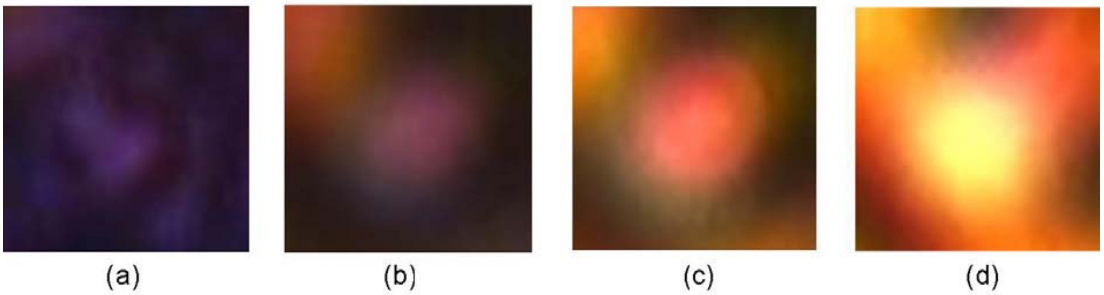

Figure 8.21: Images of the white-light Bessel beam showing the formation central spot at the of start of the beam propagation. The development of the central spot from blue to white shows that the Bessel beam forms with the shorter wavelength light first.

Another image shown in figure 8.22 was captured with a degree of neutral density filtering shows the spectral variation around the central white spot. The

Figure 8.22: Image of central spot of a white light Bessel beam as generated by a supercontinuum source. The white central core is encircled by a spectrum which shows that the longer wavelengths have a larger spot size.

experiments carried out in the preceding sections verifies that the Bessel beams generated by a supercontinuum source do in fact behave like a superposition of monochromatic Bessel beams at incremental wavelength steps. In the final experiment, we will look at the possibilities of guiding within a supercontinuum beam.

8.4 Experiments in optical guiding using white-light Bessel beams

After the reconstruction work was completed, the supercontinuum source was aligned to a guiding apparatus to perform some final guiding experiments. The aim of these experiments was to identify any benefits to be gained from using the supercontinuum source compared to a femtosecond or cw laser. The beam diameters of both the Ti:sapphire pump laser and supercontinuum were measured again using the BeamMaster and the apparatus was set up as shown in figure 8.23. The output from the Femtosource laser can be directed by a flipper mirror to two set-ups. The first is a supercontinuum guiding set-up. The Ti:sapphire beam with a diameter of $2mm$ was aligned and coupled into the PCF using the microscope objective. By adjusting the XY-translation stages, the output could be optimised to give the a broad spectral output. I optimised the output from the PCF which had a diamater of $2.5mm$, collimated and directed the beam through a $\times 4$ telescope. A flipper mount was used to redirect the output from the Ti:sapphire laser through a separate $\times 5$ telescope. This ensured that that beam diameters were approximately $10mm$ in both cases. Guiding experiments were carried out using in turn, a $25mm$ lens, $50mm$ lens and a 1°

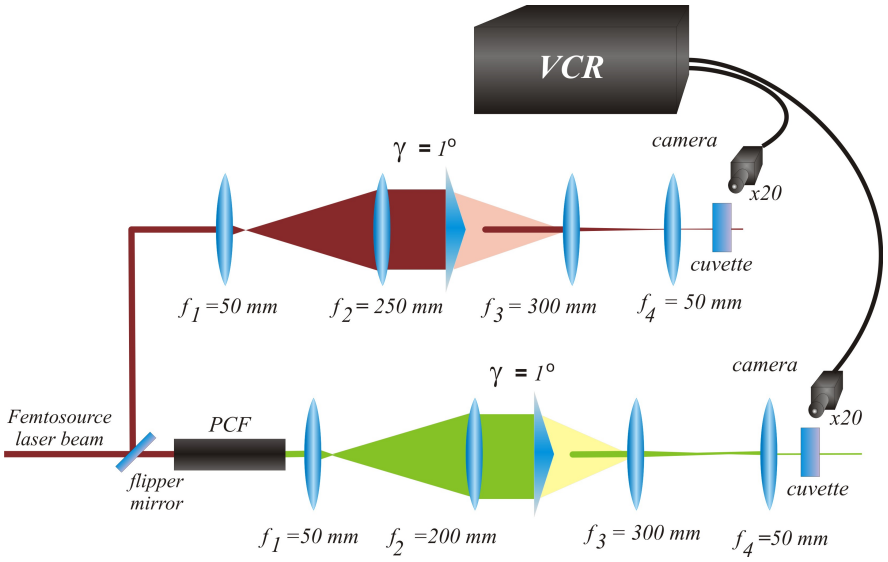

Figure 8.23: Experimental spparatus for comparison of supercontinuum and femtosecond guiding. Two setups were arranged in parallel to generate the same size Bessel beams. In the femtosecond setup, the magnifying telescope is $1:5$ while the supercontinuum beam is expanded by a $1:4$ telescope

axicon. Guiding velocities were measured for a range of output powers using each of the lenses with the results shown in table 8.2. The main observation

Supercontinuum Power (mW)	**Velocity ($\mu m/s$) 25mm lens**	**Velocity ($\mu m/s$) 50 mm lens**
100	48	32
80	45.7	18.8
60	25	13.9
40	16	8

Table 8.1: Table shows the mean guiding velocities of 10 $2.3\mu m$ particles at various powers using a supercontinuum source focussed through (i) 25 mm lens and (ii) 50 mm lens

was that the particles seemed to be guided at much higher velocities than for the femtosecond or cw Ti:sapphire beams. To compare, the guiding velocities were measured for the femtosecond beam as detailed in table **??**. It was not possible to guide well with femtosecond average powers of less than $100mW$. Equally, it was not possible to extract more than $100mW$ of supercontinuum

average power at the cuvette.

Power(mW)	Velocity microns/second
450	42
400	40
350	32
300	26
250	18
200	13
150	10

Table 8.2: Table shows the guiding velocities of $2.3\mu m$ at various powers using a $10fs$ femtosecond Ti:sapphire laser

Power(mW)	Velocity microns/second
100	48
80	46
60	25
40	16

Table 8.3: Table shows the guiding velocities of $2.3\mu m$ at various powers using a supercontinuum source

From this we see that optical guiding is possible not only at lower powers when using a supercontinuum Bessel beam, but also at increased velocities. It can be seen that the guiding velocities can be achieved for approximately a quarter of the equivalent power from the femtosecond laser. To compare guiding distances figure 8.24 show composite images taken by the CCD camera along the length of the cuvette for the same power (100 mW). Here we can see that the supercontinuum offers extended guiding distances compared to the femtosecond beam. Also evident was that the scattered light from the particles showed a spectral change over the propagation distance from blue through green and yellow to red. If one recalls that the Bessel beam generated by the supercontinuum can be considered as a superposition of Bessel beams generated of a continuum of wavelengths then the extended guiding properties are easily

understood. The next logical hypothesis is that the greater the bandwidth of the supercontinuum output, the greater the propagation distance of the Bessel beam. It follows therefore, that the effect should be discernible in an experiment which compares the guiding of particles with a broad bandwidth femtosecond laser and a cw laser of the same central wavelength. As detailed in Chapter 5, this was indeed the case. This work strongly suggested that the it would be

Figure 8.24: The relative guiding distances of $2.3\mu m$ polymer spheres in a $100mW$ average power (i) supercontinuum beam and (ii) a femtosecond Ti:sapphire beam are shown

possible to achieve super-extended guiding distances result. This result helped to explain some observations made in the work described in Chapter 6. The broader bandwidth of the femtosecond laser permitted stronger confinement and marginally longer guiding distances. Here, with a much larger spectral bandwidth the effect is much more evident. I repeated the experiment but to compare femtosecond with cw guiding using this Femtosource and we can see in figure 6.21 that the extended guiding effect is detectable here, if not in the previous experiments. The images show the comparative guiding distances for a range of powers using $2.3\mu m$ polymer spheres over the length of the cuvette, d.

While I was unable to complete this work, it generated interest in exploring

broad bandwidth lasers to achieve enhanced optical guiding distances. In related work, it was shown that by exploiting the broad bandwidth of the super-continuum, it is possible to achieve enhanced optical guiding distances using Gaussian beams [88]. In fact, guiding distances with Gaussian beams were found to be comparable with Bessel beams. This can be explained by the extended line of focus which was modelled by Pascal Fisher and Antonia Carruthers and is shown in 8.25. Here the extended distances usually associated

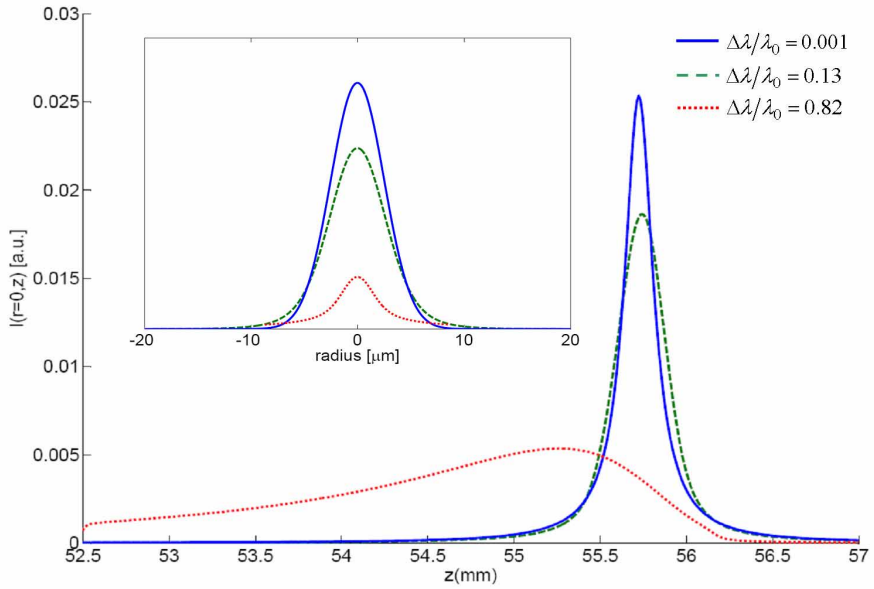

Figure 8.25: Plot which shows the modelling of the intensity of a Gaussian beam focussed by a lens for 3 different bandwidths. The broadband white-light beam may be seen to have an extended line of focus which can be used for extended guiding applications

with Bessel beams are produced with Gaussian beams and contain the higher powers associated with Gaussian beams.

8.5 Discussion

In the course of the work detailed within this chapter which explored the generation and properties of white-light Bessel beams there were several positive outcomes.

- A white-light Bessel beam was generated using a supercontinuum source. Uusing using ultrashort pulses to induce nonlinear effects in a photonic crystal fibre, a broadband output was incident on an axicon to produce a Bessel beam. Key to this Bessel beam generation is the spatial coherence of the incident white light from the supercontinuum.

- The Bessel beam was fully characterised in terms of its wavelength-dependent transverse profile, propagation and self-healing properties and was found to behave like a superposition of Bessel beams at a range of wavelengths.

- Initial experiments in optical guiding showed an increase in optical guiding distances for white-light Bessel beams compared to their femtosecond and cw counterparts. This extended guiding distance is as a consequence of the extremely broad bandwidth of the supercontinuum source. This acts to extend the focal line of the beam.

This work proved to be very interesting and exciting. By this point, I had improved my theoretical understanding of optical guiding and my experimen-

tal techniques. By virtue of my earlier experiments, I was able to carry these experiments out more accurately and speedily. I gained an understanding of supercontinuum generation and experience of aligning and optimisation the photonic crystal fibre and optics for efficient supercontinuum generation. Most importantly however, I had by this point understood that the key to scientific research is accurate measurement. While many of the phenomena investigated in this chapter may appear intuitive the verification of the physics had to be experimentally proved. Pivotal in accurate measurement is the equipment and techniques used. The early attempts showed that with standard XYZ-translation stages it was unrealistic to expect to accurately measure to the micron scale. Hysteresis and misalignments introduced massive uncertainties which rendered analysis of the results inconclusive. After completing my three year research period, I returned to repeat and improve the experiment as it was hoped that the results could form part of a publication. This time I knew that I would require much better methods and equipment. Using a computer-controlled translation stage I was able to make measurements with much higher confidence and accuracy. The speed of the technique also allowed me to take more measurements more quickly. From this I was able to reduce the uncertainty in the measurements. In the course of the white-light Bessel beam work I captured and analysed over 20,000 images. This meant that while the experiments themselves may only take a matter of days, the majority of the time was spent in extracting information from these images. My aspiration was to build accurate 3-dimensional interpretations of the reconstruction distances and Bessel beam profiles. For this I looked into obtaining software that was able to consolidate the 2-dimensional images into a 3-dimensional composition. These are readily used by biologists working in microscopy experiments. However, the cost and operating requirements of the software could not justify

the benefits.

CHAPTER 9

Conclusions & further work

As stated at the start of this thesis, the aim of the work was to explore the use of ultrashort-pulsed lasers in multiphoton excitation and optical guiding with non-Gaussian beams. Here, at its conclusion we shall discuss to what extent this aim has been successfully achieved.

In the first experiment the aim was to determine whether the high-peak powers of ultrashort lasers could yield benefits in the optical guiding of particles within a beam. We demonstrated that the particles were guided at comparable velocities in femtosecond and cw laser beams. This result applied to both guiding in Bessel and Gaussian beams.

We also demonstrated that while the guiding velocities were comparable, it was possible to use the high-peak powers to exploit multi-photon excitation in materials. Furthermore, a successful demonstration of the simultaneous second-harmonic generation and optical guiding in a Bessel beam was performed.

This work led to the use of ultrashort-pulsed lasers in visualisation techniques. The two-photon excitation-induced fluorescence from fluorescein allowed the properties of beams to be imaged. We saw that the Bessel beam had a self-healing property that the Gaussian beam lacked. From these images the reconstruction distance of a Bessel beam around an object was found to be in good agreement with the theory. This effect has been developed as a means for visualisation in optical binding studies. It has also been used as a means for mapping the profile of ultrashort pulses.

The next experiments aimed to explore multi-photon excitation through turbid media using Bessel beams. This work was compromised by a flawed experimental approach. A different experimental approach would have yielded better and more conclusive quantitative results. However, we successfully demonstrated qualitatively, that the self-healing properties of a Bessel beam facilitated penetration through turbid media for multi-photon excitation.

Finally, using spatially coherent broadband white-light sources, successful demonstration of white-light Bessel beam generation was performed using an axicon. This white-light Bessel beam was characterised in terms of its profile, propagation and self-healing properties and found to be consistent with the wavelength-dependent theory of Bessel beams. More importantly, initial experiments in optical guiding using this supercontinuum source indicated that extended guiding distances could be obtained by exploiting the broadband spectrum of the laser. Revisiting earlier experiments using a femtosecond laser with a broader bandwidth and shorter pulses confirmed to me that the bandwidth of the source contributed to extend the focal line of a beam.

From this work, I would like to have been able to carry out further experiments using the supercontinuum source. If it was possible to extend the guiding distance of a beam by using a source with a broader spectral bandwidth, it would have been interesting to see whether Gaussian beams could be used for optical guiding over longer distances in this way. As it transpired this work was carried out by others after I had completed my research in the group. The results, as mentioned in Chapter 8, show that broadband white-light Gaussian beams can have guiding distances comparable to Bessel beams. The added benefit of the Gaussian beam is that the power will be used for guiding and not distributed over the entire structure as in a Bessel beam.

To summarise, we have explored quite thoroughly the use of ultrashort pulses in multiphoton excitation and optical guiding and achieved some good results. For me, one of the most interesting outcomes lies in the extended guiding distances of white-light beams. For years, the Bessel beam has been the beam of choice for optical guiding over larger distances. For the first time, we see here that the spectral properties of a beam can be used to make Gaussian beam the preferred option.

References

[1] http://www.esf.org/publication/119/ultra.pdf.

[2] T.H. Maiman. Stimulated optical emission in ruby. *Nature*, 187:493, 1960.

[3] D.G. Grier. A revolution in optical manipulation. *Nature*, 424:810–816, 2003.

[4] D. McGloin. Optical tweezers: 20 years on. *Philosophical Transactions of the Royal Society A*, 364:3521–3537, 2006.

[5] Anthony E. Siegman. *Lasers*. University Science Books, 7th edition, 1990.

[6] Paras N. Prasad. *Introduction to Biophotonics*. Wiley-Interscience, 2003.

[7] B. Agate, B. Stormont, A.J. Kemp, C.T.A. Brown, U. Keller, and W. Sibbett. Simplified cavity designs for efficient and compact femtosecond cr:lisaf lasers. *Optics Communications*, 205:207–213, 2002.

[8] J. Kutz, B. Collings, B. Bergman, S. Tsuda, S. Cundiff, W. Knox, P. Holmes,

and M. Weinstein. Modelocking pulse dynamics in a fiber laser with a saturable bragg reflector. *Journal of the Optical Society of America B*, 14:2681–2690, 1997.

[9] P. Dufour, M. Piche, Y. De Kononinck, and N. McCarthy. Two-photon excitation fluorescence microscopy with a high depth of field using an axicon. *Applied Optics*, 45:9246–9252, 2006.

[10] D.E. Spence, P.N. Kean, and W. Sibbett. 60-fsec pulse generation from a self-mode-locked ti:sapphire laser. *Optics Letters*, 16:42, 1991.

[11] A. Ashkin and J.M. Dziedzic. Observation of radiation pressure trapping of particles by alternating laser beams. *Physical Review Letters*, 54:1245–1248, 1985.

[12] A. Ashkin, J.M. Dziedzic, J.E. Bjorkholm, and S. Chu. Observation of a single-beam gradient force optical trap for dielectric particles. *Optics Letters*, 11:288–290, 1986.

[13] W. Tao, J. Wilkinson, E. Stanbridge, and M.W. Berns. Direct gene transfer into human cultured cells facilitated by laser micropuncture of the cell membrane. *Proceedings of National Academy of Science, USA*, 84:4180–4184, 1987.

[14] J.E. Molloy, K. Dholakia, and M.J. Padgett. Optical tweezers in a new

light. *Journal of Modern Optics*, 50:1501–1507, 2003.

[15] J.E. Molloy and M. Padgett. Light, action: optical tweezers. *Contemporary Physics*, 43:241–258, 2002.

[16] Claude Rulliere. *Femtosecond Laser Pulses: Principles and Experiments (Hardcover)*. Springer-Verlag Berlin and Heidelberg GmbH & Co. K, 1998.

[17] R. W. Boyd. *Nonlinear Optics*. Academic San Diego, 1992.

[18] A. Yusim, J. Barsalou, D. Gapontsev, N. S. Platonov, O. Shkurikhin, V. P. Gapontsev, Y. A. Barannikov, and F. V. Shcherbina. 100 watt single-mode CW linearly polarized all-fiber format $1.56 - \mu m$ laser with suppression of parasitic lasing effects. In L. N. Durvasula, A. J. W. Brown, and J. Nilsson, editors, *Fiber Lasers II: Technology, Systems, and Applications. Edited by Durvasula, L. N.; Brown, Andrew J. W.; Nilsson, Johan. Proceedings of the SPIE, Volume 5709, pp. 69-77 (2005).*, pages 69–77, April 2005.

[19] W.F. Cheong, S.A. Prahl, and A.J. Welch. A review of the optical properties of biological tissues. *IEEE Journal of Quantum Electronics*, 26(12):2166–2185, 1990.

[20] Valery V. Tuchin. *Handbook of Optical Biomedical Diagnostics*. SPIE-International Society for Optical Engineering, 2003.

[21] R. K. Wang and V. V. Tuchin. Enhance light penetration in tissue for high-resolution optical imaging techniques by the use of biocompatible chemical agents. *Proceedings of the SPIE*, 4596:314–319, July 2003.

[22] P. Tadrous. Methods for imaging the structure and functions of living tissues and cells: fluorescence lifetime imaging. *Journal of Pathology*, 191:229–234, 2000.

[23] P.I.H Bastiaens and A. Squire. Fluorescence lifetime imaging microscopy: spatial resolution of biochemical processes in the cell. *Trends in Cell Biology*, 9:48–52, 1999.

[24] J.D. Bhawalkar, N.D. Kumar, C.F. Zhao, and P.N. Prasad. Two-photon photodynamic therapy. *Journal of Clinical Lasers Medicine and Surgery.*, 15:201–204, 1997.

[25] U.K. Tirlapur, K. Konig, C. Peuckert, R. Krieg, and K.J. Halbhuber. Femto-second near-infrared laser pulses elicit generation of reactive oxygen species in mammalian cells leading to apoptosis-like death. *Experimental Cell Research*, 263:88–97, 2001.

[26] K. Konig. Multiphoton microscopy in life sciences. *Journal of Microscopy*, 200:83–104, 2000.

[27] M. Göppert-Mayer. über elementarake mit zwei quantensprungen. *Annals*

of Physics (Leipzig), 5:273–294, 1931.

[28] W. Denk. Multiphoton microscopy: Imaging with nonlinear optics. *Photonics Spectra*, 31:125, 1997.

[29] W. Kaiser and C.G B. Garrett. Two-photon excitation in caf_2: eu^{2+}. *Physical Review Letters*, 7(6):229–231, Sep 1961.

[30] W. Denk and F. Helmchen. Deep tissue two-photon microscopy. *Nature Methods*, 2:932 – 940, 2005.

[31] P. A. Franken, A. E. Hill, C. W. Peters, and G. Weinreich. Generation of optical harmonics. *Phys. Rev. Lett.*, 7(4):118–119, Aug 1961.

[32] http://www.rp-photonics.com/phase_matching.html.

[33] http://phys.strath.ac.uk/12-370/sld029.htm.

[34] L. Moreaux, O. Sandre, O. M. Blanchard-Desce, and J. Mertz. Membrane imaging by simultaneous second-harmonic generation and two-photon microscopy. *Opt. Lett.*, 25:320–322, 2000.

[35] L. Moreaux, O. Sandre, and J. Mertz. Membrane imaging by second-harmonic generation microscopy. *Journal of Optical Society of America B*, 17:1685–1694, 2000.

[36] J. Mertz and L. Moreaux. Second harmonic generation by focused excitation of inhomogeneously distributed scatterers. *Optics Communications*, 196:325–330, 2001.

[37] K.T. McDonald. Laser tweezers. *American Jounal of Physics*, 68:486, 2000.

[38] D. White. Vector finite element modeling of optical tweezers. *Computer Physics Communications*, 128:558–564, 2000.

[39] A. Ashkin, J.M. Dziedzic, and T. Yamane. Optical trapping and manipulation of single cells using infrared laser beams. *Nature*, 330:769–771, 1987.

[40] A. Ashkin. Forces of a single-beam gradient laser trap on a dielectric sphere in the ray optics regime. *Biophysics Journal*, 61:569–582, 1992.

[41] M.C. McDonald, G. Spalding, and K. Dholakia. Microfluidic sorting in an optical lattice. *Nature*, 426:421, 2003.

[42] L. Paterson, M.B. Agate, M. Comrie, R. Ferguson, T.K. Lake, J.E. Morris, A.E. Carruthers, C.T.A. Brown, W. Sibbet, P.E. Bryant, F. Gunn-Moore, A.C. Riches, and K. Dholakia. Photoporation and cell transfection using a violet diode laser. *Optics Express*, 13:595–600, 2005.

[43] V. Garbin, D. Cojoc, R. Kulkarni, R. Malureanu, E. Ferrari, M. Nadasan, and E. Di Fabrizio. Numerical analysis of forces in optical tweezers in the rayleigh regime. *Advanced Topics in Optoelectronics, Microelectronics, and Nanotechnologies II. Proceedings of the SPIE*, 5972:30–37, 2005.

[44] N. Malagnino, G. Pesce, A Sasso, and E. Arimondo. Measurement of trapping efficiency and stiffness in optical tweezers. *Optics Communications*, 214:15–24, 2002.

[45] V. Garcés-Chávez, K. Volke-Sepulveda, S. Chávez-Cerda, W. Sibbett, and K. Dholakia. Transfer of orbital angular momentum to an optically trapped low-index particle. *Physical Review A*, page 063402, 2002.

[46] P. Prentice, M. P. MacDonald, T.G. Frank, P. Campbell, A. Cushieri, G.C. Spalding, W. Sibbett, and K. Dholakia. Manipulation and filtration of low index particles with holographic laguerre-gaussian optical trap arrays. *Optics Express*, 12:593, 2004.

[47] H. Melville, G.F. Milne, G.C. Spalding, W. Sibbett, K. Dholakia, and D. McGloin. Optical trapping of three-dimensional structures using dynamic holograms. *Optics Express*, 11:3562, 2003.

[48] G. Roosen and C. Imbert. Optical levitation by means of two horizontal laser beams: A theoretical and experimental study. *Physics Letters*, 59A:6, 1976.

[49] G. Roosen. A theoretical lens experimental study of the stable equilibrium positions of spheres levitated by two horizontal laser beams. *Optics Communications*, 21:189, 1977.

[50] R. Gussgard, T. Lindmo, and I Brevik. Calculation of hte trapping force in s strongly focussed laser beam. *Journal of Optics Society of America B*, 9:1922, 1992.

[51] S. Nemoto and H. Togo. Axial force acting on a dielectric sphere in a focussed laser beam. *Applied Optics*, 37:6386, 1998.

[52] D. McGloin, V. Garcés-Chávez, and K. Dholakia. Interfering bessel beams for optical manipulation. *Optics Letters*, 28(8):657–659, 2003.

[53] V. Garcés-Chávez, D. McGloin, H. Melville, W. Sibbett, and K. Dholakia. Simultaneous micromanipulation in multiple planes using a self-reconstructing light beam. *Nature*, 419:145–147, 2002.

[54] D. McGloin, A.E. Carruthers, K. Dholakia, and E.M. Wright. Optically bound microscopic particles in one dimension. *Physics Review E*, 69:021403, 2004.

[55] K. Dholakia and D. McGloin. Bessel beams: diffraction in a new light. *Contemporary Physics*, 46:15–28, 2005.

[56] J. Durnin. Exact solutions for nondiffracting beams. i. the scalar theory. *Journal of the Optical Society of America A*, 4:651, 1987.

[57] J.H. McLeod. Axicons and their uses. *Journal of Optical Society of America A*, 50:166, 1960.

[58] A. Ashkin and J.M. Dziedzic. Optical levitation by radiation pressure. *Applied Physics Letters*, 19:283, 1971.

[59] L. Malmqvist and H. M. Hertz. Second-harmonic generation in optically trapped nonlinear particles with pulsed lasers. *Applied Optics*, 34:3392, June 1995.

[60] T.N. Buican, M.J. Smyth, H.A. Crissman, G.C Salzman, C.C. Stewart, and Martin J.C. Automated single-cell manipulation and soring by light trapping. *Applied Optics*, 26:5311–5316, 1987.

[61] D. Altman, H.L Sweeney, and J. Spudich. The mechanism of myosin VI translocation and its load-inducing anchoring. *Cell*, 116:737–749, 2004.

[62] M.D. Wang, M.J. Schnitzer, H. Yin, J. Landick, R.and Gelles, and S.M. Block. Force and velocity measured for single molecules of RNA polymerase. *Science*, 282(5390):902–907, 1998.

[63] C Bustamante, S. Smith, J Liphardt, and D Smith. Single-molecule studies

ofDNA mechanics. *Current Opinion in Structural Biology*, 10:279, 2000.

[64] C.L. Kuyper and D.T. Chu. Optical trapping: a versatile technique for biomanipulation. *Applied Spectroscopy*, 56:300–312, 2002.

[65] J. Guck, R. Ananthakrishnan, H. Mahmood, T.J. Moon, C.C. Cunningham, and J. Kas. The optical stretcher: a novel laser tool to micromanipulate cells. *Biophysical Journal*, 81:767–784, 2001.

[66] C. L. Asbury, A. N. Fehr, and S. M. Block. Kinesin moves by an asymmetric hand-over-hand mechanism. *Science*, 302(5653):2130–2134, 2003.

[67] X. Zhuang. Molecular Biology: Unraveling DNA condensation with optical tweezers. *Science*, 305(5681):188–190, 2004.

[68] K Svoboda, C.F. Schmidt, B.J. Schnapp, and S.M. Block. Direct observation of kinesin stepping by optical trapping interferometry. *Nature*, 365:721–727, 1993.

[69] M.J. McCauley and M.C. Williams. Mechanisms of DNA binding determined in optical tweezers experiments. *Biopolymers*, 85:154–168, 2006.

[70] K Dholakia and P. Reece. Optical micromanipulation takes hold. *Nano Today*, 1:18, 2006.

[71] R.A. Flynn, A.L. Birkbeck, M. Gross, M. Ozkan, B. Shao, M.M. Wang, and S.C. Esner. Parallel transport of biological cells using individually addressable vcsel arrays as optical tweezers. *Sensors and Actuators B*, 87:239–243, 2002.

[72] E Eriksson, J. Enger, B. Norlaner, K Erjavec, Ramser, M. Goksor, S. Hohmann, T Nystrom, and D. Hanstorp. A microfluidic system in combination with optical tweezers for analyzing rapid and reversible alterations in single cells upon environmental changes. *Lab on a chip*, 7:71–76, 2007.

[73] C.E. Sims and N.L Allbritton. Analysis of single mammalian cells on-chip. *Lab on a Chip*, 7:423–440, 2007.

[74] J. Arlt, V. Garcés-Chávez, W. Sibbett, and K. Dholakia. Optical micromanipulation using a bessel light beam. *Optics Communications*, 197:239–245, 2001.

[75] A. D. Bykov, V. E. Zuev, V. P. Lopasov, I. S. Makushkin, L. N. Sinitsa, and O. N. Ulenikov. An analysis of the absorption spectrum of heavy water vapor in the region of 1.06 microns. *Zhurnal Prikladnoi Spektroskopii*, 37:804–810, November 1982.

[76] D.E. Spence, P.N. Kean, and W. Sibbett. 60-fsec pulse generation from a self-mode-locked ti:sapphire laser. *Optics Letters*, 16:42, 1991.

[77] S.A. Tatarkova, W. Sibbett, and K. Dholakia. Brownian particle in an optical potential of the washboard type. *Physical Review Letters*, 91:038101, 2003.

[78] P. Fischer, C.T.A. Brown, J. E. Morris, C. López-Mariscal, E.M. Wright, W. Sibbett, and K. Dholakia. White light propagation invariant beams. *Optics Express*, 13:6657–6666, 2005.

[79] B. Agate, C.T.A. Brown, W. Sibbett, and K. Dholakia. Femtosecond optical tweezers for in-situ control of two-photon fluorescence. *Optics Express*, 12:3011–3017, 2004.

[80] http://www.bioron.net/fluorescein-dutp.243.0.html.

[81] P. Fischer, H. Little, R. Smith, C. Lopez-Mariscal, C.T.A. Brown, E.M. Wright, W. Sibbett, and K. Dholakia. Wavelength dependent propagation and reconstruction of white light bessel beams. *Journal of Optical Society of America A*, 8:477–482, 2006.

[82] P. Fischer, C.T.A. Brown, J. E. Morris, C. López-Mariscal, E.M. Wright, W. Sibbett, and K. Dholakia. White light propagation invariant beams. *Optics Express*, 13:6657–6666, 2005.

[83] O. Jarlman, R. Berg, S. Andersson-Engels, S. Svanberg, and H. Pettersson. Time-resolved white light transillumination for medical imaging. *Acta*

Radiologica, 38:185–189, 1997.

[84] http://www.rp-photonics.com/supercontinuum_generation.html.

[85] S.G. Leon-Saval, T.A. Birks, W.J. Wadsorth, P. St.J. Russel, and M.W. Mason. Supercontinuum generation in sbmicron fibre waveguides. *Optics Express*, 12:2864–2869, 2004.

[86] J.W. Nicholson, A.K. Abeeluck, C. Headley, M.F. Yan, and C.G. Jorgensen. Pulsed and continuous-wave supercontinuum generation in highly non-linear, dispersion-shifted fibers. *Applied Physics B*, 77:211–218, 2003.

[87] M. Prahbu, A. Taniguchi, S Hirose, L. Jianren, M. Musha, A. SHirakawa, and K. Ueda. Supercontinuum generation using raman fiber laser. *Applied Physics B*, 77:205, 2003.

[88] P. Fischer, A.E. Carruthers, K. Volke-Sepulveda, E.M. Wright, C.T.A. Brown, W. Sibbett, and K. Dholakia. Enhanced optical guiding of colloidal particles using a supercontinuum light source. *Optics Express*, 14:5792, 2006.